NORTHWESTERN UNIVERSITY

Analytical Solutions and Optimization of the Time-Dependent Ginzburg-Landau Equation for Superconductors

A DISSERTATION

SUBMITTED TO THE GRADUATE SCHOOL
IN PARTIAL FULFILLMENT OF THE REQUIREMENTS

for the degree

DOCTOR OF PHILOSOPHY

Field of Engineering Sciences and Applied Mathematics

By

Gregory Kimmel

EVANSTON, ILLINOIS

December 2016

ABSTRACT

Analytical Solutions and Optimization of the Time-Dependent Ginzburg-Landau Equation for Superconductors

Gregory Kimmel

The behavior of type-II superconductors is modeled using the time-dependent Ginzburg Landau equations (TDGLE). Pinning centers (inclusions) and geometries which maximize the critical current that can be passed through a superconductor are numerically obtained. Previous analytical results are summarized and new results are obtained for the critical current in one and two-dimensional systems with and without an inclusion. Tangentially, analytical results of the iterative method – Weighted Jacobi are derived.

Acknowledgments

First and foremost, I would like to thank my two advisors: Igor Aronson and Andreas Glatz. Working alongside them over the past four years has truly been inspirational. Igor's innate ability to look at a complicated problem and guess a (usually correct) solution has been extremely humbling and has shown me how much intuition is required to be a great scientist. Andreas's immeasurable time spent looking over code and giving advice on which phenomenon to investigate and analyze was helpful insightful. Additionally, their patience and compassion during my tenure at Argonne was invaluable especially and most importantly at those moments when I lost those qualities in myself.

I would also like to thank Ivan Sadovvsky who helped build the routine used in obtaining the optimization numerical results. Also, for being available by Skype for the (sometimes dumb) questions at midnight on computational and compiling issues that I went through.

Additional thanks to my committee members: Vladimir Volpert and Hermann Riecke for helping me with my often tangential asymptotic questions and Alvin Bayliss with the numerical analysis of iterative methods. They, along with the other faculty of ESAM, helped further our knowledge of mathematics and it was a privilege to be trained by such amazing professors.

And of course, I would like to thank my family and friends for their love and support over these last few years. Dr. Monette Sachs for believing in me even when I scored in the 30th percentile in school. My uncle Stuart for helping me through an especially difficult

year. But most of all I would like to thank my mother, for keeping me company on the rides to and from Argonne over the years, for listening and trying to understand the math I was working on that day, even though it was difficult, and for teaching me to never give up even when I found out that weeks of work had been wasted over a silly mistake.

Finally, I would like to dedicate this thesis to my father, who unfortunately passed away a year ago from lung cancer before I finished my Ph.D. During the year he was sick, I spent my time at home to help take care of him, and if it wasn't for his love and support, would likely have not had the strength to finish this program.

Table of Contents

List of Tables

List of Figures

CHAPTER 1

Introduction

Before I give a brief history of superconductivity, I would like to briefly describe the purpose of this study. Understanding high-temperature superconductors have broad applications, from medicine, transportation to more accurate measurements of physical phenomena. Of particular interest is loss-less energy, the threshold (critical) current with which we can push a superconductor before it loses this amazing property.

In this thesis, the main tool is the Time-Dependent Ginzburg-Landau equation (TDGL), an equation derived in the early 1950s, valid for superconductors near its critical temperature. I used the TDGL to understand the mechanisms of energy loss and for the optimization of the critical current. The following is a quick outline of what each section was devoted to:

1. Introduction: A brief history of superconductivity as well as derivations of important physical properties following Schmidt and Tinkham – filling in details that I found useful or omitted.
2. Mechanism of dissipation in Weak-Link 1D superconductors are analyzed (phase slips, loosely 1D magnetic vortices). I extract a simplified model of coupled ODEs using the TDGL which explains the appearance of phase slips and I show the agreement with numerical simulations.
3. Loss of superconductivity of 2D superconductors in the presence of an external magnetic field and current are studied. A critical curve defining the threshold between superconducting and normal is computed.

4. Optimization of the critical current for varying geometries in 2D and 3D superconductors are numerically studied (e.g. square lattice of circular inclusions (2D), spherical vs. columnar inclusions in a 3D superconductor).
5. Analysis of the numerical method – weighted Jacobi to solve the TDGL equation. Analytical results for the optimal weighting parameter are derived under general conditions.

1.1. A brief history of superconductivity

In 1911, Heike Kamerlingh Onnes noticed a peculiar phenomenon when pure metals are brought to very low temperatures. In particular, at 4.2 K the resistance of a solid mercury wire suddenly vanished [**1**]. Onnes called this phenomenon "superconductivity" as it allowed a current to pass through the wire indefinitely. He was awarded the Nobel Prize in Physics in 1913 for his work on low temperature physics.

The next important step in understanding this new phenomenon occurred in 1933 when Meissner and Ochsenfeld discovered that magnetic distributions of magnetic fields in pure tin and lead samples were expelled when the metal was in the superconducting state [**2**]. It only took a few more years for the London brothers to show that the Meissner effect was simply a consequence of the minimization of the free energy of the system [**3**]. The London theory showed that in fact a certain amount of magnetic flux penetrates the superconductor to a certain depth. This depth, the London (magnetic) penetration depth is denoted by λ.

Experimentally, the behavior of a superconductor in an external magnetic field can be split into type-I and type-II superconductors. They are partitioned by how a superconductor leaves the Meissner state. Above a critical magnetic field, often denoted H_{c_1}, type-I goes to a normal metal, while type-II superconductors reaches the so-called "mixed state," where quantized magnetic flux – magnetic vortices penetrate through the superconductor, see figure

1.1. The London theory was not able to explain the physics of a type-II superconductor. An explanation would have to wait another 15 years.

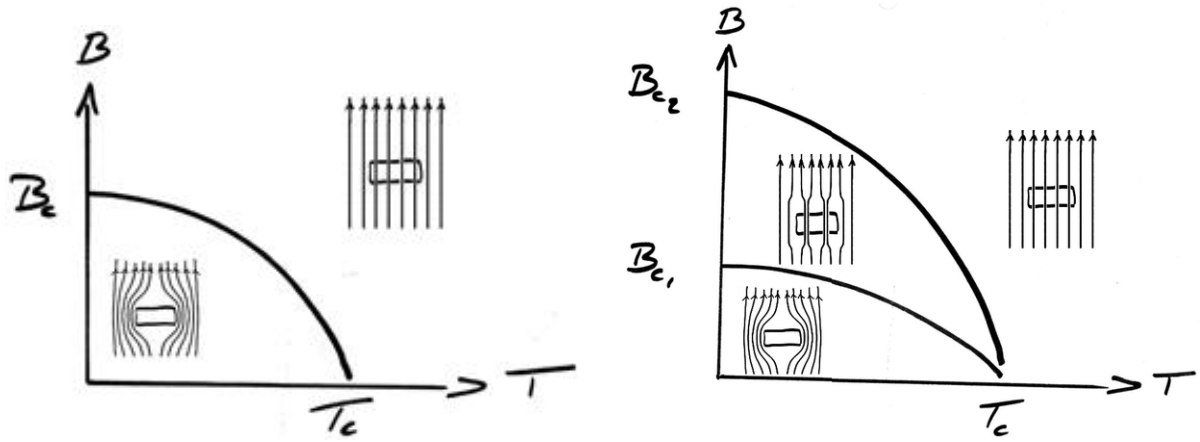

Figure 1.1. Phase diagram comparing type I and type II superconductivity.

The mystery of the existence and separation of these two types were found phenomenologically through brilliant intuition and probably divine inspiration. In the 1950s, Lev Landau and Vitaly Ginzburg combined Landau's theory of second-order phase transitions along with the assumption that the behavior can be modeled by a single complex order parameter Ψ describing the macroscopic superconducting state to create the now famous Ginzburg-Landau (GL) theory. The GL theory extended the previous work of the London brothers and showed that an additional term in the free energy through quantum effects was what accounted for the transition between the two types [**4**, **5**]. The GL theory also predicted two length scales, the magnetic penetration depth (analogous to the London theory) and the coherence length ξ which measures the length needed for variation in Ψ. This is particularly useful when analyzing the behavior of vortices – topologically singularities in the order parameter which recover on the order of ξ.

In two landmark papers, Alexei Abrikosov, a student of Landau used the GL theory to show the location of this transition between type-I and type-II in terms of the dimensionless GL parameter $\kappa = \lambda/\xi$. Additionally, he showed that magnetic flux lines (or vortices) align in such a way to minimize the free energy and that this leads to a square lattice [**6**–**8**]. The observant reader (and one familiar with superconductivity), may notice that I said square lattice. In his original paper in 1957, Abrikosov made a small mistake in minimizing the free energy and found a value slightly larger than optimal, this slight change – an error on the order of 2% was the difference between the correct triangular lattice and the incorrect square lattice. This was found and corrected seven years later [**9**]. Originally, Abrikosov's work went largely unnoticed. In fact, Landau was originally skeptical that the vortex lattice derivation was even correct. However, a few years later, multiple experiments [**10**,**11**] verified the existence of the "Abrikosov lattice" as it soon became known.

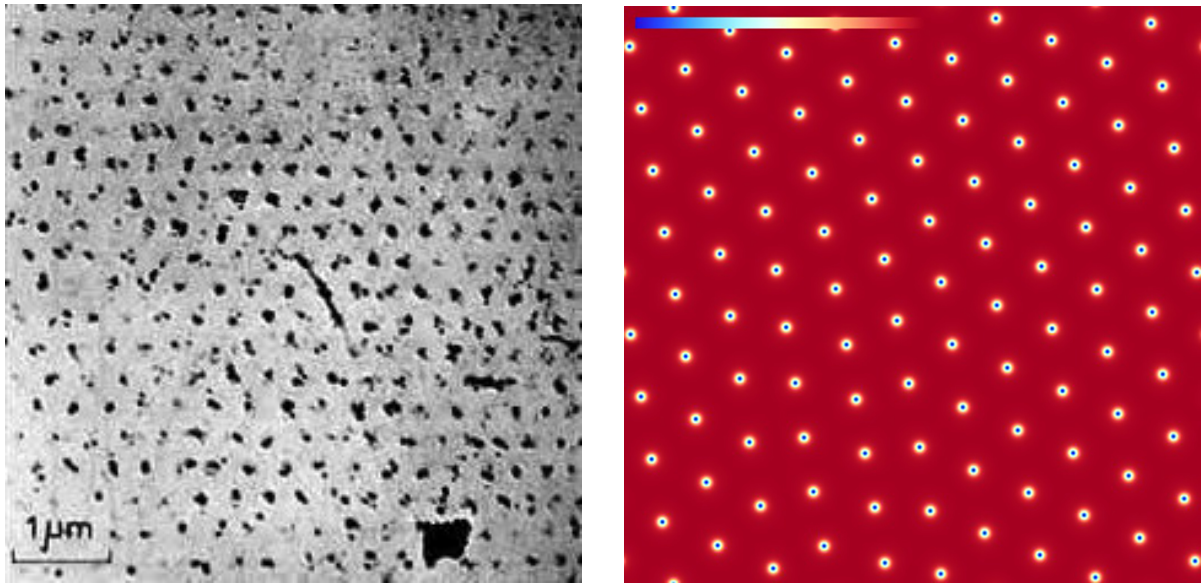

Figure 1.2. Abrikosov lattice of flux lines on the surface of a superconductor (left) and numerical solution of TDGLE (right).

All these advancements in the understanding of superconductivity culminated in 1957, when a complete microscopic theory of superconductivity was proposed by Bardeen, Cooper and Schrieffer (BCS). This BCS theory explained that the superconducting current behaved as a superfluid comprised of pairs of electrons known as "Cooper pairs." Unlike electrons, these pairs now have integer spin, so they are Bosons, therefore they do not suffer the restriction of the Pauli exclusion principle. This allows them to simultaneously occupy the same state. Soon after, Bogolyubov rigorously obtained the BCS wave function via a canonical transformation of the Hamiltonian, and Gor'kov showed that the BCS theory reduced to the GL theory close to the critical temperature [**12**–**14**]. The result of Gor'kov is not terribly surprising, though still a relief as it put the phenomenological GL theory on more rigorous terms.

1.2. Weak-Link Superconductors: Josephson Junctions and Dayem Bridges

Practical applications for superconductors involve high-temperature type-II superconductors where the critical temperature is more commercially feasible [**15**, **16**]. In 1962, Josephson predicted an entirely new effect based on quantum tunneling [**17**] of electrons. Prior to Josephson's work, it was only known that normal electrons could move through an insulating barrier through tunneling. Josephson was the first to predict that this would also be true of Cooper pairs moving across these barriers, now known as Josephson junctions (JJs). Experiments verifying this result appeared almost immediately [**18**–**20**] and in 1973, Josephson was awarded the Nobel prize in physics for his work.

Many variants and extensions of the original JJ have since been discovered and analyzed [**21**,**22**]. A Dayem bridge is a thin-film variant of the JJ in which the weak link is on the order

of a few micrometers or less [**23**]. There have been important applications of JJs in quantum-mechanical circuits, such as superconducting quantum interference devices (SQUIDs) and superconducting qubits [**24**–**26**]. SQUIDs allow for extremely accurate measurements of very small magnetic fields. SQUIDs are composed of a two superconducting wires insulated by a thin normal metal (JJ) with an applied biasing current. The magnetic field passing through the center of the SQUID can be measured by noting the periodic change in voltage. Since magnetic flux in a superconductor is quantized, the periodic voltage jumps correspond to quantized changes in the flux. This allows someone to measure fields on the order of the flux quantum ($10^{-14}T$!).

The remaining sections in the introduction are a review of the theory of superconductivity taken mostly from Schmidt [**4**] and Tinkham [**27**] with some details filled in where necessary. The review is mostly chronological, however properties of Type-I superconductors are considered first. The London approximation is discussed next, followed by the GL theory. These two are the most detailed as these approximations were used most in the calculations and analysis in this thesis. I briefly discuss BCS theory and the derivation of the Abrikosov lattice.

Finally, since we make use of Maxwell's equations and the Lorentz force frequently, I will write them in the form we used here:

(1.1a) $$\nabla \cdot \boldsymbol{E} = 4\pi\rho \qquad\qquad \nabla \cdot \boldsymbol{B} = 0$$

(1.1b) $$\nabla \times \boldsymbol{B} = \frac{1}{c}\left(4\pi\boldsymbol{j} + \frac{\partial \boldsymbol{E}}{\partial t}\right) \qquad\qquad \nabla \times \boldsymbol{E} = -\frac{1}{c}\frac{\partial \boldsymbol{B}}{\partial t}$$

(1.1c) $$\boldsymbol{F} = q(\boldsymbol{E} + \boldsymbol{v} \times \boldsymbol{B}).$$

Note also that we may write this in terms of vector and scalar potentials $\boldsymbol{E} = -\nabla V - \frac{\partial \boldsymbol{A}}{\partial t}$ and $\boldsymbol{B} = \nabla \times A$, where V and $\boldsymbol{A}$ are the electric and magnetic vector potential, respectively.

1.3. Magnetic properties of superconductors

Let us first consider the magnetization of a long cylinder type-I superconductor in an external field $\boldsymbol{H}_0$ parallel to its axis. We know that for $\boldsymbol{H}_0 < \boldsymbol{H}_{c_1}$, the magnetic field does not penetrate the superconductor and so $\boldsymbol{B} = 0$. The magnetization relates these two quantities and is given by the expression

$$\boldsymbol{B} = \boldsymbol{H}_0 + 4\pi \boldsymbol{M}. \tag{1.2}$$

We now show some basic properties of type-I superconductors which are consequences of Maxwell's equations and the fact that for $\boldsymbol{H}_0 < \boldsymbol{H}_{c_1}$, we have $\boldsymbol{B} = 0$ and $\rho = 0$.

(1) *Magnetic field lines outside a superconductor are always tangential to its surface.*

Proof. From Maxwell's equations, we know that $\nabla \cdot \boldsymbol{B} = 0$. Then let Ω_ϵ be a surface extending into the superconductor of length l and width ϵ, we have by Green's theorem

$$0 = \int_{\Omega_\epsilon} \nabla \cdot \boldsymbol{B}\, dV = \int_{\partial\Omega_\epsilon} \boldsymbol{B} \cdot \hat{\mathbf{n}}\, dS.$$

Now, letting $\epsilon \to 0$ we see that this implies that $B_n^{(i)} = B_n^{(e)}$ (the other contributions will vanish). Finally, we note that $\boldsymbol{B} = 0$ inside the superconductor and so $B_n^{(e)} = 0$, which proves the claim. □

(2) *A superconductor in an external magnetic field always carries an electric current near its surface.*

Proof. Let $\boldsymbol{H}_0$ be the external magnetic field near the surface of a superconductor. Then by Maxwell (1.1b), we see that $\nabla \times \boldsymbol{B} = \frac{4\pi}{c}\boldsymbol{j}$. Far inside the superconductor (such that any line integral does not contain the boundary), we would see $\boldsymbol{B} = 0$, and so $\boldsymbol{j} = 0$. So only an electric current at the surface is possible. To show that this depends on the field, we consider a closed contour (see figure 1.3 taken from Schmidt [**4**]).

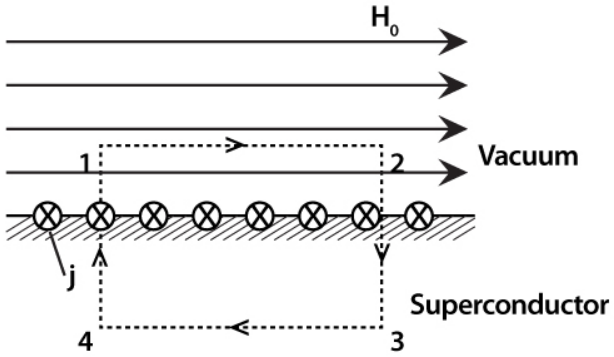

Figure 1.3. Contour 1-2-3-4 goes through superconductor. The line 3-4 is far enough in the superconductor so that $\boldsymbol{B} = 0$.

Then we calculate (1.1b) along the contour and obtain

$$\frac{4\pi}{c}J = \int (\nabla \times \boldsymbol{B}) \cdot d\mathbf{A} = \oint \boldsymbol{B} \cdot d\boldsymbol{l} = H_0 l_{12},$$

where $J = j_{\text{surf}} l_{12}$. □

This is a screening current which keeps the interior of the superconductor screened from the influence of the external field. It can be written in the following form

$$\boldsymbol{j}_{\text{surf}} = \frac{c}{4\pi}(\boldsymbol{n} \times \boldsymbol{H}_0).$$

1.4. Thermodynamics of superconductors

Consider again a long type-I cylindrical superconductor with uniform field $\boldsymbol{H}_0$ applied parallel. Below the critical field $H_{\rm cm}$, the induction is zero (Meisner). Hence $\boldsymbol{M} = -\boldsymbol{H}_0/4\pi$. What then is the work an external magnetic field does on a superconductor? Suppose we increase the magnetic field by an amount $d\boldsymbol{H}_0$, then the amount of work stored is

$$-\int_0^{H_0} \boldsymbol{M}\, d\boldsymbol{H}_0 = \int_0^{H_0} \frac{\boldsymbol{H}_0}{4\pi}\, d\boldsymbol{H}_0 = \frac{H_0^2}{8\pi},$$

this is similar to the magnetic energy stored in a field ($|\boldsymbol{B}|^2/2\mu_0$).

Define the free energy density of the superconductor in zero magnetic field as F_{s0}, then the superconductor in a finite field has energy

$$F_{sH} = F_{s0} + \frac{H_0^2}{8\pi}. \tag{1.3}$$

The transition to the normal state occurs when the free energy of the superconductor is higher than the free energy of the normal metal F_n. This occurs at $H_0 = H_{\rm cm}$ and corresponds to

$$\Delta F := F_n - F_{s0} = \frac{H_{\rm cm}^2}{8\pi}. \tag{1.4}$$

We see then that the critical field is a measure of the difference in free energy between the two states.

1.5. Entropy of a superconductor

We begin with the Helmholtz free energy

$$F = U - TS, \tag{1.5}$$

where U is the internal energy, T is temperature and S the entropy. Then the infinitesimal change is

$$\delta F = \delta U - T\delta S - S\delta T.$$

Since we have a reversible process (phase transitions are reversible), then $\delta Q = T\delta S$ and by the first law of thermodynamics

$$\delta U = T\delta S - \delta W. \tag{1.6}$$

Inserting (1.6) into the previous equation gives

$$\delta F = -\delta W - S\delta T.$$

Holding W constant it follows that

$$S = -\left(\frac{\partial F}{\partial T}\right)_W. \tag{1.7}$$

If we differentiate (1.4) with respect to T (using (1.7)), we obtain

$$S_{s0} - S_n = \frac{H_{cm}}{4\pi}\left(\frac{\partial H_{cm}}{\partial T}\right)_W. \tag{1.8}$$

This simple equation along with the experimental results summarized in figure 1.1 lead to some very important conclusions.

(1) *The superconducting state is more ordered than the normal one.* Indeed, this follows simply by the experimental fact that as T increases the critical field decreases monotonically and so $(\partial H_{cm}/\partial T)_W < 0$ from which it follows that $S_{s0} < S_n$.

(2) *The transition from normal to superconducting at $T = T_c$ is a second-order phase transition.* At $T = T_c$, we know that $H_{cm} = 0$ from which it follows that $S_{s0} = S_n$. Since there is no change in entropy, there is no latent heat and so the transition at $T = T_c$ is a second-order phase transition. This fact was extremely important in the formulation of the GL theory, which is based on Landau's previously established theory on second-order phase transitions.

(3) *At $T < T_c$, transitions between states are all first-order phase transitions.* Similar to (2), this follows by noting that when $T < T_c$ we have $S_{s0} < S_n$ and so any change leads to a change in entropy which must be accompanied by an exchange of latent heat.

As a final note, it is useful to use the Gibbs free energy instead of Helmholtz, since typically the external magnetic field is constant. Therefore, we will use

$$G = F - \frac{\boldsymbol{B} \cdot \boldsymbol{H}_0}{4\pi} = U - TS - \frac{\boldsymbol{B} \cdot \boldsymbol{H}_0}{4\pi}. \tag{1.9}$$

1.6. London Theory

The London theory, was the first successful attempt at understanding the behavior of superconductors. Its major assumptions are that there are superconducting electrons of density n_s and normal electrons of density n_n of which the total density is then given by $n = n_s + n_n$. As T increases from 0 to T_c, n_s goes from n to 0. The big simplification compared to the GL theory (which would not appear for nearly two more decades) is that there was no significant change in n_s in space, that is $n_s(\boldsymbol{r}) \approx n_s$. Finally, it is assumed that $\boldsymbol{B}, \boldsymbol{E}$ are small enough so that its influence on n_s is negligible.

1.6.1. London equations

Inside the superconductor $B \approx 0$ and so the equation of motion for superconducting electrons should follow

$$n_s m \frac{d\boldsymbol{v}_s}{dt} = n_s e \boldsymbol{E}, \tag{1.10}$$

where m, e are the electron mass and charge, respectively and $\boldsymbol{v}_s$ is the superconducting electron velocity. The definition of current density is given by $\boldsymbol{j}_s = n_s e \boldsymbol{v}_s$. Plugging this into (1.10), we have

$$\boldsymbol{E} = \frac{d}{dt}\left(\frac{m\boldsymbol{j}_s}{n_s e^2}\right).$$

Defining $\Lambda = \frac{m}{n_s e^2}$, we have the first London equation:

$$\boldsymbol{E} = \frac{d(\Lambda \boldsymbol{j}_s)}{dt}. \tag{1.11}$$

The second London equation involves the variation of the magnetic field for details see appendix A.1. Noting (A.2) and using (A.4) we obtain the second London equation

$$\boldsymbol{H} + \lambda^2 \nabla \times (\nabla \times \boldsymbol{H}) = 0. \tag{1.12}$$

The definition of the penetration depth λ is now obvious, it is the length scale of variation of the magnetic field $\boldsymbol{H}$ inside the superconductor. If we use the London gauge,

$$\nabla \cdot \boldsymbol{A} = 0, \tag{1.13a}$$

$$\boldsymbol{A} \cdot \boldsymbol{n} = 0, \tag{1.13b}$$

then (1.12) can be written as

$$\boldsymbol{j}_s = -\frac{1}{c\Lambda}\boldsymbol{A} = -\frac{c}{4\pi\lambda^2}\boldsymbol{A}. \tag{1.14}$$

1.6.2. Generalized London equation and magnetic flux

Here we take a brief detour to explain the appearance of quantized magnetic flux by looking at the Lorentz force law (1.1c), for details see appendix A.2. From (A.5), we see that the canonical momentum is

$$\boldsymbol{p} = \frac{\partial \mathcal{L}}{\partial v} = m\boldsymbol{v} + \frac{q}{c}\boldsymbol{A}.$$

The current density is given by

$$\boldsymbol{j}_s = \frac{\hbar e}{m}\Im(\Psi^*\nabla\Psi).$$

Using the definition for current density, we obtain $2m\boldsymbol{v}_s = \hbar\nabla\theta$. Thus the total momentum is given by

$$\hbar\nabla\theta = 2m\boldsymbol{v}_s + \frac{2e}{c}\boldsymbol{A}, \tag{1.15}$$

where $m \to 2m$ and $q = 2e$. Originally, it was thought that single electrons carry a superconductor and early experiments showed that the quantized magnetic flux was actually off by a factor of 2. This provided strong evidence that the carrier of superconductors were in fact pairs of electrons – Cooper pairs.

Using the definition for supercurrent density once again, we obtain the generalized London equation:

$$\boldsymbol{j}_s = \frac{1}{c\Lambda}\left(\frac{\Phi_0}{2\pi}\nabla\theta - \boldsymbol{A}\right), \tag{1.16}$$

where $\Phi_0 = \frac{hc}{2e}$ and has dimensions of magnetic flux. Consider now a superconductor which is topologically similar to a torus (i.e. has a single hole). At $T > T_c$, magnetic fields penetrate the superconductor and hole. As T decreases below T_c, the field is expelled from the bulk of the superconductor, however there is magnetic flux that remains inside the hole. To find out what this flux is, we take the line integral C around this hole where the minimum distance between the path and the hole is much greater than λ and hence $\boldsymbol{j}_s = 0$ there. Using (1.16), we obtain

$$\frac{\Phi_0}{2\pi} \oint_C \nabla\theta \cdot d\boldsymbol{l} = \oint_C \boldsymbol{A} \cdot d\boldsymbol{l} = \Phi,$$

where Φ is the total magnetic flux through the contour C. To ensure that the wave function is single-valued, we require that after a going around the contour C the flux must be an integral multiple of $2\pi n$, this leads to

$$\Phi = n\Phi_0. \tag{1.17}$$

1.7. Ginzburg-Landau Theory

London theory did an excellent job of explaining type-I superconductors and the Meissner effect, however it was not able to explain the appearance of the mixed state in type-II superconductors. Evidently the interface energy between normal and superconducting becomes favorable and this effect is not captured with the London theory. About two decades later, Ginzburg and Landau (GL) used Landau's theory of second-order phase transitions to describe the superconductor in the vicinity of the critical temperature. The first assumption – the critical temperature is a second order phase transition, was based on experimental observations and thermodynamic principles (see section 1.5). The second assumption was that this system could be modeled by a single complex order parameter Ψ. These two assumptions

lead to an expansion of the free energy near the critical temperature. An Euler-Lagrange equation then ultimately leads to the famous GL equations.

1.7.1. The free energy and the GL equation

The minimization of this free energy F is a variational problem in $\Psi, \mathbf{A}$. In the spatially homogenous case, F should be rotationally invariant, thus we expect only powers of $|\Psi|$ to appear. Finally, we note that analyticity of F forces only even powers. A similar argument holds for the gauge invariant derivative term and we obtain,

$$F[\Psi, \mathbf{A}] = F_n + \alpha|\Psi|^2 + \frac{\beta}{2}|\Psi|^4 + \frac{1}{2m}|(-i\hbar\nabla - 2e\mathbf{A})\Psi|^2 + \frac{|\mathbf{B}|^2}{2\mu_0}.$$

Define the coherence length $\xi = \sqrt{\frac{\hbar^2}{4m|\alpha|}}$, the magnetic penetration depth $\lambda = \sqrt{\frac{mc^2\beta}{8\pi e^2|\alpha|}}$ and $\kappa = \lambda/\xi$, then take a variational derivative with respect to Ψ^* and $\mathbf{A}$ which gives

$$\begin{aligned} 0 &= \left(\nabla - i\frac{2\pi}{\Phi_0}\mathbf{A}\right)^2 \Psi + (1 - |\Psi|^2)\Psi \\ 0 &= \kappa^2 \nabla \times (\nabla \times \mathbf{A}) - |\Psi|^2 \left(\frac{\Phi_0}{2\pi}\nabla\theta - \mathbf{A}\right), \end{aligned}$$

where $\Psi = |\Psi|e^{i\theta}$. In the infinite κ limit, (e.g. strong type-II), we see that $\nabla \times \mathbf{B} = 0$ and the relation for $\mathbf{A}$ is just given by the quantity in parenthesis.

These equations were successfully used to predict the existence of the mixed state as a hexagonal (Abrikosov) lattice. However to investigate the dynamic behavior we would like to see how the superconductor relaxes to this steady state. To investigate this the TDGL equation is introduced now.

1.7.2. Time-Dependent Ginzburg-Landau equation

The TDGL equation is given below for the infinite κ limit [**56**]:

$$\Gamma\left(\partial_t + i\frac{2e}{\hbar}\mu\right)\Psi = \frac{\hbar^2}{4m}(\nabla - i\mathbf{A})^2\Psi + a_0\nu(\mathbf{r})\Psi - b|\Psi|^2 + \Psi, \tag{1.18}$$

$$\mathbf{j}_0 = |\Psi|^2\left(\frac{\Phi_0}{2\pi}\nabla\theta - \mathbf{A}\right) - \sigma_n(\nabla\mu + \partial_t\mathbf{A}), \tag{1.19}$$

where Γ, a_0, b are phenomenological parameters that can be found from the microscopic theory [**57**], e, m are the electron charge and mass, μ is the scalar potential, and $\nu(x)$ a spatially dependent linear coefficient modeling inhomogeneities in the system and σ_n is the conductivity in the normal state. Following Sadovskyy et al. [**58**], we define the $+x$ direction to be the direction of the external current and obtain the following dimensionless form:

$$u(\partial_t + i\mu)\Psi = (\nabla - i\mathbf{A})^2\Psi + [\nu(\mathbf{r}) - |\Psi|^2]\Psi \tag{1.20a}$$

$$\mathbf{j} = \Im\{\Psi^*(\nabla - i\mathbf{A})\Psi\} - (\nabla\mu + \partial_t\mathbf{A}) \tag{1.20b}$$

$$\nabla\cdot\mathbf{j} = \nabla\cdot\mathbf{A} = 0. \tag{1.20c}$$

Here Ψ is the complex order parameter, satisfying $|\Psi| = 1$ in the purely superconducting state, and $|\Psi| = 0$ in the normal state. The parameter $u = \Gamma/a_0\tau_{\mathrm{GL}}$ is a material-dependent parameter, with time $\tau_{\mathrm{GL}} = 4\pi\sigma\lambda_0^2/c^2$, $\lambda_0 = \sqrt{\frac{mc^2}{8\pi e^2\psi_0^2}}$ is the magnetic penetration depth (c the speed of light) and $\psi_0 = \sqrt{a_0/b}$ is the equilibrium value of the order parameter when spatial variations are neglected, i.e., $\nu(x) = 1$. The zero temperature coherence length $\xi_0 = \sqrt{\frac{\hbar^2}{4ma_0}}$ is used for the unit of length. The magnetic vector potential and field is $\mathbf{A}$ and $\mathbf{B}$, respectively. The momentum operator is the classical gauge invariant operator for a charged particle in a magnetic field $\nabla \to \nabla - iA$. For more details see [**58**].

Later developments involving a linearized Eilenberger equation in the dirty limit has been studied as a generalized TDGL equation. It involves an additional parameter γ related to the interactions of inelastic electron-phonon collisions and was first derived in [**54**]. The equation is enlightening in its own right so I define it here

$$\frac{u}{\sqrt{1+\gamma^2|\Psi|^2}}\left(\partial_t + i\mu + \frac{\gamma^2}{2}\frac{\partial|\Psi|^2}{\partial t}\right)\Psi = (\nabla - i\mathbf{A})^2\Psi + (1-|\Psi|^2)\Psi \tag{1.21a}$$

$$\mathbf{j} = \Im\{\Psi^*(\nabla - i\mathbf{A})\Psi\} - (\nabla\mu + \partial_t\mathbf{A}) \tag{1.21b}$$

$$\nabla\cdot\mathbf{j} = \nabla\cdot\mathbf{A} = 0. \tag{1.21c}$$

It is clear that (1.21a) with $\gamma = 0$ reduces to (1.20).

1.8. Dissipative States in Type-II Superconductors

The main goal of this thesis is to gain insight into the mechanisms of dissipation in Type-II superconductors. In 1D, phase slips drive dissipation through voltage jumps which proceeds phase slips. For higher dimensional superconductors, the main cause is the motion of magnetic vortices, driven by the Lorentz force. The primary tool used in this thesis is the TDGL equations which involve the use of a complex order parameter Ψ to model whether a material is superconducting.

1.8.1. Phase Slips in 1D Superconductors

In thin superconducting wires, phase slips are made when the magnitude of the order parameter $|\Psi| \to 0$ and the phase goes through a 2π jump. An example of a phase slip event is given in figure 1.4(a). Chapter 2 is devoted to investigating phase slips in weak-linked superconducting wires. In this case the suppression of Ψ inside the weak link allows for the

successful asymptotic expansion of Ψ. This allows us to give a complete description of the dynamics of phase slips in weak-link superconductors through a pair of coupled ODEs.

1.8.2. Magnetic Vortices in 2D and 3D Superconductors

In 2D and 3D superconductors, motion of magnetic vortices are the main culprit of dissipation of energy. In contrast to phase slips, which can be loosely thought of as static 1D vortices, in 2D and 3D, static vortices do not create dissipation. This is easy to understand as follows, supercurrent can flow around these singularities in 2D and 3D. In 1D, however this is not possible.

In contrast, when the magnetic field and current are applied in parallel, there is no Lorentz force and yet superconductivity is still destroyed above some critical field. This critical curve for a 2D sample is extracted analytically in chapter 3. Previously, I mentioned that vortices move via the Lorentz force, the larger the current the stronger the force. The main idea of enhancing the maximal current is to impede the motion of vortices through pinning centers. In chapter 4, we discuss this in terms of an optimization problem where we look to find the optimal pinning geometry for a given set of geometrical parameters (e.g. radius of inclusion, volume fraction, type of inclusion).

1.8.3. Numerical Solutions of the TDGL

High-performance computing has allowed us to simulate superconducting domains that would have been computationally infeasible before. The TDGL equation is solved on GPUs using world-class supercomputers (e.g. Mira at ANL and Titan at ORNL). The TDGL code used employs the weighted Jacobi method to solve a Crank-Nicholson implicit time scheme for the relaxation step. The parallel nature of Jacobi's method made it a primary candidate for

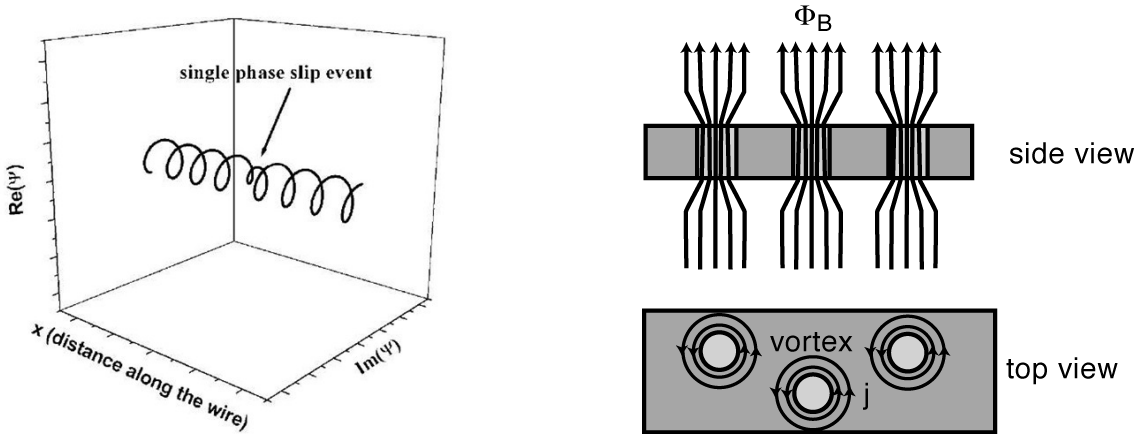

Figure 1.4. Two main types of dissipation in type-II Superconductors: phase slip event (left), magnetic vortices (right).

GPU code. In the final chapter, I investigate some theoretical properties of matrices from Jacobi's method and derive the best-worst case weighting parameter for certain classes of matrices.

CHAPTER 2

Phase slip centers in quasi-1D superconductors

2.1. Introduction

The motion of Abrikosov vortices is recognized as the main cause of dissipation in type-II superconductors [**28**]. Conversely, in thin nanowires, the motion of vortices is impeded and phase-slip events are responsible for the dissipation. Phase slips, changing the phase difference of the superconducting order parameter by 2π, may be caused by different physical mechanisms. Thermally activated phase slips at high temperatures and small applied currents are well understood [**27**]. At very low temperatures, phase slips can be caused by quantum fluctuations (aptly called quantum phase slips) [**29**–**31**]. Phase slips are not unique to superconductors, they also occur in superfluid systems [**32**–**34**], and more recently, dissipation due to phase slips were studied in cold atom systems [**35**–**37**]. In particular, phase slips can be triggered in a superfluid cold atom system by a rotating weak link [**38**].

Even without thermal and quantum fluctuations, the phase slip phenomena and dissipative (or resistive) states can be induced by an applied current [**39**, **40**]. Magnetic field penetrates type-II superconductors in the form of Abrikosov vortices. If an external current is applied, the Lorentz force induces motion of the vortices. This motion is the main cause of dissipation in 2D and 3D superconductors. However, in quasi-one dimensional nanowires with the coherence length $\xi(T)$ and the penetration depth $\lambda(T)$ large compared to the wire diameter, vortex motion is suppressed. In this situation the transition to the normal state was made through successive voltage jumps which are attributed to the appearance of phase

slip centers [**39**,**40**]. A study of this phenomenon was given first by Kramer and Baratoff who found that slightly below the depairing current, there is a dissipative state which consists of localized phase slips occurring in the superconducting filament [**41**]. In a narrow range of currents close to the depairing current, the material is superconducting except in narrow regions where phase slip centers (PSCs) occur. The period of these PSCs diverge as the external current approaches the lower bound in this narrow region. It was also shown that random thermal fluctuations allow for phase slips [**42**], but these did not persist indefinitely. Further numerical study of the one-dimensional time-dependent Ginzburg-Landau equation revealed periodic phase slips existing in a narrow range of currents close to the depairing current [**43**,**44**]. Follow-up numerical studies of narrow two-dimensional superconducting strips discovered a transition from a phase-slip-line to vortex pairs [**45**]. Periodic lattices of the phase slip centers were studied in the context of vortex penetration in thin superconducting films near the third critical magnetic field [**46**]. Using a saddle-point approximation for the Ginzburg-Landau energy in narrow superconducting strips, the dependence of voltage drop vs temperature and bias current (neglecting thermal fluctuations) was studied in [**47**].

The situation is different, however, for spatially inhomogeneous systems, such as superconductors with macroscopic defects or weak links [**48**]. Perhaps the most famous examples are Dayem bridges and Josephson junctions [**17**,**23**]. The mechanism for dissipation in these cases is the quantum tunneling of Cooper pairs between the two superconductors, which is caused by a phase difference between the weakly-linked superconductors. When the current is below some threshold j_c, the phase difference is fixed in time and a stationary superconducting state persists. Above this threshold, the solution exhibits oscillations, which lead to a finite voltage. In a review paper by Ivlev and Kopnin, inhomogeneities were analyzed, but in regards to the stability of the normal state [**49**]. Thus, their analysis involved currents

much closer to the GL critical threshold $j_{GL} = 2/\sqrt{27}$. A lower bound j_1 at which the normal state was globally unstable (i.e. arbitrary small perturbation lead to instability of the normal state), and above which there was a critical-sized perturbation which separated the normal and superconducting states was estimated. Also, an upper critical current j_2 such that the normal state was absolutely stable for an external current $j_0 > j_2$ was found. An inhomogeneity much smaller than the coherence length, $\xi(T)$, was used and was approximated by a δ function, simplifying the algebra. Here we consider a more realistic situation for the type-II high-temperature superconductors: an inclusion on the scale of $\xi(T)$. The transition we are interested in analyzing, occurs between the non-uniform superconducting state and the oscillatory state with phase slips. Therefore, the steady state and linearization in this paper are much more complex then in analyzing the normal state. The authors of [**50**] have shown experimental results of weak-links with non-hysteric behavior.

The phase slip state of homogenous systems have recently been analyzed in much greater detail [**51**]. Using bifurcation analysis, Baranov et. al. extract the normal form of a saddle-node bifurcation when the current is near the critical current. They then correctly determine the characteristic scaling law and show its agreement with numerical simulations. The period diverges in an infinite-period saddle-node bifurcation as $j_0 \to j_c$. These authors further expanded upon their analysis by showing the important role that the material parameter u plays in the type of bifurcation that can occur [**52**] (u is related to the electric field penetration depth). They observed that for finite lengths and values of u above some critical threshold u_{c2}, numerical simulations showed hysteresis in the I-V curve. However, our work focuses on analytical methods for the inhomogeneous system, which as stated previously makes the steady state and linearization much more difficult to handle. We show that a simplified system can be obtained through weakly nonlinear analysis and that this system

contains the normal form obtained in [**51**] as the size of the weak link shrinks to zero. We also demonstrate that in addition to the infinite period bifurcation for small u, a hysteresis exists in our system for large u values, similar to that in [**51**]. However, in contrast to previous studies, our reduced two-dimensional nonlinear system exhibits evolution of periodic orbits and a transition between superconducting and normal states that are not properly captured by the one-dimensional model in [**51**].

A work by Michotte et. al. in [**53**] have found that the condition for PSCs to occur is based on the competition between two relaxation times: the relaxation time for the magnitude of the order parameter $t_{|\Psi|}$ and the relaxation time for the phase of the order parameter t_ϕ. They observed that phase slips are possible only when $t_\phi < t_{|\Psi|}$. A linearized Eilenberger equation in the dirty limit was studied, resembling a generalized TDGL equation with additional parameters related to inelastic electron-phonon collisions, which was first derived in [**54**]. They derived an approximate critical current via this equation and their results implied that there was a finite maximal oscillation period for the order parameter. In contrast, for weak links all oscillation periods diverged. The generalized GL equation used contained an additional parameter γ characterizing relative superconducting phase relaxation time (for us, $\gamma = 0$). For large γ values hysteresis was observed in the I-V curve. On a qualitative level, the effect of increasing parameter γ is similar to an increase in parameter u [**51**]. Correspondingly, we observed hysteresis when $u \gg 1$. The authors of [**55**] have done numerical analysis of a periodic array of weak links using the generalized TDGL equation. They showed I-V curves for different magnetic fields, however no analysis of the divergence of the period of vortices was presented.

We focus on a 1D superconductor, separated by a normal or weakly superconducting inhomogeneity. The complete system is modeled by a spatially dependent critical temperature $T_c(x)$. The weak link is created by a lower transition temperature inside an interval $I = [-r, r]$, which leads to a suppression of the order parameter. Here r is the inclusion radius. Below some critical current, this system relaxes to a stationary superconducting state, but above it, the superconductor exhibits a finite voltage with oscillatory behavior. Thermal fluctuations are initially not considered in this model and therefore does not cause a finite voltage in the superconducting state. The Josephson junction analysis is not applicable here. Indeed, since there is no dielectric contact between the two superconductor pieces, the phase should always be the same, implying zero voltage. We will show via simulations of the time-dependent Ginzburg-Landau equation, that the oscillations in the voltage is caused by phase slips in the center of the inclusion. The system approaches this state via a saddle-node bifurcation of two superconducting states, which occur at the critical current (at a saddle-node bifurcation stable and unstable stationary superconducting states annihilate and a periodic resistive state appears). The suppression of the order parameter in and near the weak link allows us to employ analytical methods in the vicinity of the critical current. We derive a reduced two-dimensional system governing the time evolution of the phase slip solution and describe a sequence of transitions between superconducting and dissipative states.

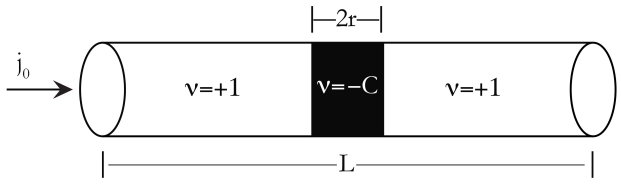

Figure 2.1. Weak-linked superconducting wire.

This chapter is organized as follows: section 2.2 describes the model, section 2.3 deals with the stationary case and estimates the critical current which is obtained from the saddle-node bifurcation condition. Sections 2.4-2.7 deal with the time periodic solutions, extracting a time-dependent system via weakly nonlinear analysis and then studying the simplified model to show that it exhibits the same qualitative behavior. In section 2.8, we interpret our analytical results, show the correspondence to the parameters of the superconductor and its effects on the phase slip state. Finally, section 2.9 gives closing remarks and ideas for further study.

2.2. Governing equations

We employ (1.20) with $\mathbf{A} \equiv 0$ (no external magnetic field) and apply periodic boundary conditions for Ψ. Since μ is on average an increasing function of x, there is necessarily a discontinuity at the boundary. This is resolved by making the following transformations:

$$\Psi = \tilde{\Psi} e^{iK(t)x} \tag{2.1a}$$

$$\mu = -Ax + \tilde{\mu}. \tag{2.1b}$$

Here, $\tilde{\mu}$ is a periodic function in x. Essentially, we are moving the growth of μ to the phase of Ψ. The growth in K now does not affect the magnitude. Indeed, this also allows us to *rewind* K through $K \to K - (2\pi/\Delta x)\lfloor K\Delta_x/2\pi \rfloor$ which will remove any error from rapid phase oscillations [**58**]. Inserting this into (1.20a) gives

$$u[\partial_t + ix(\partial_t K - A) + i\tilde{\mu}]\tilde{\Psi} = (\partial_x + iK)^2\tilde{\Psi} + [\nu(x) - |\tilde{\Psi}|^2]\tilde{\Psi}.$$

Setting $\partial_t K = A$ eliminates the linear term. Now inserting this into (1.20b), we have

$$j_0 = \Im(\tilde{\Psi}^* \partial_x \tilde{\Psi}) + |\tilde{\Psi}|^2 K + \partial_t K - \partial_x \tilde{\mu}.$$

Averaging this equation over space and noting that $\langle \tilde{\mu}_x \rangle = 0$ results in an ordinary differential equation (ODE) for K

$$\partial_t K + \left\langle |\tilde{\Psi}|^2 \right\rangle K = j_0 - \Im \left\langle \tilde{\Psi}^* \partial_x \tilde{\Psi} \right\rangle \equiv j_n.$$

For clearer notation, we now suppress the tildes, and we arrive at our modified TDGLE

$$u(\partial_t + i\mu)\Psi = (\partial_x + iK)^2 \Psi + [\nu(x) - |\Psi|^2]\Psi \tag{2.2a}$$

$$\mu_x = \Im(\Psi^* \partial_x \Psi) + \partial_t K + |\Psi|^2 K - j_0 \tag{2.2b}$$

$$j_n = \partial_t K + \left\langle |\Psi|^2 \right\rangle K. \tag{2.2c}$$

The integration domain is periodic with the period L. For the numerical integration, we generally took $L = 20$ and $u = 1$, however this was relaxed to see if the qualitative behavior changed. We verified that increasing L does not affect the results, however changing u can have a large effect (see section 2.8.3). To make the analysis simpler, we placed the weak link of length $2r$ symmetrically at the origin in the interval I. The inclusion's effect enters through the term $\nu(x)\Psi$ defined by

$$\nu(x) \equiv \begin{cases} 1, & x \notin I \\ -C, & x \in I \end{cases}. \tag{2.3}$$

Numerical analysis has shown that for $L \gg r$ there exists a critical current j_c, which is a function of r that separates the dynamics of this system. For $j_0 < j_c$, the system goes to a stationary superconducting state, while for $j_0 > j_c$ the system exhibits a dissipative state represented by periodic phase slips occurring in the center of the inclusion via a stable limit cycle. In the following sections, we explain these results analytically. We first provide an analytical approximation of the critical current. Next, we extract a coupled two-dimensional nonlinear system of ODEs from (1.20a) which describes qualitatively the correct behavior for suitable choices of the coefficients of the simplified system.

2.3. The stationary case $j_0 < j_c$

In the superconducting state with an applied current of $j_0 < j_c$, it can be shown that $\mu = 0$, (see appendix B.1 for details). To proceed, we rewrite (1.20a) in terms of amplitude and phase of the order parameter, i.e., $\Psi = Fe^{i\phi}$. Inserting this into (1.20a) and (1.20b), we look for stationary solutions and obtain

$$0 = \partial_x^2 F + [\nu(x) - (\partial_x \phi)^2 - F^2]F \tag{2.4a}$$

$$j_0 = F^2 \partial_x \phi. \tag{2.4b}$$

Plugging (2.4b) into (2.4a) gives the nonlinear ODE

$$0 = \partial_x^2 F + [\nu(x) - j_0^2 F^{-4} - F^2]F. \tag{2.5}$$

2.3.1. Large C approximation

We now assume a large C approximation, that is, the weak link strongly suppresses superconductivity in the inclusion (i.e. $C \gg j_0^2 F^{-4}$). This allows us to neglect the nonlinear term

and obtain a first order approximation of the solution of (2.4). From this we notice that (2.4a) has a first integral for both the inclusion domain and the superconducting domain. Asymptotic analysis of the size of these coefficients gives us a condition for j_c given by

$$j_c = \frac{1}{2\sqrt{C}} e^{-2r\sqrt{C}}, \tag{2.6}$$

for details see appendix B.2. Setting $C = 1$, we have that

$$j_c = \frac{1}{2} e^{-2r}. \tag{2.7}$$

Comparing this approximation with numerical simulations, we see that the large C approximation with $C = 1$ is in good agreement with the numerical solution (see Fig. 2.2). Thus, we derived that a weak link results in a exponential suppression of the critical current as a function of the inclusion width $2r$ and strength C. A similar result was obtained through a different method in [**44**]. However, our method is appealing for the simple generalization to multiple inclusions.

2.3.2. Multiple inclusions

Let $r_1, \ldots r_k$ be the radii of k inclusions in the domain. We have $k + 1$ superconducting domains and k normal domains, each with their own first integral constant. The analysis from appendix B.2 carries over and we expect the inclusion domain's first integral constant E_{I_k} to be approximately 0 for each k. This holds at the center of each respective inclusion, which each give different critical currents. However, when one is no longer satisfied, the system will no longer be satisfied and the global j_c is determined by the lowest local j_c,

which appears at the longest inclusion:

$$j_c \approx \frac{1}{2} e^{-2 \max_k r_k}. \tag{2.8}$$

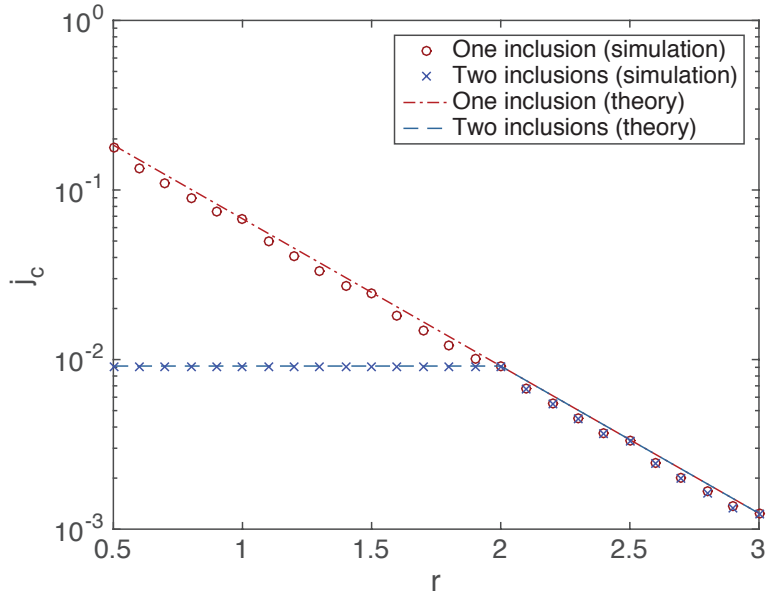

Figure 2.2. The critical current as a function of inclusion size using (2.7) (e.g. $C = 1$ with (2.6)). For the two inclusions, one inclusion is held fixed at $r = 2$. Above the curves the superconducting order parameter Ψ oscillates.

2.3.3. Linear stability analysis of the stationary state

Consider now a perturbation η of the stable state in the form $\Psi = (F+\eta)e^{i\phi}$. Inserting this into (1.20a)-(1.20b) and linearizing in η, we obtain with (2.4a) and (2.4b)

$$\begin{aligned} u\partial_t\eta = \partial_x^2\eta + \left(\nu - (\partial_x\phi)^2 - 2F^2\right)\eta + \\ i(2\partial_x\phi\partial_x\eta + \partial_x^2\phi\eta - uF\mu) - F^2\eta^* \end{aligned}$$

$$0 = \Im(F\partial_x\eta + 2iF\partial_x\phi\eta + \partial_x F\eta^*) - \partial_x\mu.$$

Separating $\eta(x,t) = (U+iV)e^{\lambda t}$ we obtain the following system (here λ is the growth rate)

$$\begin{aligned} 0 = \partial_x^2 U + \left(\nu - (\partial_x\phi)^2 - 3F^2 - \lambda\right)U - \\ (2\partial_x\phi\partial_x V + V\partial_x^2\phi) \end{aligned} \tag{2.9a}$$

$$\begin{aligned} 0 = \partial_x^2 V + \left(\nu - (\partial_x\phi)^2 - F^2 - \lambda\right)V + \\ (2\partial_x\phi\partial_x U + U\partial_x^2\phi) - uF\mu \end{aligned} \tag{2.9b}$$

$$\partial_x\mu = F\partial_x V - V\partial_x F + 2FU\partial_x\phi. \tag{2.9c}$$

This system along with (2.4a)-(2.4b) represents a 7 dimensional boundary-value eigenvalue problem which must be solved with appropriate boundary conditions. First, we note from (2.4a) that replacing $x \to -x$ leaves the differential equation unchanged. This with the reflection symmetry implies that F is an even function in x. This symmetry implies from (1.20b) that $\partial_x\phi$ and $\partial_x\mu$ are even in x. Thus $x \to -x$ changes $\Psi \to \Psi^*$. The action of this must be retained in the linearization implying that $\eta(-x)$ and $\eta^*(x)$ are both solutions. Hence U is even and V is odd in x. Furthermore, by symmetry it suffices to solve the

equations only on the half interval $(0, L/2)$ with the obtained natural boundary conditions from symmetry and the remaining conditions to be found by matching-shooting algorithm. To solve this we used a technique developed in [**46**,**59**]. In order to do so, we used a numerical matching-shooting solver for ODEs by beginning with a small domain (typically $L \sim 3$). We extracted the appropriate shooting boundary conditions and approximation for λ and used these as guesses for a larger system size. Iterating this process, we continued to L sufficiently large until the boundary conditions and λ were not changing significantly. The results are plotted in Fig. 2.3. We note here that $j_c \approx 0.0637$ obtained by the solver is only 6% away from the value obtained through direct numerical solution of the Ginzburg-Landau model. The step size used in the dynamic simulations were much larger ($\Delta x = 0.05$ compared to shooting solver with $\Delta x = 0.001$) and each had an associated numerical error. We checked if the error is independent of the solvers by analyzing the dynamic simulations j_c as a function of Δx in appendix B.4. We found that as $\Delta x \to 0$, we approached a similar value to that found from shooting. Thus, from Fig. 2.3 one sees that at the critical current, when stable ($\lambda < 0$) and unstable ($\lambda > 0$) solutions merge and annihilate, the corresponding linear system becomes degenerate. At the critical point it possesses two zero eigenvalues $\lambda_{1,2} = 0$. This degeneracy is taken into account through weakly nonlinear analysis.

2.4. Analysis of time-periodic solutions for $j_0 > j_c$

When the current is above the critical threshold, the above analysis breaks down. Numerical simulations indicate that the superconductor exhibits oscillations in the order parameter, where phase slips are now present (i.e. $|\Psi(0,t)| = 0$ for some t). In figure 2.4 we have estimated the period of oscillation T as a function of $j_0 - j_c \ll 1$. Numerical simulations

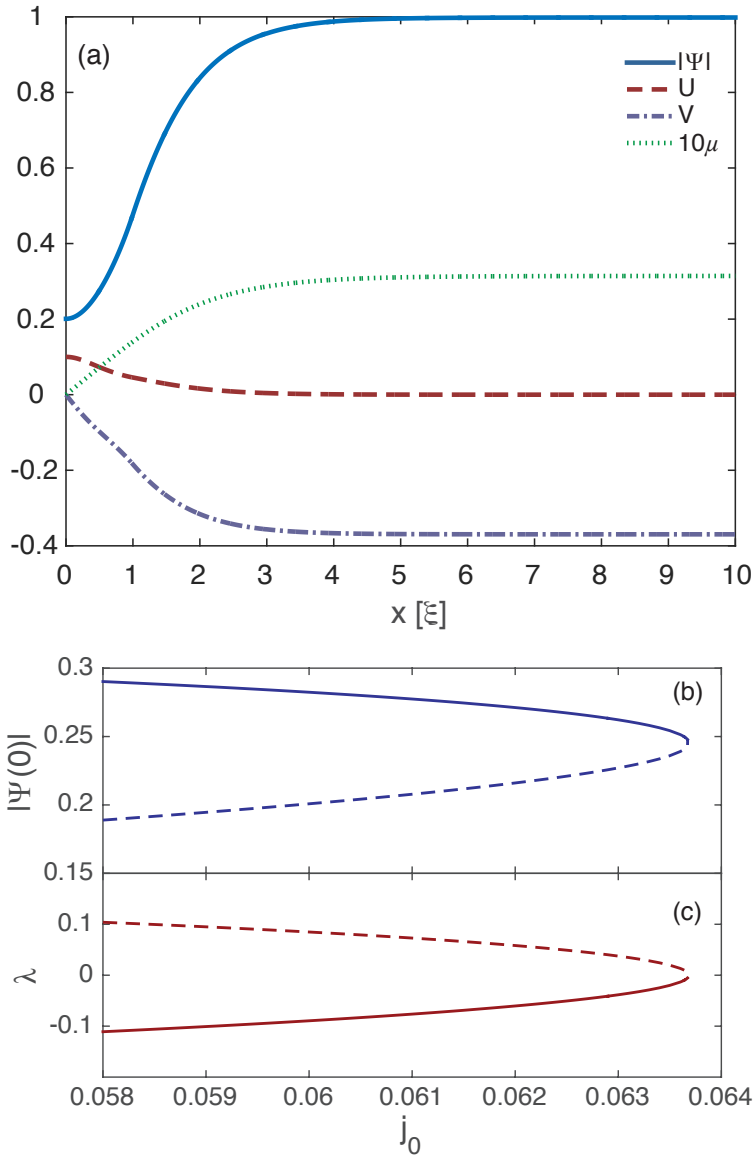

Figure 2.3. (a) Amplitude $|\Psi|$ and linearized solutions U, V, μ with $j_0 = 0.061$, $r = 1$. Plots (b) and (c) show the value of $|\Psi(0)|$ and location of the smallest eigenvalue respectively, for stable (solid line) and unstable (dashed line) solutions of eqs. (2.5), (2.9a)-(2.9c) for varying current. At the critical current the stable and unstable stationary (i.e. superconducting) solutions merge and annihilate.

indicate that the period $T \sim O(|j_0 - j_c|^{-1/2})$, which is indicative of an infinite-period bifurcation (IPB) at the point $j_0 = j_c$. In general for a bifurcation parameter R (e.g. current j)

the period of oscillations $T \sim O(|R - R_c|^{-1/2})$ for $|(R/R_c) - 1| \ll 1$ for an IPB [**60**]. We can see from figure 2.4 that an IPB is occurring at the critical value. In section 2.8.3, we show that for $u \gg 1$, we also observe hysteresis, behavior which is typical of a homoclinic bifurcation, a different mechanism through which a limit cycle can be destroyed [**60**].

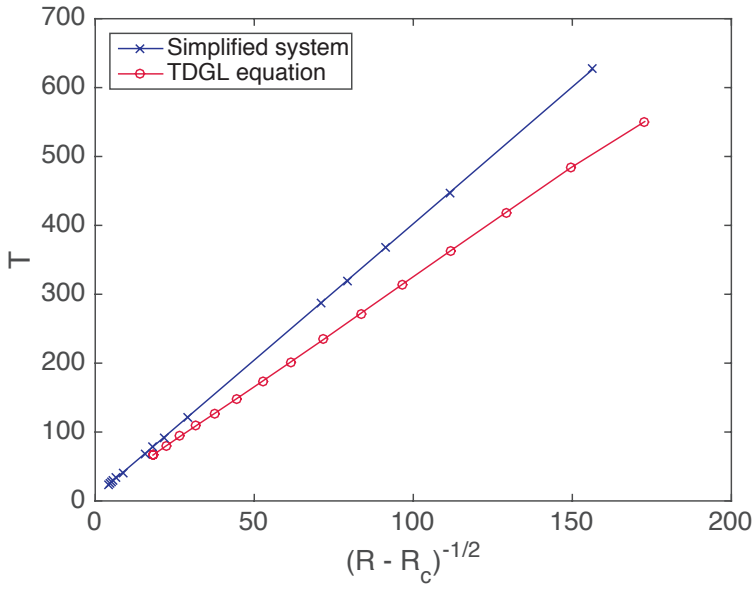

Figure 2.4. IPB analysis with $L = 20$ and $r = 1$. The critical current $j_c \approx 0.067$ was obtained via stable state calculation from Section 2.2. The simplified system derived in section 2.7 from weakly nonlinear analysis at $\gamma = -0.13$ with $c_{\text{IP}} \approx -0.565$ also exhibits an IPB. As expected, period $T \propto \frac{1}{\sqrt{R-R_c}}$ near the bifurcation point in both cases. Here R is current j in the TDGLE and parameter c in the simplified system.

Figure 2.5 shows time-voltage curves for $j_0 > j_c$. One clearly sees the period diverging as we approach the critical value. To calculate the current-period relationship, we ramped the current from an initial amount (typically $j_{\text{init}} < j_c$). If the system was stationary for a certain number of iterations, we increased the current. Once the system started oscillating, we calculated peaks in voltage, while skipping the first few to account for system equilibration. Then we averaged over the remaining peaks to obtain the period. We then used linear

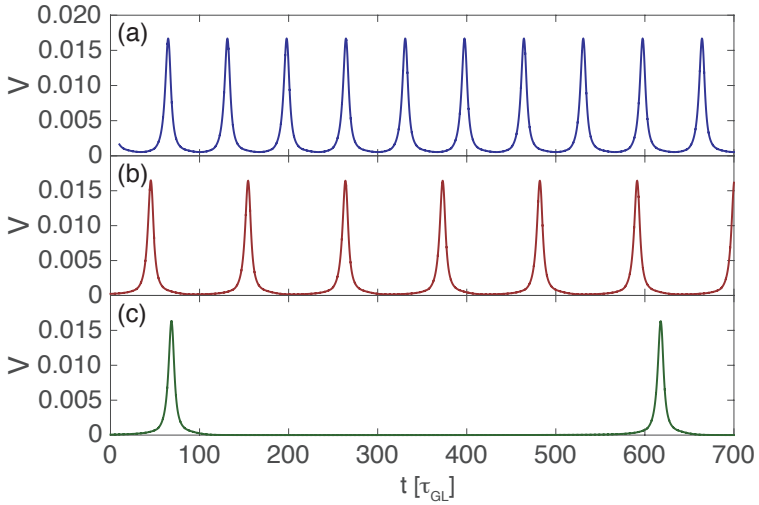

Figure 2.5. Plots (a)-(c) show dependence of voltage vs time above the critical current where $j_0 = 1.045 j_c$, $j_0 = 1.015 j_c$ and $j_0 = (1 + 10^{-6})\, j_c$, respectively and $j_c \approx 0.067$. System size $L = 20$, with an inclusion $r = 1$ in the center.

extrapolation to find the new current. For example, at the n^{th} step, we have the current j_n and corresponding period T_n. Let $m_n = \Delta T_n / \Delta j_n$, then suppose we want to find the current corresponding to a new period $T_{n+1} = (1 + \alpha) T_n$, with $\alpha > 0$. This is given by $j_{n+1} = j_n + \frac{\alpha T_n}{m_n}$. Figure 2.6 shows a similar period divergence of the oscillations of Ψ and the simplified model (see section 2.7).

2.5. Weakly nonlinear analysis

We now extract a coupled ODE system, which exhibits two dynamical possibilities. In the case $j_0 < j_c$, we show that the stationary (fixed) solution is stable, while in the opposite case, a stable limit cycle exists. It is of course possible that a bistability region can exist, which would lead to hysteric effects. Such effects have been observed in homogeneous superconductors [**45**, **51**, **52**]. For large u, we have also observed hysteric I-V curves and we show

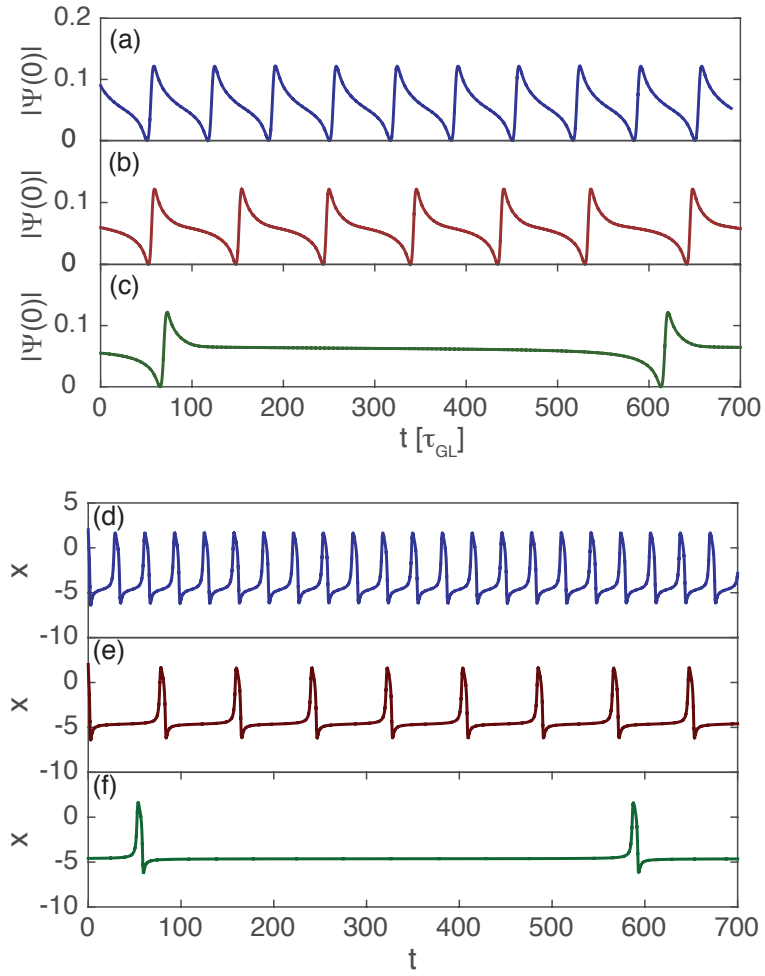

Figure 2.6. Plots (a)-(c) show dependence of $|\Psi(0)|$ vs time above the critical current where $j_0 = 1.045 j_c$, $j_0 = 1.015 j_c$ and $j_0 = (1 + 10^{-6})\, j_c$, respectively and $j_c \approx 0.067$. System size $L = 20$, with an inclusion $r = 1$ in the center. Plots (d)-(f) correspond to the simplified system Eqs. (2.14) where $\gamma = -0.13$ with $c_{\rm IP} \approx -0.565$ is the IPB threshold, with $c = 0.955 c_{\rm IP}$, $c = 0.985 c_{\rm IP}$ and $c = (1 - 10^{-5})\, c_{\rm IP}$.

that our extracted system contains both possibilities. The process is standard and is broken into these steps:

- Find stationary (basic) state $\Psi_0 = Fe^{i\phi}$ (it is already shown in Fig. 2.3)
- Perturb solution and solve linearized system.

- Extract weakly nonlinear effects from orthogonality condition.
- Show that certain conditions allow for a stable limit cycle to exist.

Though standard, the difficulty in this problem is that the basic state and linearization cannot be solved in closed form. Though we can approximate it to a certain degree, its region of validity is dependent on the radius of the inclusion r, the current j_0 and to a smaller extent, the system size L. Indeed, it is impractical to obtain it numerically since the solutions are sensitive to these choices. However, our analysis will assume that these are all known a priori and proceed through the framework. The simplified system is then obtained generally, and we show that the system exhibits the appropriate behavior for certain values in parameter space.

We expand Eqs. (2.2a)-(2.2c) near the stationary solution and near the critical point $j_0 = j_c + \epsilon$ with $\epsilon \ll 1$. The first order solution will be given by $\Psi_0 = Fe^{i\phi}$ (since $K = 0$, there is no electric potential in the super conducting state), in fact the initial transient would show exponential decay of $K \to e^{-\langle |\Psi|^2 \rangle t}$ and so $\mu = 0$ as expected. Let $\Psi = (F+\eta)e^{i\phi}$, where η, and time will now both slowly vary and be controlled by a small parameter $0 < \delta \ll 1$, whose size will be related to ϵ. The proper scaling will be determined from the ODE for K. Based on numerical simulations, we assume $K = O(\delta^2)$. We claim that we may regard K as constant in the relevant order of the perturbation method by the following argument. The perturbation η at first order is highly localized inside the inclusion and from this we argue

that

$$\begin{aligned}\langle|\Psi|^2\rangle &= \frac{1}{L}\int_0^L F^2 + 2F(\eta+\eta^*) + O(\eta^2)\,dx \\ &\approx \frac{1-j_0^2}{L}(L-r) + \frac{1}{L}\int_0^r F^2 + 2F(\eta+\eta^*)\,dx \\ &\approx 1 - j_0^2 + O\left(\frac{r}{L}\right).\end{aligned}$$

For $L \gg r$, we can regard $\langle|\Psi|^2\rangle$ as a constant. In a similar way all averaged quantities in the voltage equation can be neglected in the large superconductor domain limit. This analysis shows that the time-dependence of the voltage is slaved to the behavior of the order parameter Ψ. Therefore, we set K to a constant by

$$K = \frac{\epsilon}{1-j_0^2} + O\left(\frac{r}{L}\right). \tag{2.10}$$

From this, we extract the relation $\epsilon = \alpha\delta^2$ where $\alpha = \pm 1$. The linearized system at $\epsilon = 0$ has a degenerate eigenvalue as was shown previously in Fig. 2.3. Therefore we expand $\eta(x,\tau) = A(\tau)\eta_1(x) + \sqrt{\delta}[B(\tau)\eta_2(x) + z_1(x,\tau)] + \delta z_2(x,\tau)$ where $\mathcal{L}\eta_1 = 0$, $\mathcal{L}\eta_2 = \eta_1$ and $\mathcal{L}$ is the linear operator from (2.9). Using orthogonality conditions, we arrive at the coupled system

$$\begin{aligned}uA_\tau &= B + c_1A^2 \\ uB_\tau &= c_2AB + c_3A^3,\end{aligned} \tag{2.11}$$

where the coefficients c_k can be found through evaluating the integrals (see appendix B.5). We will show in section 2.6 why we chose to not include the constant K at this order. The general behavior is only captured correctly at $\epsilon = 0$. When $\epsilon \neq 0$ (i.e. $K \neq 0$) we do not see

a saddle-node bifurcation. To correct for this deficiency, higher order terms will be included. However, we can still gain some insight by analyzing this simplified system first.

2.6. Dynamical System Analysis

We begin with (2.11) by making a dimensionless system to analyze it more easily. We introduce the dimensionless variables

$$x = \frac{A}{L_A}, Y = \frac{B}{L_B}, t' = \frac{t}{uL_t}.$$

Inserting this into the system and defining the characteristic variables

$$L_A = \frac{1}{c_2 L_t}, \quad L_B = \frac{1}{c_2 L_t^2},$$

we arrive at the dimensionless system

$$\begin{aligned} \dot{X} &= Y + aX^2 \\ \dot{Y} &= XY + bX^3, \end{aligned} \tag{2.12}$$

where $a \equiv c_1/c_2$ and $b \equiv c_3/c_2^2$. The characteristic scale for time is arbitrary and is a consequence of the degeneracy in the system. The culprits are the X^2 term and XY terms whose combination of characteristic scales simultaneously vanish.

2.6.1. Fixed points and stability

There is only one fixed point located at the origin, provided that $a \neq b$. In this case there is a family of non-isolated fixed points along the parabola $Y = -aX^2$, however this case is not physical so we omit it. Next, we note the symmetry $t \to -t$ and $X \to -X$ of (2.12),

which implies that the linearized center located at the origin is robust (e.g. Nonlinear terms don't destroy qualitative behavior). We wish to see if this system exhibits closed orbits. The system is conservative if $a = -1/2$. In this case, a first integral can be obtained

$$H(X,Y) = \frac{1}{2}Y^2 - \frac{1}{2}X^2Y - \frac{1}{4}bX^4.$$

This has closed orbits provided that $b < -1/2$. So now that we have established the existence of closed orbits, we seek to gain insight if $a \neq -1/2$. We replace Y via the transformation

$$Y = \frac{U}{2a+1} - aX^2,$$

and rescale $X \to \frac{X}{2a+1}$ and obtain

$$\dot{X} = U \tag{2.13a}$$

$$\dot{U} = UX + \frac{b-a}{(2a+1)^2}X^3 \equiv UX + \gamma X^3. \tag{2.13b}$$

This leaves us with one independent parameter γ. We have already analyzed the case where $a = -1/2$ which, if $b < -1/2$ corresponds to $\gamma \to -\infty$ and has a family of closed orbits. If $b > -1/2$ then $\gamma \to \infty$ and we know this does not have closed orbits. Therefore, there must be some critical value of γ where this behavior changes. We seek a solution of (2.13) of the form $X = \tilde{C}t^{-1}$ with $\tilde{C}$ to be determined. Plugging this into the equation gives the condition

$$\tilde{C} = \frac{1 \pm \sqrt{1+8\gamma}}{2\gamma}.$$

These two solutions form a saddle-type connection only when they are equal which occurs at $\gamma_c = -1/8$ or in the original coefficients

$$b_c = -\frac{1}{8}(2a_c - 1)^2.$$

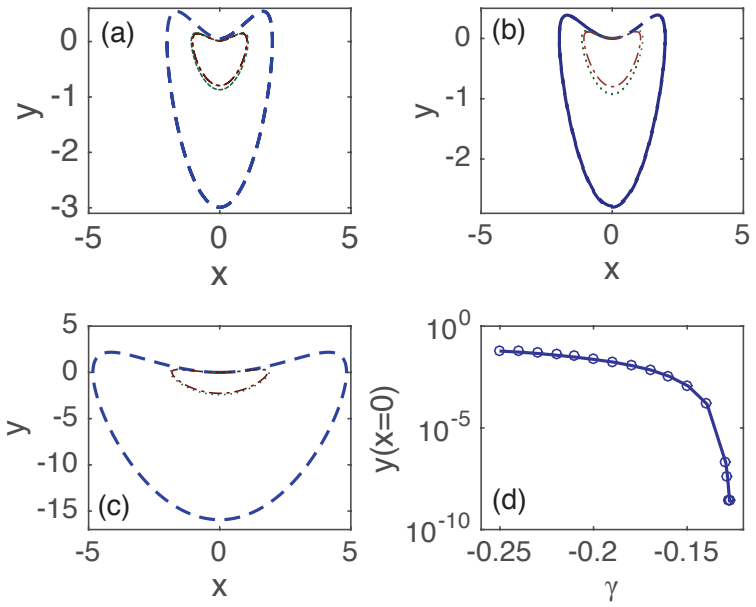

Figure 2.7. Plots (a)-(c) represent the solutions to (2.13) in the phase plane (X, Y) with $\gamma = -0.25, -0.15, -0.13$, respectively. There is a dimple near the origin where the trajectories are being squeezed down due to the homoclinic orbit at $\gamma_c = -1/8$. In plot (d), we display this dimple as a function of γ by taking 150 initial conditions and taking the average maximum.

This critical curve separates closed orbit solutions in the (a, b) parameter space. We have shown that the simplest (first order) system obtained, demonstrates a saddle-type infinite period bifurcation, however this creates an infinite family of closed orbits and a unique stable limit cycle is not obtained. The bottleneck is created near the origin (see Fig 2.7). Additionally, it does not have a saddle-node bifurcation which we expect to occur at $j_0 = j_c$. We note also that introducing K at this order, which adds a nonzero constant term to the

second ODE would still only have one fixed point and a constant at this order would destroy the degeneracy (and also any closed orbits) in a degenerate Hopf-type bifurcation when that constant crosses through zero. This should be corrected by including the next higher order cubic terms which will saturate and force the system to select one unique closed orbit.

The bottleneck created near the emergence of the saddle-node bifurcation is apparent in both the physical and simplified system (see figure 2.6). Note that the time scales need not be the same and careful treatment of the parameters in the simplified system (see section 2.4) would lead to the relation between the GL time and the time scale of the simplified system.

2.7. Full Dynamical System

We modify the system to include the next order cubic terms. In principle, we could obtain the next order terms by continuing the perturbation expansion, however, we chose to include the generic next higher order terms X^3, X^2Y, XY^2, and so on. We then found that the removal of some cubic terms e.g. XY^2, Y^3 slightly shifts the transitions boundaries but does not qualitatively change the bifurcation sequence. Therefore, we chose to keep the following system for our analysis:

$$\dot{X} = Y + aX^2 + w_1X^3 \tag{2.14a}$$

$$\dot{Y} = XY + bX^3 + c + w_2X^2Y, \tag{2.14b}$$

where we have introduced the new coefficients c, w_1, w_2. We will enforce $w_1, w_2 < 0$ to ensure the phase flow cannot escape to infinity, which would be a nonphysical state for this system.

2.7.1. Analysis

The fixed points cannot be found analytically in general since the equation involves a quintic polynomial. Instead we look to find the two critical curves which correspond to our system. We wish to find a saddle-node bifurcation curve and an infinite-period bifurcation as the current is varied. The saddle-node bifurcation involves the merging and annihilation of the stable and unstable stationary solutions. An infinite-period bifurcation is a saddle-node bifurcation which occurs on the limit cycle in the phase plane [**60**].

We first find the fixed points of (2.14). Using (2.14a), we obtain $Y^* = -(X^*)^2(a+w_1X^*)$, which leads to the quintic equation

$$f(X) \equiv w_1w_2X^5 + (w_1 + aw_2)X^4 + (a - b)X^3 - c = 0.$$

A saddle-node bifurcation occurs provided that $f(X^*) = f'(X^*) = 0$. The curve exists only if X^* is real which leads to the requirement that

$$b \geq a - \frac{4(w_1 + aw_2)^2}{15w_1w_2}.$$

To motivate our choice of parameters, we write this in terms of γ

$$\gamma \geq -\frac{4w_1}{15w_2}\left(\frac{\frac{w_2}{w_1}a + 1}{2a + 1}\right)^2.$$

If we set $w_2 = 2w_1$ we can eliminate a from the dependence on γ. Thus, we have that the saddle-node bifurcation exists only if $\gamma \geq -\frac{2}{15}$.

Writing the quintic now with $a = -1$ allows us to cast the quintic function solely in terms of w_1, γ and c.

$$2w_1^2X^5 - w_1X^4 - \gamma X^3 - c = 0.$$

The saddle node bifurcation then occurs along the curve

$$c_{\mathrm{SN}}(X^*) = \frac{1}{5}(X^*)^3\left[2\gamma + w_1(X^*)^2\right],$$

where X^* is given by

$$X^* = \frac{1 \pm \sqrt{1 + \frac{15}{2}\gamma}}{5w_1}.$$

The Jacobian of this system is

$$J = \begin{bmatrix} 2aX^* + 3w_1(X^*)^2 & 1 \\ Y^* + 3b(X^*)^2 + 2w_2X^*Y^* & X^* + w_2(X^*)^2 \end{bmatrix}.$$

A necessary condition for a Hopf bifurcation to occur is for a (un)stable spiral to change stability. This occurs when the trace of the Jacobian $\tau = X^*[2a + 1 + (3w_1 + w_2)X^*] = 0$ and the determinant $\Delta > 0$. For our analysis this implies that $X^* = 0$ or $X^* = (5w_1)^{-1}$. Of course our fixed point X^* must also satisfy the quintic equation. Inserting this gives a necessary condition and curve in (γ, c) space for a Hopf bifurcation

$$c_{\mathrm{Hopf}} = -\frac{1}{125w_1^3}\left(\gamma + \frac{3}{25}\right), \text{ or } c_{\mathrm{Hopf}} = 0.$$

The determinant is

$$\Delta = -\frac{1}{125w_1^2}(2 + 15\gamma).$$

Thus, the first Hopf bifurcation curve exists only when $\gamma < -2/15$. The second Hopf bifurcation is more complicated since $\Delta = 0$ and so nonlinear terms are important. The existence of that curve was found numerically.

2.7.2. Phase Diagram

In general, this system has many different ways in which a limit cycle is destroyed. Numerical experiments indicate that this can occur via a Hopf, cycle bifurcation, infinite period or homoclinic bifurcation. Slightly changing the parameters can change which bifurcation we obtain. From the preceding section, we motivated the choices $w_1 = -0.05, w_2 = -0.1, a = -1$ to keep our parameter space (γ, c). This leads to a generalized phase diagram of section 2.6. The Hopf and saddle-node bifurcation curves of figure 2.8 were obtained analytically. The

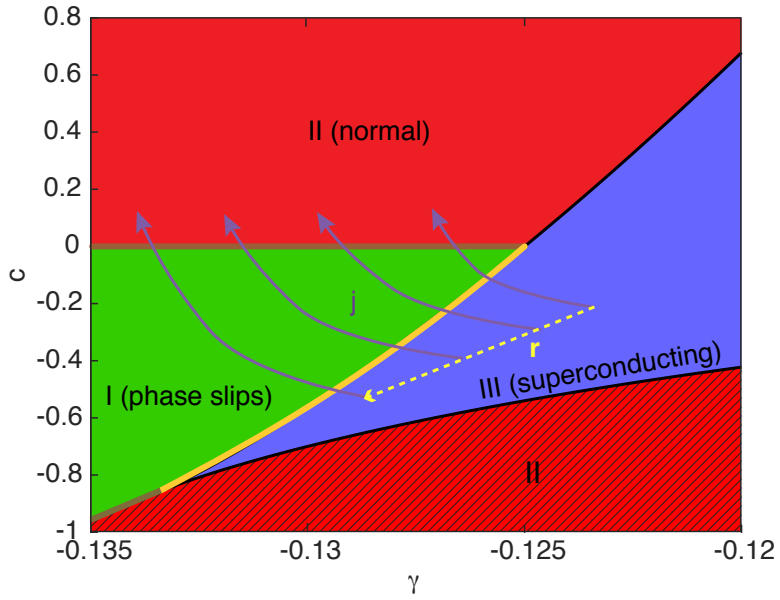

Figure 2.8. Phase diagram with $a = -1$, $\gamma = b + 1$, $w_1 = -0.05$, $w_2 = -0.1$. There is a stable limit cycle, i.e. periodic phase slips, (green) only in region I. Region II has one stable fixed point and region III has three fixed points. The saddle-node bifurcation (SNB) is boundary of the superconducting region. There is an IPB occurring along the yellow line. Possible trajectories in phase space are mapped with purple lines and the dashed yellow line corresponds to increasing r. Note that this phase diagram does not have a bistability region (with $u \gg 1$, we observed hysteresis, see section 2.8.3).

IPB curve $c_{\text{IP}} = c_{\text{IP}}(\gamma_{\text{IP}})$ was found numerically and for comparison is compared to the observed physical limit cycle in figures 2.4 and 2.6. Additionally, it was found numerically

that the HB in region III, did not exhibit the birth of a stable limit cycle. Possible trajectories of the superconductor through this phase diagram are shown with purple lines.

A more generic phase diagram with $w_2 \neq 2w_1$ is given in figure 2.9. Here, both an IPB and homoclinic bifurcation can destroy the limit cycle. The existence of the homoclinic bifurcation changes the morphology of the phase diagram to now include a bistability region in which the limit cycle (phase slips) and fixed point (superconducting state) coexist. This is particularly encouraging since we also found hysteresis for $u \gg 1$ (see section 2.8.3). Possible trajectories of the superconductor through this phase diagram are shown with purple lines.

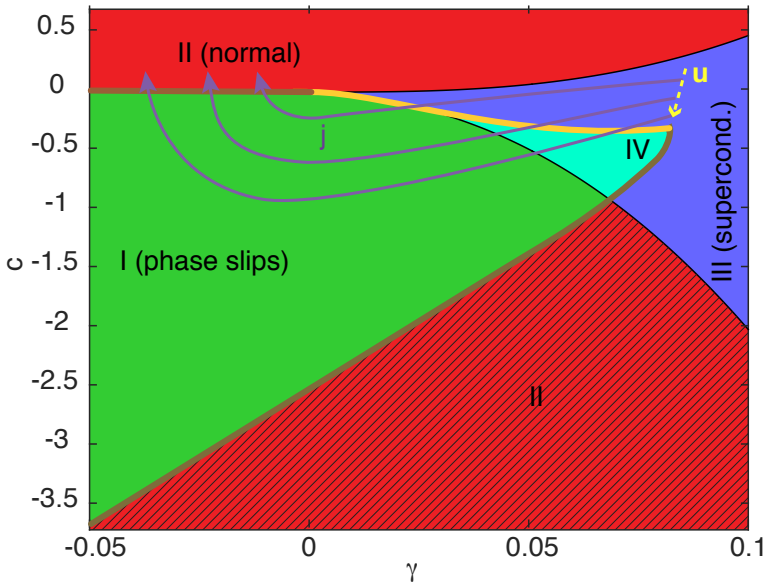

Figure 2.9. Phase diagram with $a = -1$, $\gamma = b + 1$, $w_1 = -0.09$, $w_2 = -0.08$. There is a stable limit cycle (green) in region I. Region II has one stable fixed point and region III has three fixed points. Region IV is a bistability region where a limit cycle and distant attractor coexist. The limit cycle is destroyed along the yellow line via a homoclinic bifurcation (a saddle point moving towards the limit cycle), and the dashed yellow line corresponds to increasing u. This homoclinic bifurcation line eventually merges with the SNB line (boundary of region III) and becomes an IPB (similar to Fig. 2.8).

2.8. Discussion

2.8.1. Sensitivity to temperature

To test the sensitivity of these phase slips to small thermal noise we modified (2.2) to include a small random noise term uniformly distributed between $[-T_f, T_f]$ at each point in space. Numerical simulations indicate that the system is stable to small fluctuations. The qualitative change is the existence of finite voltage in the superconducting state, however the critical current at which phase slips begin is unchanged.

2.8.2. Effect of parameter u

The parameter u characterizes the penetration of the electric field. In homogeneous wires, it has been found that hysteresis of the phase slip state exists for finite domains with $u \gg 1$ [**52**]. We analyzed $u = 0.01, 1, 10, 100$ with $L = 20$ and $r = 1$ (see figure 2.10). Another important quantity not yet discussed is that of the retrapping current j_r. The authors of [**52**] discuss the effect of u, numerically simulating the GL equation and finding a curve separating the hysteresis region of the I-V curve through some length dependent critical curve $u_{c2}(L)$. For our simulations of weak links, u small (for $r = 1$, $u < 30$ is small enough), $j_r = j_c$. However for $u \gg 1$, $j_r < j_c$, this leads to hysteresis in the I-V curve (see figure 2.11).

2.8.3. Physical quantities in simplified system

The phase diagram is in (γ, c) space. We can relate the important physical quantities u, r, j_0, L to γ, c by using appendix B.5. The coefficient c is strongly affected by the parameter u and the current j_0. Consider $j_0 < j_c$ and $u \to 0$, then we know that there is no voltage (i.e. $K = 0$), and $\alpha = -1$. This implies that $c \sim -u\zeta^2$ for some $\zeta(r, j_0, L)$ for

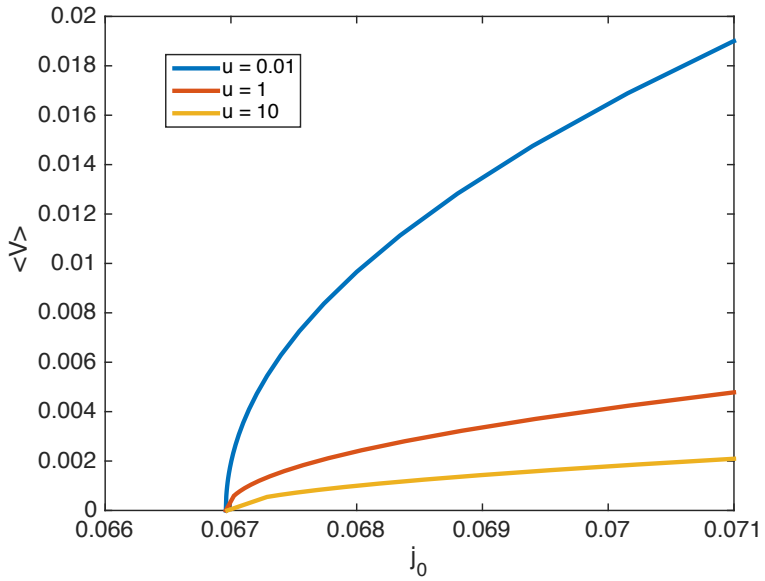

Figure 2.10. I-V curve with different $u = 0.01, 1, 10$. The critical current does not change, however the slope as $j_0 \to j_c$ increases as $u \to 0$. Additionally, $j_c = j_r$ (the reentrance current) for all u shown (no hysteresis).

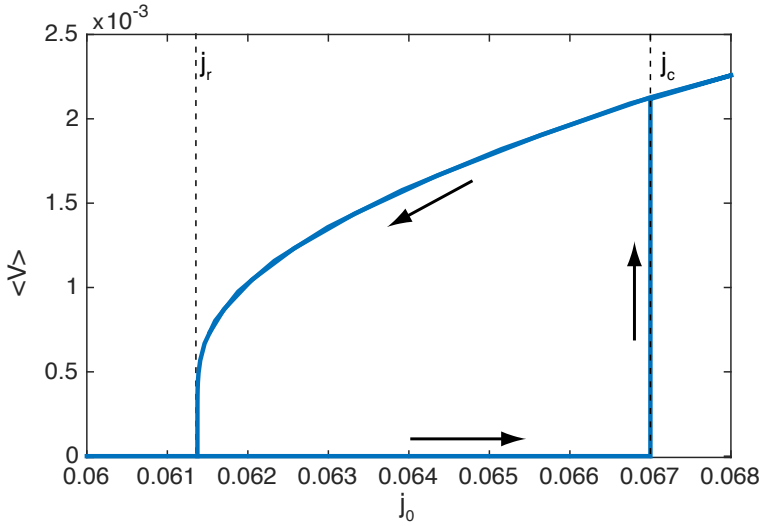

Figure 2.11. I-V curve for $u = 100$. Hysteresis is present, the saddle-node bifurcation still occurs at $j_c \approx 0.067$, however $j_r \approx 0.0614$ below which the superconducting state reappears.

small u. For $u >> 10$ we expect our initial trajectory to begin from a region in figure 2.9 where hysteresis is possible. Increasing the current $j_0 > j_c$ switches $\alpha = 1$ and $K \neq 0$, as j_0

continues to increase, R decreases and we expect c to change sign as we continue to increase it, which explains our motivation for the direction of trajectories. Increasing r lowers j_c and so we expect the trajectories to spend more time in the phase slip state, which leads us to expect that c decreases. A similar argument, leads us to assume the same holds for γ (see figure 2.8 and 2.9). The effects on γ are more complicated for the current and probably non-monotonous in a general case. From physical arguments we know that the trajectories must begin in the superconducting state and move into the phase slip state via either an IPB or homoclinic bifurcation. Comparing this to the phase diagrams, we see that as j_0 increases, γ must decrease. We also attempt to justify this from the terms in appendix B.5. We consider the scaling from section 2.6, which implied $b = c_3/c_2^2$. We noted that R is decreasing as j_0 increases (where R' is relatively unchanged). Again, employing appendix B.5, we see that c_3 is decreasing with the current since the positive terms involve R and the negative terms involve R'. Finally we use the fact that $b = c_3/c_2^2$ to deduce that b must be decreasing and since $\gamma = (b-a)/(2a+1)^2$, we see that γ is also decreasing with the current.

2.9. Conclusion

We have considered a weak-link superconductor qualitatively similar to other weak-link systems, but fundamentally different in mechanism. We demonstrated the existence of a superconducting state and a PSC periodic state separated by a critical current j_c. This current was calculated asymptotically and agrees very well with numerical simulations. We then extracted a coupled ODE system from the TDGL equations using weakly nonlinear theory and showed under certain choices of parameters, an infinite period bifurcation and homoclinic bifurcations can occur. This demonstrates that the dynamics of phase-slip behavior in weak

links described by the TDGL equations can be correctly captured by a simpler system of two coupled ordinary differential equations.

Further research is to extend this analysis to two dimensions. We anticipate additional transitions from phase slips occurring instantly inside the weak link to a more complicated dynamic regime involving phase slips and nucleation of vortex pairs, similar to that in [**45**]. Another interesting generalization is to include disorder in the transverse direction inside the weak link. Possibly, some of the vortices will be pinned in the weak link. It may in turn, lead to further suppression of the critical current. However, a more tractable problem is to first consider a homogenous 2D superconductor. We now cannot neglect a magnetic field (this was possible in 1D). Understanding the destruction of superconductivity in these cases is a required stepping stone before including 2D weak-links.

CHAPTER 3

Onset of vortices in thin superconducting strips

3.1. Preliminaries and governing equations

Finite resistance in massive 2D or 3D type-II superconductors with external field $\boldsymbol{H}_0 > \boldsymbol{H}_{c_1}$ is caused by the motion of vortices via the Lorentz force [**28**]. In narrow strips, with the transverse direction much smaller than ξ and λ, we have a limiting case which is quasi-one-dimensional. The mechanism of dissipation is through phase-slip centers (PSCs) [**41**, **42**, **48**, **49**]. In chapter 2, we discussed this mechanism analytically in weak-linked superconductors.

In this chapter, we consider a system whose geometry is intermediate of the two cases above, that is the thickness h and width d of the strip is such that $hd \ll \lambda^2$ and $h \gg \xi$. This ensures that we are in the strong type-II limit ($\kappa \gg 1$). We also assume that the external current and magnetic field are applied parallel and normal to the strip (see figure 3.1). This chapter is a modification of a previous result which had the field and current normal to each other rather than parallel [**61**], in that case dissipation was caused immediately by movement via the Lorentz force. In contrast, with parallel field and current, there can be no Lorentz force at first (vortices are aligned with the current). However, thermal fluctuations lead to random perturbations (e.g. bending of vortices), these bent regions then come under the influence of the Lorentz force, which move and ultimately lead to dissipation. We begin with the (1.20) with $\mathbf{A} \to 2\mathbf{A}$ and apply it to the geometry of figure 3.1. The fact that $\lambda^2 \gg hd$ ensures that we can neglect the magnetic field created by currents [**62**]. Define the origin to be at the center of the strip so that the edges of the strip are located at $(x, -d/2)$ and $(x, d/2)$.

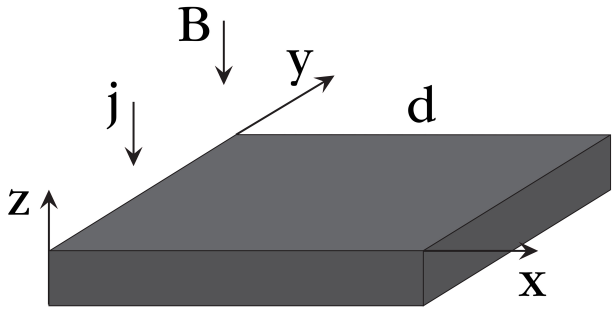

Figure 3.1. 2D superconductor. Magnetic field and current are applied normal to the strip.

Define $\boldsymbol{A} = (-By, 0, 0)$ where $\boldsymbol{B}$ and $\boldsymbol{j}$ are applied in the $-z$ direction with no-flux boundary conditions in the y direction.

3.2. Analysis

3.2.1. Linear stability

We look for stationary solutions of the TDGLE of the form $\Psi(y, z) = F(y)e^{ikz}$. Plugging this into (1.20a)-(1.20b), we immediately see that $\mu = 0$ which physically corresponds to no voltage in the superconducting state. We obtain a nonlinear equation for $F(y)$ and the current density

$$0 = \partial_y^2 F + (1 - F^2 - k^2 - 4B^2y^2)F \tag{3.1}$$

$$\boldsymbol{j}(y) = F(y)^2\langle 2By, 0, k\rangle. \tag{3.2}$$

For the case of weak magnetic fields $B \ll k/d$, we can expand $F = F_0 + BF_1 + B^2F_2 + \dots$ to obtain a perturbative solution of $F(y)$ and the mean current $j_0 = \frac{1}{d}\int_{-d/2}^{d/2} j(y)\, dy$. Inserting

the expansion in B into (3.1) to second order we have

$$\begin{aligned}
\mathcal{O}(1): &\quad F_0'' + (1 - F_0^2 - k^2)F_0 = 0, \\
\mathcal{O}(B): &\quad F_1'' - 2F_0^2 F_1 = 0, \\
\mathcal{O}(B^2): &\quad F_2'' - 2F_0^2 F_2 = 4F_0 y^2.
\end{aligned}$$

Inspection shows that a constant solution for F_0 is given by $F_0 = \sqrt{1-k^2}$. Plugging this into $\mathcal{O}(B)$ implies that $F_1 = 0$ (see lemma 3.2.1). Finally, solving the next order leads to our approximation,

$$F = F_0 + \left(\frac{\sqrt{2} d \cosh(\sqrt{2} F_0 y)}{F_0^2 \sinh(F_0 d/\sqrt{2})} - \frac{2y^2}{F_0} - \frac{2}{F_0^3} \right) B^2 + \mathcal{O}(B^3). \tag{3.3}$$

The mean current $\boldsymbol{j}_0$ can be approximated by plugging (3.3) into (3.2). By symmetry, the current is nonzero only in the z direction

$$j_{z0} = k \left\{ 1 - k^2 - \frac{1}{3} d^2 B^2 + \frac{1}{20} \frac{d^4 B^4}{1-k^2} \right\} + \mathcal{O}(1/d^2)$$

To analyze stability of this solution, we seek a perturbative solution of the TDGLE in the form $\Psi = [F(y) + \eta(y,z,t)]e^{ikz}$. Linearizing (1.20) with respect to η, μ, splitting real and imaginary parts of $\eta = \hat{a} + i\hat{b}$ where we define $(\hat{a}, \hat{b}, \mu) := [a(y), b(y), \mu(y)]e^{iqz+\omega t}$, we obtain

$$u\omega a = \partial_y^2 a + \{Z(y,q) - 2F^2\}a - 2ikqb, \tag{3.4a}$$

$$u\omega b = \partial_y^2 b + Z(y,q)b + 2ikqa - uF\mu, \tag{3.4b}$$

$$F\omega u b = \partial_y^2 \mu - (q^2 + uF^2)\mu, \tag{3.4c}$$

where $Z(y,q) := 1 - F^2 - k^2 - 4B^2y^2 - q^2$. This system represents the eigenvalue problem which has to be solved for the no-flux boundary conditions of a, b, μ. The stationary solution becomes unstable when $\omega(q) > 0$. At $\omega = 0$, the equation for μ in (3.4c) has only the trivial solution $\mu = 0$. Substituting this into (3.4) and redefining $ib \to b$. We have

$$\partial_y^2 a + \{Z(y,q) - 2F^2\}a - 2kqb = 0, \tag{3.5a}$$

$$\partial_y^2 b + Z(y,q)b - 2kqa = 0. \tag{3.5b}$$

Unless we use the asymptotic approximation for F, (3.5) generally can only be solved numerically. A particular (numerical) solution is represented in figure 3.2. The perturbation is highly localized and symmetric about the center of the strip. Of course, there is no Lorentz force here (since the current and magnetic field are parallel). The dissipation then cannot be caused by the motion of vortices but instead is caused by the motion of vortex and anti-vortex lines which begins at the sides and annihilate at the center. The critical curves are terminated at the depairing current $j_p = 2/\sqrt{27}$ which corresponds to $k_p = 1/\sqrt{3}$. In this region, a very weak magnetic field is needed to destroy superconductivity. In the relevant limit $d \gg 1$ (well-separated edges), we use adiabatic elimination to remove a from (3.5b). This leads to the following equation for b,

$$\partial_y^2 b = q^2 \left(1 - \frac{4k^2}{2(1 - k^2 - 2B^2y^2) + q^2}\right) b + \mathcal{O}(1/d^2). \tag{3.6}$$

The general solvability condition is given by integrating once which yields the following solvability condition along with the additional condition that its partial derivative with respect to q is 0. This will find the first q defined as q_c where the solutions will be non

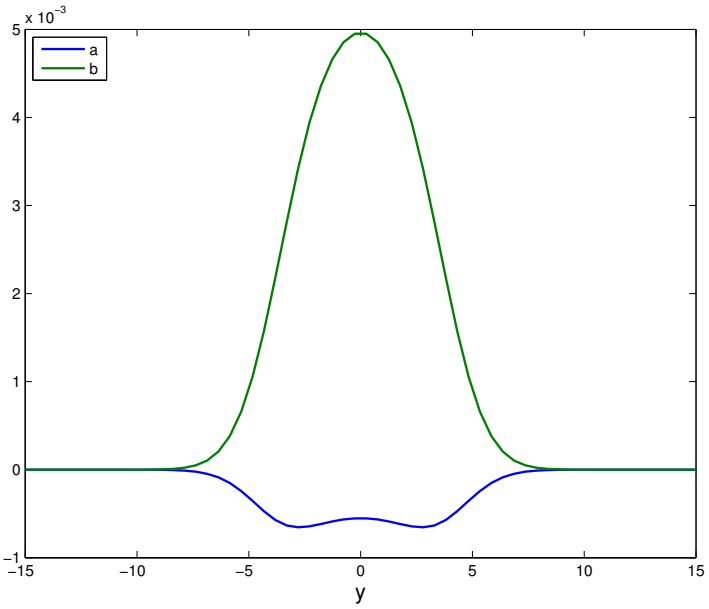

Figure 3.2. Perturbative solutions $a(y), b(y)$ as functions of y obtained by numerical solution with $B = 0.12$, $q = 0.28$, $k = 0.3$, $d = 30$.

trivial.

$$0 = Bd\tilde{q} - 4k^2 \operatorname{arctanh}\left(\frac{Bd}{\tilde{q}\sqrt{2}}\right), \tag{3.7a}$$

$$0 = Bq\left(1 + \frac{4\sqrt{2}k^2}{2\tilde{q}^2 + B^2d^2}\right), \tag{3.7b}$$

where $\tilde{q} = \sqrt{1 + q^2/2 - k^2}$. We immediately see in (3.7b) that the quantity in the parenthesis is strictly positive and hence $Bq = 0$. Noting that $B \equiv 0$ trivially satisfies the equation, this implies that $q_c = 0$ in this region. Then (3.7a) gives an approximation to the critical magnetic field curve.

3.2.2. Small q analysis

From the asymptotic expansion, it is clear that q can be treated as a small parameter. Linearizing about $q = 0$ in (3.5), we obtain

$$0 = \partial_y^2 a + \{Z(y,0) - 2F^2\}a,$$

$$0 = \partial_y^2 b + Z(y,0)b.$$

Note here that the second equation is exactly the same as (3.5b) and so $b = F$ is a solution to this equation. To solve the first equation we prove a short lemma here.

Lemma 3.2.1. Consider the following differential equation:

$$y'' - f(x)y = 0, \quad a < x < b$$

$$y'(a) = y'(b) = 0,$$

where $f(x) > 0$ for mostly all $x \in (a,b)$ (except for maybe a set of measure zero). Then $y = 0$ almost everywhere.

Proof. Multiplying both sides by y and then integrating we have

$$\int_a^b yy'' - f(x)y^2\,dx = 0$$

Integrating by parts once and employing the boundary conditions yields

$$\int_a^b (y')^2 + f(x)y^2\,dx = 0$$

Since $f(x) > 0$ almost everywhere, we see that $y' = y = 0$. This implies that $y = 0$ almost everywhere. $\square$

Employing the above lemma, we see that the first equation for a satisfies the condition required since $2F^2 - Z > 0$. Hence $a = 0$ at first order. Looking at the next order we see that

$$\partial_y^2 a + \{Z(y,0) - 2F^2\}a = 2kqF,$$

where we have substituted $b = F$. To solve this, we look back at the nonlinear equation and note that if we differentiate (3.1) with respect to k we obtain

$$\partial_y^2 F_k + \{Z(y,0) - 2F^2\}F_k = 2kF.$$

We immediately see, that this implies $a = qF_k$. Inserting this back into the equation for b to now include q^2 terms

$$Lb := \partial_y^2 b + Z(y,0)b = q^2 F + 2kq^2 F_k.$$

Using the self-adjoint property of the operator L, we have the solvability condition

$$q^2\langle F, F + 2kF_k\rangle = 0,$$

where the inner product is over the whole domain. This must hold for all $q \to 0$ and so our solvability condition can be written as

$$\int_{-d/2}^{d/2} F^2 + 2kFF_k \, dy = 0.$$

This can be further rewritten into the enlightening form

$$\frac{\partial}{\partial k}\left[\int_{-d/2}^{d/2} kF^2\,dy\right] = 0,$$

which we recognize as simply stating that $\frac{\partial j_z}{\partial k} = 0$. This condition was used to obtain the critical curve in figure 3.3. Above this critical curve, magnetic flux penetrates the superconductor at the sides of the domain.

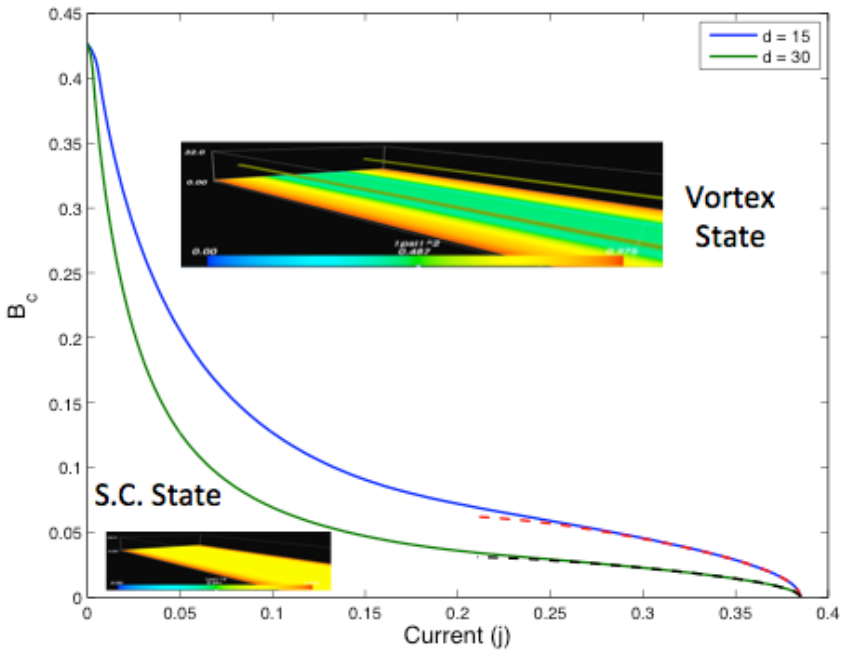

Figure 3.3. The critical curve for j_c vs. B_c. The dotted lines are the approximation from (3.7a).

3.2.3. Conclusion

I estimated a base (superconducting) state. Linear analysis showed that the perturbations were highly localized in the center in good agreement with numerical simulations, which show a decrease in the order parameter in the center of the strip. Next, I computed the critical

curve in the large d limit which motivated that the main instability was caused by long-wave instability. This led to the critical curve separating a purely superconducting material from the vortex state (dissipative). A second critical curve can be obtained in the future which would be above this curve and leads to the complete destruction of superconductivity.

More complicated geometries in general cannot be solved or even approximated analytically. The next chapter is devoted to analyzing some of these cases using numerical optimization to find the maximal current that can be obtained for given field. Impurities in superconductors act as pinning centers to trap vortices in place, restricting movement and allowing a larger current to be passed. Optimization of these parameters (e.g. best type of impurity, size, etc.) is thus extremely valuable research.

CHAPTER 4

Optimization

4.1. Introduction

The ability of superconductors to carry current without loss has extremely important energy and scientific consequences. With the recent development into manufacturing high-temperature type-II superconductors with higher critical temperatures, the energy applications has suddenly become a real possibility [**63**, **64**]. Another advantage of such superconductors is that the superconductivity is not completely suppressed by an external magnetic field. Instead of this, the magnetic field enters the superconducting matrix as elastic magnetic vortices [**65**] carrying quantized flux and each having diameter of superconducting coherence length. The highest amount of current that can be passed through a superconductor is known as the critical current and it strongly depends on vortex dynamics and its interaction with admixed non-superconducting inclusions. In particular, through a Lorentz force, vortex motion is induced. This motion creates heat dissipation, which ultimately leads to the destruction of the superconductivity. Thus, impeding this motion as much as possible, allows us to reach higher currents before superconductivity is lost. The small non-superconducting inclusions embedded in superconducting material possesses the ability to "pin" magnetic vortices in place, preventing their motion [**66**, **67**]. The efficiency of the landscape of the inclusions (pinning landscape) strongly depends on the shape and arrangement of individual inclusions. Indeed, bigger inclusions ensure a larger pinning force, but, at the same time, reduce effective cross-section of the superconductor needed for current flow. The optimal

pinning landscape depends on certain applications, particularly on the type of superconductor and on the value and direction of the applied magnetic field. The capability of systematic prediction of the optimal pinning landscape for energy and scientific applications aims at replacing the traditional try-and-error approach [**68**].

In this chapter we test several existent optimization strategies needed for the systematic improvement of the critical current in the superconducting wires. We compare the efficiency of global method (particle swarm optimization) and three local methods (Nelder-Mead method, pattern search, and adaptive pattern search) on a physically relevant critical current optimization problem. Also, we provide a detailed analysis of these methods on typical benchmark functions. We calculate the critical current for a given pinning landscape using implicit CUDA solver of time-dependent Ginzburg-Landau (TDGL) equation for type-II superconductors [**69**]. This model correctly describe vortex dynamics [**66**, **67**, **70**] in superconductors in the vicinity of the critical temperature and is capable of reproducing experimental critical currents for a given pinning landscape [**68**, **71**–**74**].

The chapter is organized as follows. In Sec. 4.2 we list optimization methods and provide their general description. In Sec. 4.3 we present the detailed comparison of the efficiency of the chosen optimization strategies on benchmark functions. In Sec. 4.4 we briefly describe the TDGL approach. In Sec. 4.5 we define a physically relevant optimization problem. In Sec. 4.6 we provide results of the optimization for the model problem. We summarize our results in Sec. 4.7.

4.2. Optimization methods and problem formulation

There are two classes of optimization methods: global search and local search. Examples of global search methods include: particle swarm optimization (PSO), cuckoo search, and

simulated annealing. For this paper, we elected to test only the PSO method because it was simple to implement and each individual particle in the swarm makes it a parallelizable method. We compare this global method against three local methods: pattern search (or coordinate descent), adaptive pattern search, and Nelder-Mead's simplex method. The pattern search and Nelder-Mead methods are standard local methods and their analysis, convergence properties, and pitfalls have been widely studied [**75**–**81**] . The adaptive pattern search method is a recent improvement on the traditional pattern search [**82**]. We can conceivably use more sophisticated methods, or routines, such as multi-level single linkage, which has random points initially, and collects them into multiple sets, depending on whether they are sufficiently close to an already found local optimum, if not it starts a local search [**83**, **84**]. The primary use behind this type of routine is to terminate local searches which are falling into the basin of attraction of a optimum point already found, which reduces computation time.

The general optimization problem for minimization of a function f can be formulated as follows

$$\mathbf{x}_{\text{opt}} = \arg\min_{\mathbf{x}\in\Omega}\{f(\mathbf{x})\}, \quad f_{\text{opt}} = \min_{\mathbf{x}\in\Omega}\{f(\mathbf{x})\}. \tag{4.1}$$

4.2.1. Particle swarm optimization

The PSO algorithm is a meta-heuristic global optimization algorithm [**85**, **86**]. Its convergence properties has been studied in a simplified form, where a single particle was used and the randomness in the algorithm was replaced by its averaged value [**87**]. It performed well on all test problems, but was typically outshone by the local methods when there was only a single minimum. The utility of this method was exploited with Rastrigin's function. The

importance of this test function came from the study of the physical problem of maximizing current for size and period of a square array of circular inclusions in a two-dimensional superconductor. It turned out, that many local maxima of J_c existed on integer values of the ratio of inclusions to vortices [**74**].

The PSO has four main control parameters given by $\mathbf{q} = \{S, \omega, \phi_p, \phi_g\}$, where S is the swarm size, ω the inertia of the individual particle (its tendency to move in its current direction), ϕ_p and ϕ_g are the weights for the particle to move towards its personal and global best, respectively.

The algorithm can be summarized in the following way: S random points (particles) are given, each with the same inertia ω. Each particle has a certain velocity v_i which governs its motion in parameter space. Each particle reports its best function value and location $\mathbf{p}_i$ and the best of these is the current global optimum $\mathbf{g}$. The particles velocities are then updated via the formula

$$\mathbf{v}_i = \omega \mathbf{v}_i + \phi_p r_p(\mathbf{p}_i - \mathbf{x}_i) + \phi_g r_g(\mathbf{g} - \mathbf{x}_i),$$

where $r_p, r_g \sim U(0,1)$. The particles then move to the new location $\mathbf{x}_i = \mathbf{x}_i + \mathbf{v}_i$.

Each particle is updated independently and does not need to wait for the other particles in the swarm to finish and so this method is easily parallelizable. In this way, a large architecture can make this method very efficient for high dimensional or multimodal problems where it is necessary for a large swarm size to ensure convergence. The biggest challenge is in determining an appropriate exit criterion for the routine. We use (i) the change, $|g - \langle g \rangle_K|$, in the best found objective function value, g, where $\langle \cdot \rangle_K$ is the averaging over last K iterations of PSO or (ii) the "size" of the swarm $\|\mathbf{x} - \langle \mathbf{x} \rangle_s\|_2$, where $\langle \cdot \rangle_s$ is the averaging over all particles in the swarm at the last iteration.

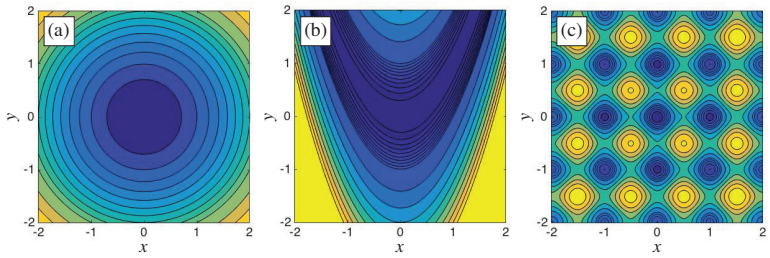

Figure 4.1. (a) Sphere, (b) Rosenbrock and (c) Rastrigin functions.

4.2.2. Pattern search

Pattern search is a straightforward method which starting from a random point, evaluates $2d + 1$ points (including the initial point) where d is the dimension, by moving a distance along each dimension in the search space, and chooses the point which improves the function the most. The method from then on evaluates $2d - 1$ points (it doesn't need to re-evaluate the point its on or the point it came from). If no improvement is made, the step size is reduced, and tries again. Once the step size is below some threshold, it exits. Along with its simplicity comes its ability to converge to non-stationary problems on some relatively simple problems [**88**] such as sphere function shown in Fig. 4.1(a). It has a particularly difficult time with functions with coordinate systems which are correlated — such as the Rosenbrock function shown in Fig. 4.1(b).

4.2.3. Adaptive pattern search

The adaptive pattern search method is a recent modification of pattern search [**82**]. The algorithm works similar to pattern search, however it attempts to create a better coordinate system as it searches the parameter space. It initially searches in each direction (pattern search), it then keeps the best $\mu < 2d + 1$ points to build a transformation of the coordinate system such that the new coordinates are as uncorrelated as possible. This transformation

is then updated after each sweep of all d dimensions ($2d-1$ points) and applied for the next iteration. There are four parameters $\mathbf{q} = \{\mu, \sigma, k_\mathrm{s}, k_\mathrm{u}\}$ which control the success and efficiency of this method – μ is the number of points used in the adaptive encoding function call, σ is the initial step size, and k_s (k_u) are the increase (decrease) of the step size upon successful (unsuccessful) improvement of the function value. The first parameter is the only one which is very restrictive as it is required to include at least one point (in this case the best point), up to $2d-1$. It was often found that μ scaled linearly with the dimension and typically $\mu = d$ was part of the optimal set. The utility of this method is best seen in the Rosenbrock function where pattern search takes $\sim 2 \times 10^3$ iterations in two-dimensional space, the adaptive pattern search method typically performed on the order of a 10^2 times better.

The key for the method's improved performance on Rosenbrock-type functions, is the adaptive encoding part of the algorithm. The function slowly builds a coordinate transformation that changes the search directions to be along the principal components [**82**]. At this point, the reader may question including pattern search if adaptive pattern search can only be an improvement in performance. While this is true, this exact reason also offers a useful way to measure the overall shape of the optimal solution. If adaptive pattern search is orders of magnitude better than pattern search, then the d-dimensional J_c surface is similar to the Rosenbrock function.

4.2.4. Nelder-Mead method

The Nelder-Mead method was chosen for its simplicity and its independence from being hindered by choice of coordinate system (it does not move along each dimension sequentially). This is most easily seen in comparing the methods against the Rosenbrock function. This

method utilizes a simplex, $d+1$ points in d dimensions (i.e. for $d=2$, we have a triangle). Over time, many variants of Nelder-Mead have been conceived [**89**,**90**], however, we followed the algorithm described in [**91**].

The initial points (or vertices) are chosen and the function value obtained. We then order the vertices in terms of function value and calculate the centroid of all but the worst point. This point is then replaced by one of three new possible points. First a reflection $\mathbf{x}_r$ about the centroid from the worst point is evaluated, if this function value is better than the second worst point, replace the deleted point with this point. If this point is better than the best point, the method expands its search in that direction, picking a new point $\mathbf{x}_e$. If this point is the best we add it to the simplex, otherwise we add $\mathbf{x}_r$. If $\mathbf{x}_r$ did not improve the simplex, we contract the simplex $\mathbf{x}_c$ and replace the worst point if the function value of $\mathbf{x}_c$ is better. The biggest problem with Nelder-Mead is the convergence to non-stationary points, couple this with the relatively expensive function evaluations and potentially multi-minima d-dimensional objective function surface which can quickly lead to this method becoming inefficient.

4.3. Testing on benchmark functions

The above mentioned optimization methods were tested on three benchmark functions shown in Fig. 4.1: sphere function, Rosenbrock's function, and Rastrigin's function. These were chosen for their relation to previous current surfaces obtained on simple sets of parameters. We expect scenarios where either a single optimum or multiple small ones and one global one exists. The Rosenbrock function was used because of its similarity to the optimization for the number of inclusions. This strange J_c surface can be removed by the change of variables from inclusion number to volume fraction. Though we are able to remove

it in that case, we cannot be sure we will find the appropriate transform which makes the function easier to optimize or exclude it from other geometries and so we account for it with the topologically similar Rosenbrock function.

The study was broken up as follows: optimal parameters for the PSO and adaptive pattern search are obtained using the three benchmark functions. These were found by overlaying the optimization routine with PSO. For example, adaptive pattern search has tuning parameters $\mathbf{q} = \{\mu, k_{\mathrm{s}}, k_{\mathrm{u}}, \sigma\}$, where the explanation of these parameters is deferred to its respective section. The nested PSO algorithm then searches through parameter space in an attempt to find the optimal parameters for the algorithm. First, we consider the function

$$\bar{E}_f(\mathbf{q}) = \frac{1}{M} \sum_{i=1}^{M} E_{f,i}(\mathbf{q}), \tag{4.2}$$

where $E_{f,i}$ is the number of function evaluations required to find the global optimum for a function f, $\mathbf{q}$ are the parameters used for the optimization routine, and M are the total number of simulations which successfully found the global optimum. However, this is not the most useful measure as it does not take into account the rate at which the algorithm successfully finds the global optimum. Indeed, define $r_f(\mathbf{q})$ as the rate at which a correct solution is found (to within a specified tolerance) for a set of the method parameters $\mathbf{q}$. Then, it may turn out that $\bar{E}_f(\mathbf{q}_1) < \bar{E}_f(\mathbf{q}_2)$, but $r_f(\mathbf{q}_1) \ll r_f(\mathbf{q}_2)$ for some certain $\mathbf{q}_1$ and $\mathbf{q}_2$. It then may happen that we would require many more runs for $\mathbf{q}_1$ so that $\mathbf{q}_2$ was actually the better choice. Therefore, we chose the optimal parameters $\mathbf{q}_{\mathrm{opt}}$ for each optimization

method by solving the following auxiliary optimization problem:

$$\mathbf{q}_{\text{opt}} = \arg\min_{\mathbf{q}}\{F_{f,\alpha}(\mathbf{q})\}, \tag{4.3a}$$

$$F_{f,\alpha}(\mathbf{q}) = N_{f,\alpha}(\mathbf{q})\bar{E}_f(\mathbf{q}) \tag{4.3b}$$

$$N_{f,\alpha}(\mathbf{q}) = \frac{\log(1-\alpha)}{\log[1-r_f(\mathbf{q})]}, \tag{4.3c}$$

where $N_{f,\alpha}$ is the number of iterations needed to be at least $1-\alpha$ sure that we have found the global solution. We use $\alpha = 0.99$ in this work. The dimensionality in the function was absorbed into the optimization problem, and an analysis of the problem dimensionality and number of iterations was tested.

We sampled 10^3 different starting configurations $\mathbf{x}$, where $x_i \in [-10, 10]$ for the algorithms and then ran the nested PSO algorithm 10 times for each dimension and each benchmark function. The best parameters were recorded. Once these were obtained, we tested all the algorithms mentioned using the same starting points and compared the performance. The algorithms each had a maximum iteration number of $10^3 d^2$ where $d = |\Omega|$ is the dimension of the original optimization problem (4.1), and would exit out of the loop with a tolerance of $10^{-3}d^2$.

4.3.1. Sphere function.

The sphere function is defined by

$$f(\mathbf{x}) = \sum_{i=1}^{n} x_i^2.$$

Tables 4.1 and 4.2 show a tabulated view of the effectiveness of the chosen methods to solve this function in the given number of iterations. The function is very simple and the

coordinates are uncorrelated. Thus, a wide range of parameters actually turned out to be similarly effective. A comparison of the method's performances is presented in figure 4.2 by using 100 random initial starting configurations and employing equation (4.3).

d	$\{S$	ω	ϕ_{p}	$\phi_{\mathrm{g}}\}$	$F_{f,\alpha}$
2	5	0.22	0.93	1.93	84.7
3	5	0.36	1.35	1.68	131.3
4	8	0.23	0.80	1.96	183.7
5	10	0.18	0.99	1.96	235.5
6	9	0.36	1.55	1.55	290.5
7	12	0.27	1.18	1.75	348.4

Table 4.1. Optimal PSO parameters $\mathbf{q}_{\mathrm{opt}} = \{S, \omega, \phi_{\mathrm{p}}, \phi_{\mathrm{g}}\}$ and $F_{f,\alpha}(\mathbf{q}_{\mathrm{opt}})$ for the sphere function.

d	$\{\mu$	σ	k_{s}	$k_{\mathrm{u}}\}$	$F_{f,\alpha}$
2	1	0.21	1.00	0.24	44.3
3	2	0.22	1.00	0.33	64.0
4	4	0.12	1.00	0.29	82.0
5	2	0.36	1.00	0.29	99.5
6	3	0.21	1.00	0.33	114.9
7	13	0.25	1.00	0.33	128.7

Table 4.2. Optimal adaptive pattern search parameters $\mathbf{q}_{\mathrm{opt}} = \{\mu, \sigma, k_{\mathrm{s}}, k_{\mathrm{u}}\}$ and $F_{f,\alpha}(\mathbf{q}_{\mathrm{opt}})$ for the sphere function.

4.3.2. Rosenbrock function.

The Rosenbrock function is a standard test for optimization methods and is given by

$$f(\mathbf{x}) = \sum_{i=1}^{n-1} \big[100(x_{i+1} - x_i^2)^2 + (1 - x_i)^2\big].$$

Optimization of this function demonstrates the utility of coordinate independent local search methods (i.e. Nelder-Mead, adaptive pattern search). This is due to the fact that the

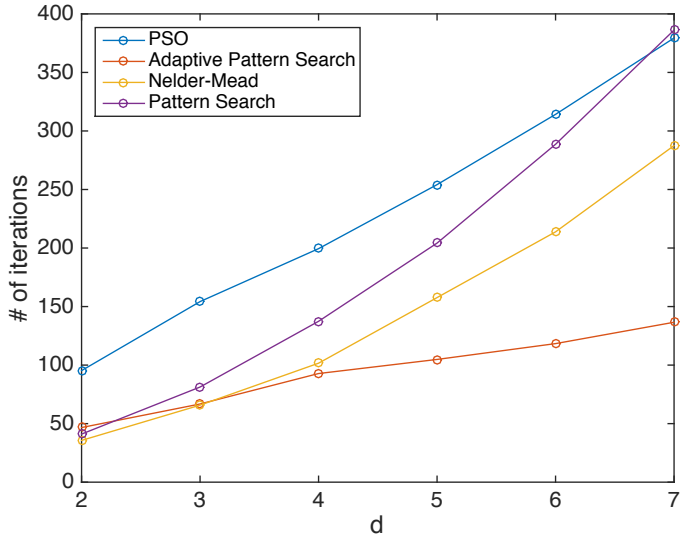

Figure 4.2. A comparison of the each methods efficiency as a function of dimension for the sphere function. Here it is clear that adaptive pattern search performs the best.

minimum is contained inside a parabolic valley which requires constant shrinking of the step size for pattern search to make progress. Consider the 2D case

$$f(x, y) = 100(y - x^2)^2 + (1 - x)^2,$$

the change of variables to the (u, v) plane given by $u = 1 - x$ and $v = y - x^2$ leads to elliptical level sets $g(u, v) = u^2 + 100v^2$, which is much more favorable to coordinate-dependent methods. In practice it is usually difficult or impossible to find the appropriate transform converting to elliptical level sets. Nevertheless, this gives a useful test of the morphology of the surface of J_c by comparing iterations between coordinate-dependent and coordinate-independent methods. We can tell if the surface is of a Rosenbrock-type if pattern search takes a large number of iterations compared to an independent coordinate method such as adaptive pattern search or Nelder-Mead.

Tables 4.3 and 4.4 show the effectiveness of the PSO and adaptive pattern search methods to minimize Rosenbrock function in the given number of iterations. As we can see from the table, the PSO method is not practical for dimensions $d > 5$, and for our practical purposes is almost entirely unusable because of how expensive our function evaluations are. The optimization of parameters for PSO have revealed that the dimensionality and swarm size are (perhaps not surprisingly) correlated. As the dimensionality increases, the optimal swarm size (holding other parameters fixed) increases. To verify this we sampled 100 random starting points for swarm sizes between 10–200, the results are shown in figure 4.3.

d	$\{S$	ω	ϕ_{p}	$\phi_{\mathrm{g}}\}$	$F_{f,\alpha}$	r_f	$N_{f,\alpha}$
2	28	0.25	−0.21	1.58	823	0.99	1
3	34	0.29	−0.15	1.73	2942	0.95	2
4	29	0.35	−0.17	1.59	9352	0.73	4
5	44	0.28	−0.21	1.67	19113	0.61	5

Table 4.3. Optimal PSO parameters $\mathbf{q}_{\mathrm{opt}} = \{S, \omega, \phi_{\mathrm{p}}, \phi_{\mathrm{g}}\}$, $F_{f,\alpha}(\mathbf{q}_{\mathrm{opt}})$, $r_f(\mathbf{q}_{\mathrm{opt}})$, and $N_{f,\alpha}(\mathbf{q}_{\mathrm{opt}})$ for the Rosenbrock function.

d	$\{\mu$	σ	k_{s}	$k_{\mathrm{u}}\}$	$F_{f,\alpha}$	r_f	$N_{f,\alpha}$
2	2	0.28	1.67	0.43	227	1.00	1
3	2	0.15	1.48	0.46	392	1.00	1
4	2	0.22	1.81	0.38	781	0.94	2
5	2	0.14	1.71	0.45	1384	0.92	2
6	6	0.37	1.96	0.36	1775	0.93	2

Table 4.4. Optimal adaptive pattern search parameters $\mathbf{q}_{\mathrm{opt}} = \{\mu, \sigma, k_{\mathrm{s}}, k_{\mathrm{u}}\}$, $F_{f,\alpha}(\mathbf{q}_{\mathrm{opt}})$, $r_f(\mathbf{q}_{\mathrm{opt}})$, and $N_{f,\alpha}(\mathbf{q}_{\mathrm{opt}})$ for the Rosenbrock function.

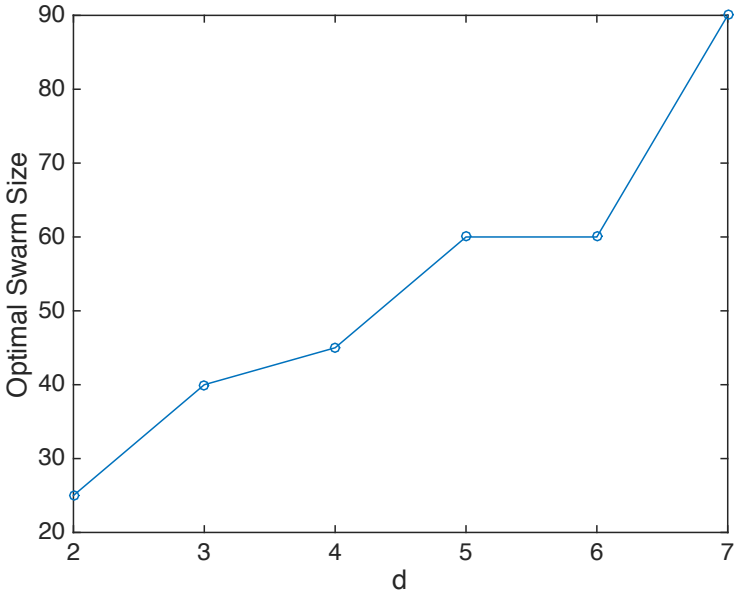

Figure 4.3. The optimal swarm size as a function of dimension, we incremented the swarm size by 5 or 10 and is indicated by the error bars in the figure.

4.3.3. Rastrigin function.

The optimal result for the Rastrigin function is very useful since we know that our general physical problem may often have a similar landscape. It is defined by

$$f(\mathbf{x}) = 10n + \sum_{i=1}^{n} \left[x_i^2 - 10\cos(2\pi x_i) \right].$$

This is where PSO perform particularly well over the local search methods. Table 4.5 shows its effectiveness to solve Rastrigin function in the given number of iterations.

d	$\{S$	ω	ϕ_{p}	$\phi_{\mathrm{g}}\}$	$F_{f,\alpha}$	r_f	$N_{f,\alpha}$
2	32	0.25	2.00	1.00	618	0.99	1
3	23	0.58	2.08	0.89	2767	0.91	2
4	25	0.58	2.21	0.75	9609	0.67	5

Table 4.5. Optimal PSO parameters $\mathbf{q}_{\mathrm{opt}} = \{S, \omega, \phi_{\mathrm{p}}, \phi_{\mathrm{g}}\}$, $F_{f,\alpha}(\mathbf{q}_{\mathrm{opt}})$, $r_f(\mathbf{q}_{\mathrm{opt}})$, and $N_{f,\alpha}(\mathbf{q}_{\mathrm{opt}})$ for Rastrigin function.

4.4. Model of superconductor

We use the TDGL equation for the superconducting order parameter $\psi = \psi(\mathbf{r}, t)$,

$$(\partial_t + i\mu)\psi = \epsilon(\mathbf{r})\psi - |\psi|^2\psi + (\nabla - i\mathbf{A})^2\psi + \zeta(\mathbf{r}, t), \tag{4.4}$$

as the main tool for the numerical analysis of vortex dynamics in strong type-II superconductors. Here $\mu = \mu(\mathbf{r}, t)$ is the chemical potential, $\mathbf{A}$ is the vector potential associated with the external magnetic field $\mathbf{B}$ as $\mathbf{B} = \nabla \times \mathbf{A}$, and $\zeta(\mathbf{r}, t)$ is the temperature-dependent δ-correlated Langevin term. The unit of length is given by the superconducting coherence length ξ and the unit of magnetic field is given by the upper critical field H_{c2}. See [**69**] for the details of TDGL model implementation. The current density is given by the expression

$$\mathbf{J} = \mathrm{Im}\big[\psi^*(\nabla - i\mathbf{A})\psi\big] - \nabla\mu. \tag{4.5}$$

To determine the critical current value — maximal current, which can flow through the superconductor without dissipation, — we use a finite-electrical-field criterion. Specifically, we chose certain small external electric fields, $E_{\mathrm{c}} = 10^{-4}$, and adjusted the external current, J, current to keep this electrical-field criterion on average. The time-averaged value of external current over steady state gives the critical current, $J_{\mathrm{c}} = \langle J \rangle$.

The critical current in a presence of an external magnetic field is mostly defined by inclusion patterns (small non-superconducting islands in superconductor): both by inclusion size (typically a few ξ) and their (sometimes rather non-trivial) spatial distribution. The foundational mechanism here is the pinning of magnetic vortices on non-superconductive inclusions and preventing vortices from moving under the influence of the Lorentz force, $\mathbf{f}_{\mathrm{L}} = \mathbf{J} \times \mathbf{B}$.

The pinning landscape is characterized by the set of parameters $\mathbf{x}$, which corresponds to the objective function

$$f(\mathbf{x}) = -J_{\mathrm{c}}(\mathbf{x}). \tag{4.6}$$

Each element $\mathbf{x}$ of the parameter space Ω describes the pinning landscape in the superconductor. e.g. the shape of each defect and their spatial distribution. The optimal configuration of the defects $\mathbf{x}_{\mathrm{opt}}$ corresponds to the minimization of the objective function, $f_{\mathrm{opt}} = f(\mathbf{x}_{\mathrm{opt}})$.

Knowledge of the shape and behavior of the function $J_{\mathrm{c}}(\mathbf{x})$ is not known *a priori*. If we consider, for example, the random placing of inclusions in the domain, depending on the particular placement, can yield slightly different values for J_{c}. We expect, as the number of random simulations tends to infinity, the J_{c} approaches the true value, however the finite number of trials can create a non smooth J_{c} surface. This can create some difficulties for the local methods to converge to the global solution, but for this particular physical problem, did not cause too many problems. The modification of these local methods to multi-level starts should be sufficient for these types of problems to overcome the noise.

4.5. Optimization of critical current

The general definition of the pinning landscape optimization problem is given by Eq. (4.1). Each set of pinning landscape parameters $\mathbf{x}$ describe the size of individual defect and defect density in the superconductor. Typically the pinning landscape in the superconductor is described by approximately from $d = 2$ to 8 parameters. For example, the three-dimensional superconductor with randomly placed spherical inclusions can be described by the density of inclusions ρ and diameter d of each of them, [**92**] $\mathbf{x} = (\rho, d)$. Another example is the addition of columnar defects of fixed diameter by high-energy heavy-ion irradiation to the

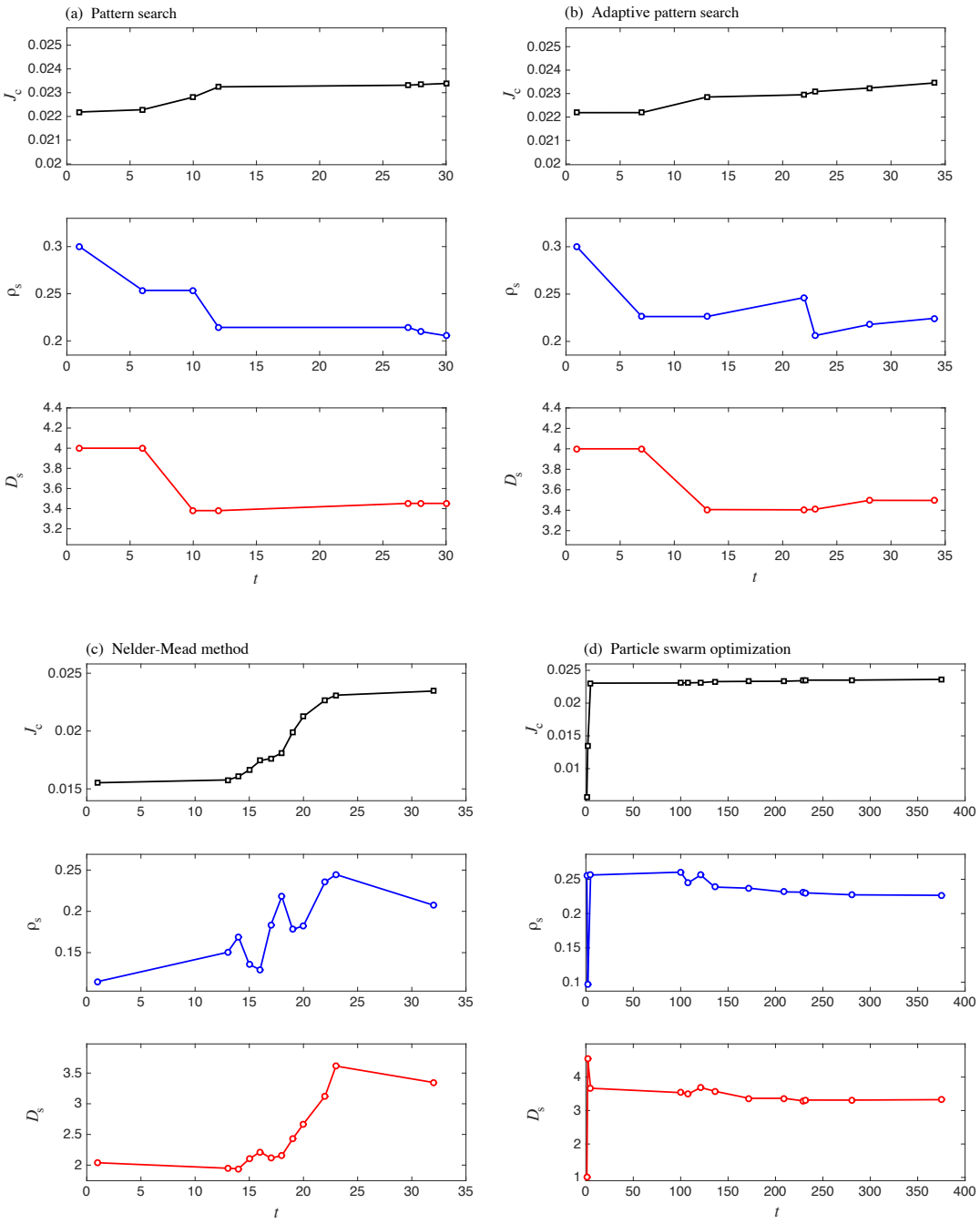

Figure 4.4. Optimization paths for the two-parameter optimization problem (spheres) as a function of iteration number t, see Eq. (4.7a), using (a) pattern search, (b) adaptive pattern search, (c) Nelder-Mead method, and (d) particle swarm optimization. All local methods converged to the same point, a good indication that it is the global optimum. Note PSO exit criterion causes over 300 iterations for marginal improvement.

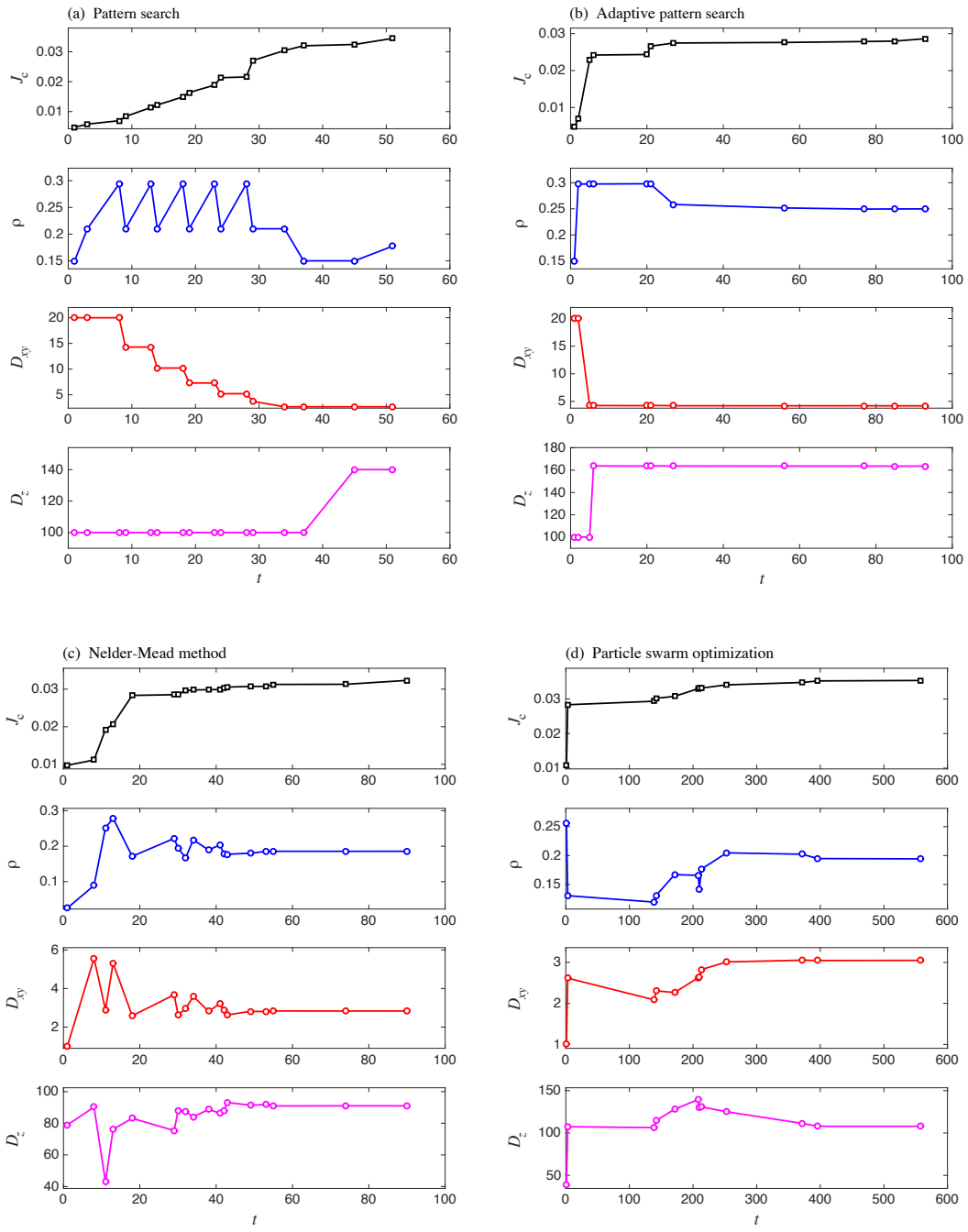

Figure 4.5. Optimization paths for the three-parameter optimization problem (ellipsoids) as a function of iteration number t, see Eq. (4.7b), using (a) pattern search, (b) adaptive pattern search, (c) Nelder-Mead method, and (d) particle swarm optimization. $D_z \gg L_z = 64$ in the optimum case which shows that these ellipsoids are approximately cylindrical with axis parallel to the z-axis. Adaptive search failed to converge to the global maximum finding a slightly higher volume fraction than optimal $\rho_s \approx 0.2$. Nelder-Mead, pattern search converged to the same optimum as PSO.

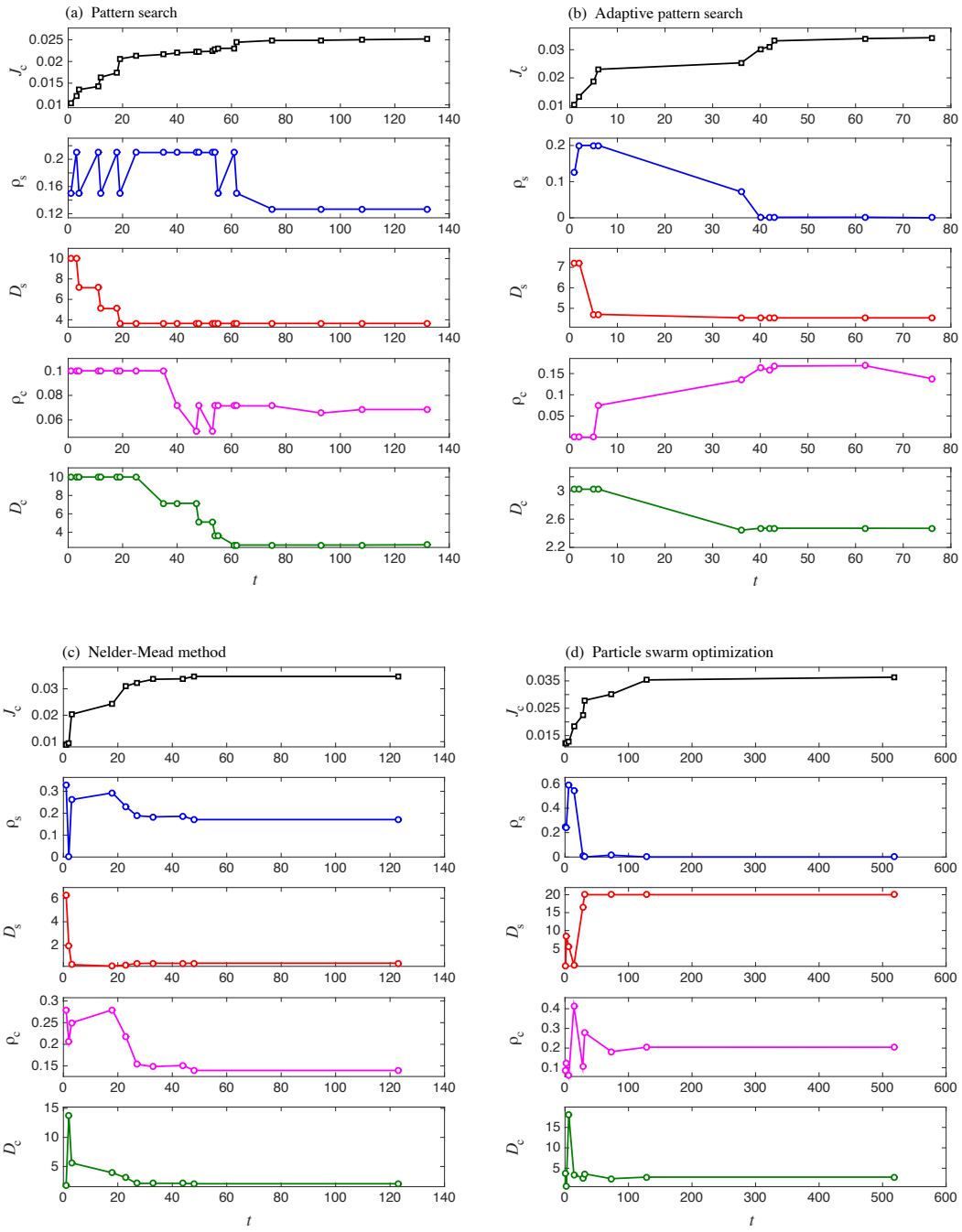

Figure 4.6. Optimization paths for the four-parameter optimization problem (spheres vs. cylinders) as a function of iteration number t, see Eq. (4.7c), using (a) pattern search, (b) adaptive pattern search, (c) Nelder-Mead method, and (d) particle swarm optimization. Except for pattern search which maintained a coexistence of spheres and cylinders, all other methods converge to only cylindrical defects. The fact that PSO also converges to this point and it has a higher J_c gives strong evidence to support that this is optimum.

sample already containing chemically grown nanorods [**68**]. In this case the parameter space will be defined by concentration ρ of irradiated defects and concentration γ of chemically-grown inclusions, $\mathbf{x} = (\rho, \gamma)$. Note, due to the discrete nature of the pinning centers the function $J_c(\mathbf{x})$ may be a noisy function in general.

To obtain the critical current $J_c(\mathbf{x})$, we solve the TDGL equation described in Sec. 4.4 in the domain of interest with the specified parameter set $\mathbf{x}$. Each evaluation of J_c is relatively expensive (typically, a few GPU-hours) and can be performed independently. In order to reduce noise in J_c, one can (i) average it over several realizations of random positions of inclusions and/or (ii) increase averaging time. Both techniques naturally increase the computation time of J_c. In experiment the parameters of the inclusions in a superconductor can only be controlled to within a certain precision, thus the robustness of the found solution is also important. The robust configuration should be insensitive to small perturbations in parameters $\mathbf{x}$ characterizing pinning landscape.

In this work we concentrate on existent numerical methods for the systematic optimization of the critical current in the superconductor. We consider the model geometry with a three-dimensional superconducting cube with dimensions $64 \times 64 \times 64$ in units of coherence length ξ with quasi-periodic boundary conditions. The external current J is applied perpendicular to the magnetic field B. To test the efficiency of the methods, we begin with a known result for spherical inclusion density and size [**92**]. The program requires us to specify number of inclusions N_s, N_e, N_c, not volume fraction, so we require a transform for each problem. The two main (2D) control parameters are volume fraction occupied by inclusions ρ_s and diameter D_s of each inclusion,

$$\mathbf{x} = (\rho_s, D_s), \qquad N_s = \text{round}\left(\frac{6L_xL_yL_z\rho_s}{\pi D_s^3}\right). \tag{4.7a}$$

This problem was tuned to a three-parameter (3D) optimization problem by assigning inclusions two different diameters in xy plane and z direction. We modified the relation for number of inclusions to account for the fact that $D_z \gg L_z$.

$$\mathbf{x} = (\rho_e, D_{xy}, D_z), \qquad N_e = \text{round}\left(\frac{4L_xL_yL_z\rho_e}{\pi\kappa D_{xy}^2\tilde{D}_z}\right). \tag{4.7b}$$

Where $\tilde{D}_z = \min(D_z, L_z)$ and $\kappa = 1 - \frac{\tilde{D}_z{}^2}{3D_z^2}$. The four-dimensional (4D) problem involves a competition between spherical and columnar inclusions. The control parameters are then $\rho_\mathrm{s}, D_\mathrm{s}$ for spheres and $\rho_\mathrm{c}, D_\mathrm{c}$ for cylinders,

$$\mathbf{x} = (\rho_\mathrm{s}, D_\mathrm{s}, \rho_\mathrm{c}, D_\mathrm{c}), \qquad N_c = \text{round}\left(\frac{4L_xL_y\rho_s}{\pi D_{xy}^2}\right), \tag{4.7c}$$

where N_s was defined in (4.7a).

4.6. Results

Figures 4.4, 4.5, and 4.6 all show the optimization path for a particular run of that optimization routine for the 2D [Eq. (4.7a)], 3D [Eq. (4.7b)], and 4D [Eq. (4.7c)] problems, respectively. The physical results are summarized in Table 4.6. In the 2D case for randomly placed spherical inclusions the optimal value is the same as in [**92**] for magnetic field $B = 0.1H_{c2}$. In the 3D case for ellipsoidal inclusions the optimal pinning landscape corresponds to the infinite size in z direction (larger then system size), i.e. to the columnar inclusion, and the optimal value of the critical current raises by $\sim 50\%$. The 4D case for a combination of the columnar and spherical defects ends up with columnar defects in z direction only. The diameter of the columnar defects in 3D and 4D cases is naturally the same.

d	$\mathbf{x} = \{\rho_\mathrm{s}$		$D\}$	J_c
2	0.22		3.5	0.0235
d	$\mathbf{x} = \{\rho$	D_{xy}	$D_z\}$	J_c
3	0.20	3.0	∞	0.035
d	$\mathbf{x} = \{\rho_\mathrm{s}$	D_s	ρ_c $D_\mathrm{c}\}$	J_c
4	0.00	—	0.20 3.0	0.035

Table 4.6. Optimal parameters of the pinning landscape for maximal critical current in the superconductor.

To obtain a function evaluation, that is a good estimate of the true critical current for randomly placed inclusions, we require a large number of realizations. The critical current from each realization is averaged to give us "objective function evaluation." In theory, we expect the current surface to be relatively smooth (i.e. in the case where we take a sufficiently large number of realizations). In practice, this is too computationally expensive, hence our function can be quite noisy. This noise is especially dangerous when the noise is of the order of the function value. This invariably leads to local methods failing to reach the optimal solution. However, global methods like PSO are much more resistant to the noise in the objective function.

Increasing the parameter space can only improve the function value and as expected, J_c increased with increasing parameter space dimension. PSO was able to improve J_c by $\sim 50\%$ from $d = 2$ to 4. Physically, the 4D optimization is a competition between spherical and cylindrical defects. Three configurations are possible: coexistence, all cylindrical or all spherical. The result shows an optimal configuration where spherical inclusions are gone and cylinders with an optimal density and diameter remain. That one species of inclusion should go to zero is not surprising. The magnetic field is aligned parallel to the z-axis and so the vortices can be well contained in cylindrical holes parallel to the z-axis. If however,

the magnetic field was rotated (vortices are rotated), this configuration would no longer be optimal and a co-existence of these two types of inclusions would become optimal.

Figures 4.4, 4.5, and 4.6 all show the optimization path for a particular run of that optimization routine for the 2D [Eq. (4.7a)], 3D [Eq. (4.7b)], and 4D [Eq. (4.7c)] problems, respectively. All local methods were comparable for the 2D problem, PSO took a large number of iterations, but looking at Fig. 4.4, we see the improvement is marginal. The difficultly is determining an appropriate exit criterion. The increased dimensionality leads to an increase in number of iterations, however it appears to scale linearly which is not terrible. PSO was insensitive to the dimensionality taking roughly the same number of iterations and asymptoting to the optimal J_c after $\sim$ 100–200 iterations. We note that only a single sample optimization run was used for PSO and 2–3 were used for the local methods (if they did not converge to the best solution the first time). Therefore, though the number of iterations can be dramatically less, multiple runs can make the efficiency comparable.

An additional observation of the surface J_c can be made by noting that the number of evaluations required for adaptive pattern search and pattern search to converge were nearly the same. We can conclude that the current surface is topologically different from the Rosenbrock function. Indeed, if the maximum was in a Rosenbrock-type function, coordinate descent would take orders of magnitude longer (as was observed from testing the benchmark functions). We also observed that all methods converge to the same maximum ($\pm 1\%$) in 2D, but in 3D or 4D, the local methods did not always find the global maximum or perform as well as the global method. This indicates that additional parameters can, perhaps create local maxima, which can create difficulties for the local methods. This can be mitigated by taking more realizations, which should smooth out the error from random placement potentially being poor, but we have no guarantee that the multi-maxima are caused primarily by this

mechanism and not some underlying physical principle. Ultimately, this leads to a balance between number of realizations and choice of method.

The main benefit to using a global method such as PSO, is that it consistently finds the better solution than the local methods. In higher dimensional spaces $d \gtrsim 4$, taking a larger swarm size S becomes necessary to ensure convergence. The local methods however, converge faster, where strictly speaking there is no such guarantee that the optimal value returned from PSO is actually an optimum at all. Additionally, local methods have obvious choices for exit criterion, unlike PSO, which can often take additional evaluations 10^2–10^3 for a marginal gain in the objective function ($< 1\%$).

We compared the relative error of PSO with a single run of adaptive pattern search in the four dimensional case and found that the J_c of PSO was $< 2\%$ higher than local methods (when they converged to the correct value). Furthermore, we found that the parameters obtained from local methods varied in relative error when compared to PSO, ranging from $< 5\%$ for the 2D problem to as much as 25% for the 4D problem. This suggests a flatter global maximum as the dimensionality increased for this particular problem.

4.7. Conclusions

We have tested various methods and determined that PSO and adaptive pattern search performed the best on the benchmark functions as well as in the physical optimization problem presented. PSO in particular does a relatively good job at handling the noisy surface of J_c, but suffers from a clear exit criterion which leads to additional (and potentially costly extra function evaluations). On the other side, adaptive pattern search can get caught at a local maximum, created physically or through the noise, however the number of evaluations are often much less (on the order of 7–10 times). The multi-level local method as mentioned

in the methods section could be introduced to mitigate this, and this would lead to a number of function evaluations similar to, or perhaps even greater than PSO if the number of local maxima is very large. We would then be assured we have converged to local optimum and more local searches increase our probability that we have found the global, PSO gives no such guarantee, but is a simple method which doesn't get caught easily in a local maximum.

CHAPTER 5

Analytical results of Weighted Jacobi

5.1. Introduction

As was mentioned in chapter 1, TDGL was solved and implemented on a GPU architecture, which leads naturally to the use of parallelizable methods. Jacobi is an obvious candidate, it is easy to implement and its convergence properties are well known. Jacobi's Method for solving the diagonally dominant linear system $\mathbf{Ax} = \mathbf{b}$ was first suggested by Jacobi in 1834 [**93**]. The process was simple, and involved separating the matrix $\mathbf{A} = \mathbf{M} - \mathbf{E}$ where $\mathbf{M} = \text{diag}(\mathbf{A})$ and $\mathbf{E}$ is the remaining off-diagonal elements. Approximations to the solution $\mathbf{x}$ are given by $\mathbf{x}^{(i)}$. These are updated iteratively using the following equation

$$\mathbf{x}^{(n+1)} = (\mathbf{I} - \mathbf{M}^{-1}\mathbf{A})\mathbf{x}^{(n)} + \mathbf{M}^{-1}\mathbf{b}. \tag{5.1}$$

Before proceeding, we comment on the distinction between scalars, vectors and matrices by using the following representation: scalars are denoted by lower-case letters $(a, b, \dots)$, vectors are written as boldface lower-case $(\mathbf{x}, \mathbf{y}, \dots)$ and matrices correspond to boldface capitals $(\mathbf{A}, \mathbf{B}, \dots)$. Defining $\mathbf{G} = \mathbf{I} - \mathbf{M}^{-1}\mathbf{A}$, it is clear that a sufficient condition for convergence of this method is for the spectral radius of $\mathbf{G}$ to satisfy $|\rho(\mathbf{G})| < 1$. In practice, this was quite restrictive as it required $0 < \rho(\mathbf{M}^{-1}\mathbf{A}) < 2$ which constricts the class of linear systems guaranteed to converge with this method. This issue was eventually solved by introducing a damping parameter ω which can be controlled for improved convergence [**94**]. With this,

the modified iterative scheme becomes

$$\mathbf{x}^{(n+1)} = (\mathbf{I} - \omega \mathbf{M}^{-1}\mathbf{A})\mathbf{x}^{(n)} + \omega \mathbf{M}^{-1}\mathbf{b}. \tag{5.2}$$

Defining $\mathbf{G}_\omega = \mathbf{I} - \omega \mathbf{M}^{-1}\mathbf{A}$, we can easily show that a sufficient condition for convergence of this method is given by the requirement $0 < \omega < 2/\rho(\mathbf{M}^{-1}\mathbf{A})$. Over time, (weighted) Jacobi's method has become obsolete by other more efficient iterative methods such as successive over-relxation (SOR) and conjugate gradient (CG), which offer sufficiently quicker convergence properties [**95**, **96**]. However, Jacobi's method has recently been improved by following a schedule of over and under relaxations updates [**97**]. In the last few decades, the increase of processing power utilizing parallel computing has become an important part of high-performance simulations [**98**]. With this, comes the need for easily parallelizable methods, which leads us back to Jacobi's Method.

In practice, the optimal weight parameter is strongly problem-dependent and has been computed through trial and error and more recently through auto-tuning techniques [**96**,**99**]. We will show that an optimal choice of this parameter ω is in fact more related to the choice of coordinate system and grid size.

It is of course possible to converge in under n iterations where n is the dimension of the matrix $\mathbf{A}$ if one knows *a priori* the distribution of eigenvalues of the matrix $\mathbf{M}^{-1}\mathbf{A}$. However, from a numerical standpoint this is highly impractical. Historically, the problem of finding the optimal weight parameter has been motivated in the following way. The amplification factor of the iteration matrix $\mathbf{G}_\omega$ is given by $1 - \omega\lambda_{\mathbf{M}^{-1}\mathbf{A}}$ where $\lambda_{\mathbf{M}^{-1}\mathbf{A}}$ is an eigenvalue of the matrix $\mathbf{M}^{-1}\mathbf{A}$. This leads to the following optimization problem for the weight parameter

$$\omega_{\text{opt}} = \min_{\omega} \max_{\lambda} |1 - \omega\lambda|. \tag{5.3}$$

In the case where all the eigenvalues are real, we note that the function in (5.3) is minimized and symmetric in λ-space at $\lambda_c = 1/\omega$. It is clear that the minimum should be located at the midpoint of the extreme eigenvalues which leads to the well known result

$$\omega_{\text{opt}} = \frac{2}{\lambda_{min} + \lambda_{max}}. \tag{5.4}$$

Therefore, one only needs the extreme eigenvalues to determine a "good" weight parameter. In this paper, we extend the theory regarding this ω_{opt} by showing under very general conditions, we can actually compute the value in (5.4) for a class of matrices without ever calculating an eigenvalue. These matrices are often sparse and found most commonly in solving physical problems involving the Laplacian operator.

This paper is structured as follows: First, the structure of typical 1-D problems (which typically leads to tridiagonal matrix systems) are described in terms of the Jacobi matrix and introduced in section 5.2. In section 5.3, the result is generalized by first adding an additional (super) diagonal with nonzero elements, then we consider the symmetric case. In section 5.4 we discuss approximations to ω_{opt} and analysis of convergence. In section 5.5, we compare the analytical results with numerical simulations and analyze ways to exploit the derived properties to speed up Jacobi for large sparse matrices. Section 5.6 gives closing remarks, and discusses issues and possible remedies.

5.2. Optimal Parameter for a Tridiagonal Matrix

Consider the one dimensional heat equation

$$u_t - \nabla^2 u = f, \quad x \in (0, L) \tag{5.5}$$

$$u|_{x=0,L} = 0.$$

Time dependent problems involving the Laplacian are typical and widespread in physical problems (e.g. fluid mechanics, electrodynamics, wave equations, superconductors, etc.). Though being 1-D, (5.5) can still be insightful in analyzing the behavior of Jacobi methods.

In practice, these problems are often solved using sequential methods such as Thomas' algorithm [**100**]. However, this simple case allows us to generalize to more complicated and higher dimensional problems where iterative methods become relevant and sequential processes become detrimental and so we begin with the tridiagonal case first.

5.2.1. Properties of a Jacobi Iteration Matrix

We begin this section by stating our first result –

Theorem 5.2.1. Let $\mathbf{A} \in \mathbb{R}^{n\times n}$ be a diagonally dominant tridiagonal matrix. Then $\omega_{opt} = 1$.

The proof of theorem 5.2.1 is subsequently given by a series of lemmas.

Lemma 5.2.1. Define $\mathbf{B} = \mathbf{M}^{-1}\mathbf{A} \in \mathbb{R}^{n\times n}$ with eigenvalues $\lambda_j \in \mathbb{C}$. Then

$$\sum_{j=1}^{n} \lambda_j = n \tag{5.6}$$

Proof. This follows immediately by noting that the trace of a matrix is the sum of its eigenvalues and $b_{jj} = 1$ by construction. □

Lemma 5.2.2. If additionally, **B** is diagonally dominant, then

$$|\lambda_j - 1| \leq 1 \tag{5.7}$$

Proof. By Gershgorin's circle theorem, we know that $|\lambda_j - 1| \leq \sum_{k \neq j} |b_{jk}|$. Using the fact that $1 \geq \sum_{k \neq j} |b_{jk}|$ completes the lemma. □

Lemma 5.2.3. $\lambda_{min} \leq 1$ and $\lambda_{max} \geq 1$.

Proof. This follows from Lemma 5.2.1 by noting

$$\bar{\lambda} := \frac{1}{n} \sum_{j=1}^{n} \lambda_j = 1$$

which indicates that the mean of the eigenvalues is 1 (hence the smallest one could not lie above nor the largest below). □

Remark 1. It should be noted here that if $\lambda_j \in \mathbb{R}$ for all j, then we can immediately see by noting $\lambda_{\max} \leq 2$ that $\omega_{opt} \geq 2/3$ is a lower bound for diagonally dominant linear systems.

Lemma 5.2.4. Let **B** be a tridiagonal matrix of the form

$$\mathbf{B}_n = \begin{bmatrix} 1 & \alpha_1 & 0 & \dots & 0 \\ \beta_1 & 1 & \alpha_2 & 0 & 0 \\ 0 & \ddots & \ddots & \ddots & 0 \\ \vdots & & \ddots & \ddots & \alpha_{n-1} \\ 0 & \dots & 0 & \beta_{n-1} & 1 \end{bmatrix} \tag{5.8}$$

Then the characteristic polynomial $F_n(\nu)$ of $\mathbf{B}$ where $\nu \equiv 1 - \lambda$ and λ is an eigenvalue of $\mathbf{B}$ is given by the recurrence relation:

$$F_n(\nu) = \nu F_{n-1}(\nu) - \alpha_{n-1}\beta_{n-1}F_{n-2}(\nu), \qquad F_0 = 1,\ F_{-1} = 0 \tag{5.9}$$

The deg $F_n(\nu) = n$ and $F_{2k}(\nu)$ is even, while $F_{2k+1}(\nu)$ is odd.

Proof. The derivation of (5.9) is straightforward. The degree of F_n follows easily by induction. We show that $F_{2k}(\nu)$ is an even function. First note that $F_0 = 1$ and $F_1 = \nu$ (the base case). Now suppose this relation holds for $n < 2k$. Then

$$\begin{aligned} F_{2k}(-\nu) &= (-\nu)F_{2k-1}(-\nu) - \alpha_{2k-1}\beta_{2k-1}F_{2k-2}(-\nu) \\ &= (-\nu)[-F_{2k-1}(\nu)] - \alpha_{2k-1}\beta_{2k-1}F_{2k-2}(\nu) \\ &= \nu F_{2k-1}(\nu) - \alpha_{2k-1}\beta_{2k-1}F_{2k-2}(\nu) \\ &= F_{2k}(\nu) \end{aligned}$$

Hence F_{2k} is even, the odd case follows analogously. □

Lemma 5.2.5. If $F_n(\nu) = 0$, then $F_n(-\nu) = 0$.

Proof. Since F_n is either even or odd depending on the integer n, we know that $F_n(-\nu) = (-1)^n F_n(\nu)$. Plugging in the assumption we immediately see

$$F_n(-\nu) = (-1)^n F_n(\nu) = 0$$

which proves the result. □

Lemma 5.2.6. Let $f(\nu)$ be the characteristic polynomial of the $\mathbf{B}$. If $\lambda_j \in \mathbb{R}$ for all j, then $\nu_{max} + \nu_{min} = 0$.

Proof. Define the largest zero in magnitude that satisfies the function $f(\nu) = 0$ by ν_{max}. Without loss of generality suppose that $\nu_{max} > 0$. Then by Lemma 5.2.5, we know that $-\nu_{max}$ is also an eigenvalue. Then it follows that $\nu_{min} = -\nu_{max}$. To see this, suppose that $\nu_{min} < -\nu_{max}$. Then $|\nu_{min}| > |\nu_{max}|$, but we said that ν_{max} was the largest in magnitude, which is a contradiction. We note here that this implies that $\nu_{min} + \nu_{max} = 0$. □

The proof of Theorem (5.2.1) now follows easily using (5.4) and lemma 5.2.6. It is easy to see that $\lambda_{max} = 1 - \nu_{min}$ and $\lambda_{min} = 1 - \nu_{max}$. Hence

$$\lambda_{min} + \lambda_{max} = 2 - (\nu_{min} + \nu_{max}) = 2.$$

We immediately see from (5.4) that $\omega_{opt} = 1$.

Corollary 5.2.1. If A is Hermitian, then we can always transform the operator to a form where $\omega_{opt} = 1$.

Remark 2. Though it may be impractical to transform the operator (i.e. by Householder's algorithm), the corollary is nevertheless insightful. It is well known that a unitary transformation is equivalent to a change of basis, which in a physical setting can be thought of as a coordinate system transformation. For example, we can construct a symmetric matrix $\mathbf{A}$ where the optimal parameter $\omega_A < 1$. However, we can reduce it to a tridiagonal matrix $\mathbf{B}$ by the above corollary implying that $\omega_B = 1$ which supports the notion that ω_{opt} is coordinate system dependent.

For related properties of similar matrices, see [**101**].

5.2.2. Properties of Toeplitz F_n

If we assume in (5.8) that the matrix is Toeplitz (i.e. that $\alpha_i = \alpha$ and $\beta_i = \beta$), then the following is true of F_n:

$$F_n(\nu) = \begin{cases} \frac{(\alpha\beta)^{n/2}\sin\left[(n+1)\arccos\left(\frac{\nu}{2\sqrt{\alpha\beta}}\right)\right]}{\sin\left[\arccos\left(\frac{\nu}{2\sqrt{\alpha\beta}}\right)\right]}, & |\nu| < 2\sqrt{\alpha\beta} \\ (\alpha\beta)^{n/2}(n+1), & \nu = \pm 2\sqrt{\alpha\beta} \end{cases} \tag{5.10}$$

Thus the solution to $F_n(\nu) = 0$ is given by

$$\nu_m = 2\sqrt{\alpha\beta}\cos\left(\frac{m\pi}{n+1}\right),\ m = 1, 2, \ldots, n \tag{5.11}$$

In general however, the distribution of eigenvalues does not have a closed form solution. Despite this, we will still be able to obtain useful bounds on ω_{opt} (see section 3.3).

5.3. Optimal parameter for more general matrices

The key to proving Theorem 5.2.1 relied on the symmetry of the characteristic polynomial. We must extend the result and exploit this symmetry to obtain conditions where $\omega_{opt} = 1$ for more general problems. We now introduce some notation. Let d be the distance from the main diagonal where $d = \pm 1$ corresponds to the super/sub diagonals respectively of a matrix $\mathbf{A}$. For the remainder of the paper, we will assume the matrix is Toeplitz as this greatly simplifies the algebra and notation, however the results are still valid in the general case.

5.3.1. Tridiagonal Matrix with an additional non-zero diagonal

For simplicity, we begin the analysis of more general matrices by considering just one additional nonzero diagonal d with $|d| \geq 2$. In the following theorem, we consider the matrix $\mathbf{B}_{n,d}$ and $\mathbf{C}_{n,d} := \mathbf{B}_{n,d} - (1-\nu)\mathbf{I}$

$$b_{ij} = \begin{cases} 1 & \text{if } i = j \\ \alpha & \text{if } |i-j| = 1\,, \\ \beta & \text{if } j - i = d. \end{cases} \qquad c_{ij} = \begin{cases} \nu & \text{if } i = j \\ \alpha & \text{if } |i-j| = 1 \\ \beta & \text{if } j - i = d. \end{cases} \tag{5.12}$$

This allows us to obtain a recurrence relation for the characteristic polynomial in closed form.

Theorem 5.3.1. Let $F_{n,d}(\nu)$ be the characteristic polynomial corresponding to the matrix $\mathbf{B}_{n,d}$. Then the following relation holds.

$$F_{n,d}(\nu) = \nu F_{n-1,d}(\nu) - \alpha^2 F_{n-2,d}(\nu) + (-1)^d \beta \alpha^{|d|} F_{n-(d+1),d}(\nu) \tag{5.13}$$

where $F_{n,d}$ is defined similarly to F_n in Lemma 5.2.4. In addition, the polynomial is symmetric only if $|d| = 2k+1$ where $k \geq 1$, which implies $\omega_{opt} = 1$ (by Lemma 5.2.6).

Proof. The characteristic polynomial $F_{n,d}(\nu)$ is given by

$$F_{n,d}(\nu) = |\mathbf{C}_{n,d}|. \tag{5.14}$$

Expanding the determinant over the first row we define $\mathbf{C}_{n,d}^{(i,j)}$ to be the minor of $\mathbf{C}_{n,d}$ with row i and column j removed. Hence we immediately see that $|\mathbf{C}_{n,d}^{(1,1)}| = F_{n-1,d}(\nu)$. Next it is also clear that $|\mathbf{C}_{n,d}^{(1,2)}| = \alpha F_{n-2,d}(\nu)$. To calculate $|\mathbf{C}_{n,d}^{(1,d-1)}|$, we use the fact that this creates

a block matrix of the following form

$$|\mathbf{C}_{n,d}^{(1,d-1)}| = \begin{vmatrix} \mathbf{E} & \mathbf{u} \\ \mathbf{0} & F_{n-(d+1),d}(\nu) \end{vmatrix} = |\mathbf{E}| F_{n-(d+1),d}(\nu),$$

where

$$E_{ij} = \begin{cases} \alpha & \text{if } i = j, \text{ or } i = j-2 \\ \nu & \text{if } i = j-1 \\ 0 & \text{otherwise} \end{cases}$$

Hence $\left|\mathbf{C}_{n,d}^{(1,d-1)}\right| = \beta\alpha^d F_{n-(d+1),d}(\nu)$. Combining these gives (5.13). To prove the symmetry property, we use (5.14) and replace $\nu \to -\nu$. Factoring (-1) out of each column we have

$$F_{n,d}(-\nu) = (-1)^n \begin{vmatrix} \nu & -\alpha & 0 & \dots & 0 & -\beta & 0 & \dots & \dots & 0 \\ -\alpha & \nu & -\alpha & 0 & \dots & 0 & -\beta & 0 & & \vdots \\ 0 & -\alpha & \nu & \alpha & 0 & \dots & 0 & \ddots & \ddots & \vdots \\ \vdots & \ddots & \ddots & \ddots & \ddots & \ddots & & \ddots & \ddots & 0 \\ \vdots & & \ddots & \ddots & \ddots & \ddots & \ddots & & 0 & -\beta \\ \vdots & & & \ddots & \ddots & \ddots & \ddots & \ddots & & 0 \\ \vdots & & & & \ddots & \ddots & \ddots & \ddots & \ddots & \vdots \\ \vdots & & & & & \ddots & \ddots & \ddots & \ddots & 0 \\ \vdots & & & & & & \ddots & \ddots & \ddots & -\alpha \\ 0 & \dots & \dots & \dots & \dots & \dots & \dots & 0 & -\alpha & \nu \end{vmatrix}.$$

We now obtain

$$F_{n,d}(-\nu) = (-1)^n [\nu F_{n-1,d}(\nu) - \alpha^2 F_{n-2,d}(\nu) - \beta\alpha^d F_{n-(d+1),d}(\nu)]$$

Multiplying (5.14) by $(-1)^n$ and subtracting this from the previous equation we obtain

$$(-1)^n F_{n,d}(\nu) - F_{n,d}(-\nu) = [(-1)^{n+d} + (-1)^n]\beta\alpha^d F_{n-(d+1),d}(\nu)$$

This is 0 only if $(n+d) - n = 2k+1$, or $d = 2k+1$. □

Remark 3. The result of Theorem 5.3.1 holds even if the matrix is not Toeplitz. In addition, recursion relation (5.13) could easily be extended to multiple diagonals $d_1, \ldots d_k$ provided that all diagonals lie either above or below the main diagonal (i.e. $d_i \geq 2$ for all i or $d_i \leq -2$ for all i).

We would like to analyze the asymptotic behavior of large matrices with the property – $n, d \to \infty$. The following theorem shows that $\omega_{\text{opt}} \to 1$ in the limit as $n, d \to \infty$.

Theorem 5.3.2. If $n, d \to \infty$, then $\omega_{\text{opt}} \to 1$.

Proof. Since we have shown that $\omega_{\text{opt}} = 1$ for all $d = 2k+1$, we consider only the case $d = 2k$. We claim that for $k \to \infty$, the last term in (5.13) decays faster than the others and so we approach a symmetric polynomial asymptotically which in the limit will imply that $\omega_{\text{opt}} \to 1$. Consider the Ansatz $F_{n,d}(\nu) := x^n$. We define

$$f(x) := x^{2k+1} - \nu x^{2k} + \alpha^2 x^{2k-1} - \beta\alpha^{2k},$$

and define the roots $x_1, \ldots x_{2k+1}$. We will show that $\exists\, |x_i| > \alpha$ for $k \to \infty$. The derivative is $f'(x) = x^{2k-1}[(2k+1)x^2 - 2k\nu x + \alpha^2(2k-1)]$. Excluding the $2k-1$ trivial zeros, we see that as $k \to \infty$, the two other roots $|x_1'| \geq |x_2'|$ satisfy $x_1' x_2' = \alpha^2 > 0$ and $x_1' + x_2' = \nu$. We first analyze the case $|\nu| > 2|\alpha|$. It is clear that $|x_1'| \geq \alpha$ since otherwise the product would not equal α^2. To see that $x_1' \neq \alpha$, we need only note then that $x_1' + x_2' = 2\alpha = \nu$

which contradicts $|\nu| > 2|\alpha|$. Hence $|x_1'| > \alpha$. Now, by the Gauss-Lucas theorem (GLT), the zeros of f' must be contained in the convex hull of f and so $\exists\, |x_i| > \alpha$. Suppose now that $|\nu| \leq 2|\alpha|$, then $|x_1'| = |x_2'| = |\alpha|$. Let $x_1' = |\alpha|e^{i\phi}$ and $x_2' = |\alpha|e^{-i\phi}$. Plugging in x_1' into f we see that for $f(x_1') = 0$ we require

$$2|\alpha| \cos\phi - (-1)^n \beta = \nu,$$

where n is an integer. Using the definition of $\cos\phi = \nu/2|\alpha|$ we see that $\beta = 0$ is the only solution and if this was the case, we would be in the tridiagonal case, which we have already showed satisfies $\omega_{\text{opt}} = 1$. Hence x_1' is not a zero of f (and similarly for x_2'). By GLT, we can conclude that f must have a zero $|x_i| > \alpha$, for if not, (i.e. $|x_i| \leq \alpha$ for all i), then $|x_1'|$ would not be contained in the convex hull which is a contradiction. Therefore, we have shown that $\exists\, |x_i| > |\alpha|$ where $f(x_i) = 0$. Now for sufficiently large n, and let $|x_1|$ be the largest zero of f, we see that $F_{n,d}(\nu) \to c x_1^n$. Looking at (5.13), we see that for large n,

$$F_{n,2k}(\nu) \sim x_1^{n-1} \left[\nu - \frac{\alpha^2}{x_1} + \beta \left(\frac{\alpha}{x_1} \right)^{2k} \right].$$

Hence as $k \to \infty$ the last term goes to zero and so $\omega_{\text{opt}} \to 1$. □

5.3.2. Optimal Parameter for a Symmetric Toeplitz Matrix with two additional non-zero diagonals

In section 5.2, we used the 1D heat equation to motivate the initial analysis. Now we consider a higher dimensional problem. These involve a large class of problems which gives a tridiagonal, pentadiagonal or in general, a $(2n+1)$-diagonal form where n is the physical dimension. In this section we show that the properties found in the single off-diagonal case

carry over to the symmetric case and that when the elements are small in magnitude we have obtain a decent approximation to ω_{opt} when $d = 2k$.

We will assume a matrix $\mathbf{B}_{n,d}$ of the form:

$$b_{ij} = \begin{cases} 1 & \text{if } i = j \\ \alpha & \text{if } |i-j| = 1 \\ \beta & \text{if } |i-j| = d \end{cases} \tag{5.15}$$

Theorem 5.3.3. Let the matrix $\mathbf{B}_{n,d}$ be of the form (5.15) with $d = 2k+1$ then $\omega_{opt} = 1$.

Proof. Unlike the previous case, it is difficult to derive a general recurrence relation for the characteristic polynomial. Instead we utilize a different technique to prove that $\omega_{opt} = 1$ when $d = 2k + 1$ ($d > 0$ can now be assumed without loss of generality). Let $F_{n,d}(\nu) = |\mathbf{B}_{n,d} - (1-\nu)\mathbf{I}| := |\mathbf{C}_{n,d}(\nu)|$ where $\mathbf{C}_{n,d}(\nu)$ has the form

$$c_{ij} = \begin{cases} \nu & \text{if } i = j \\ \alpha & \text{if } |i-j| = 1 \\ \beta & \text{if } |i-j| = d \end{cases} \tag{5.16}$$

Consider $(-1)^n F_{n,d}(-\nu) = (-1)^n |\mathbf{C}_{n,d}(-\nu)| = |-\mathbf{C}_{n,d}(-\nu)|$. Define the map

$$[T_K(\mathbf{C})]_{ij} = (1 - 2\delta_{iK})(1 - 2\delta_{jK})c_{ij},$$

where δ_{ij} is the Kronecker delta. It clear then that this map is invariant with respect to the determinant, that is, $|T_K(\mathbf{C})| = |\mathbf{C}|$. Then we may write

$$| - \mathbf{C}_{n,d}(-\nu)| = \left| \prod_{K=1}^{\lfloor \frac{n}{2} \rfloor} T_{2K-1}[-\mathbf{C}_{n,d}(-\nu)] \right| := \left| T[-\mathbf{C}_{n,d}(-\nu)] \right|.$$

It can be shown that $[T(\mathbf{C})]_{ij} = (-1)^{\mathrm{mod}(i+j,2)} c_{ij}$ by employing the property that for $K_1 \neq K_2$ we have $T_{K_1} T_{K_2} = [1 - 2(\delta_{iK_1} + \delta_{iK_2})][1 - 2(\delta_{jK_1} + \delta_{jK_2})]$ (and then using induction to show it is true for n transformations). Thus

$$[T(-\mathbf{C}_{n,d}(-\nu))]_{ij} = \begin{cases} \nu & \text{if } i = j \\ \alpha & \text{if } |i-j| = 1 \\ \beta(-1)^{\mathrm{mod}(d+1,2)} & \text{if } |i-j| = d \end{cases},$$

so if $\mathrm{mod}(d-1, 2) = 0$, or if $d = 2k+1$, then we have

$$(-1)^n F_{n,d}(-\nu) = |T[-\mathbf{C}_{n,d}(-\nu)]| = |\mathbf{C}_{n,d}(\nu)| = F_{n,d}(\nu).$$

This implies that the characteristic polynomial is symmetric and by lemma 5.2.6 we have $\omega_{\mathrm{opt}} = 1$. □

Remark 4. Similar to Theorem 5.3.1, the result of Theorem 5.3.3 holds even if the matrix is not Toeplitz or symmetric. The only requirement is that the non-zero elements lie on diagonals $d_i = 2k+1$ for any $k \in \mathbb{Z}$.

5.4. Asymptotic approximations

5.4.1. Approximation of $\omega_{\mathbf{opt}}$

There is a well known result for approximating eigenvalues of a given system. Suppose $\mathbf{A}\mathbf{y}_\mathbf{A} = \lambda_\mathbf{A}\mathbf{y}_\mathbf{A}$ are known eigenvalues and eigenvectors (normalized). Consider the perturbed system $\mathbf{B}\mathbf{y}_\mathbf{B} = \lambda_\mathbf{B}\mathbf{y}_\mathbf{B}$ where $\mathbf{B} = \mathbf{A} + \beta\mathbf{S}$, then the update for the eigenvalues is given by

$$\lambda_\mathbf{B} = \lambda_\mathbf{A} + (\mathbf{y}_\mathbf{A}^T\mathbf{S}\mathbf{y}_\mathbf{A})\beta + \mathcal{O}(\beta^2).$$

The difficultly with this method, is that it requires knowledge of the eigenvectors of the unperturbed system $\mathbf{A}$. In our case the unperturbed system is the tridiagonal Toeplitz system from section 2. We gave the closed form for the eigenvalues, but we did not give the closed form for the eigenvectors. It can be shown that an eigenpair $(\lambda_m, \mathbf{y}_m)$ of $\mathbf{A}$ has the form:

$$\lambda_m = 1 + 2\alpha\cos\left(\frac{m\pi}{n+1}\right), \qquad y_{m,j} = \sqrt{\frac{2}{n+1}}\sin\left(\frac{jm\pi}{n+1}\right),\ j = 1, 2, \ldots, n.$$

To calculate the update we assume $\mathbf{S} = \delta_{i,i-d} + \delta_{i,i+d}$ where $\delta_{i,j}$ is the Kronecker delta. This implies that

$$\mathbf{y}_m^T\mathbf{S}\mathbf{y}_m = 2\sum_{j=1}^{n-d} y_{m,j}y_{m,j+d}.$$

Inserting the definition for $y_{m,j}$ we have an update for the new eigenvalue at first order given by

$$\lambda_{\mathbf{B},m} = 1 + 2\alpha\cos\left(\frac{m\pi}{n+1}\right) + \frac{2\beta}{n+1}\left\{(n-d)\cos\left(\frac{md\pi}{n+1}\right) + \frac{\sin\left[\frac{m\pi(d+1)}{n+1}\right]}{\sin\left(\frac{m\pi}{n+1}\right)}\right\}. \tag{5.17}$$

For this paper, we are primarily interested in the largest and smallest eigenvalues. First, we show that the largest eigenvalue occurs at $m = 1$. Consider the right-most term in (5.17). Of course, we are technically only interested in $m = 1, 2, \ldots, n$, but for now we don't make this assumption. For brevity, we define the simpler notation $x = m\pi/(n+1)$ and $k = d+1$ with

$$h(x;k) \equiv \frac{\sin(kx)}{\sin x},$$

where $x \in \left(\frac{\pi}{n+1}, \frac{n\pi}{n+1}\right) \equiv I$. We show that $|h(x;k)| < k$ by induction on k. Consider $k = 2$, then

$$|h(x;2)| = \left|\frac{\sin 2x}{\sin x}\right| = 2|\cos x| < 2.$$

Assume now that it holds for the kth case. Then

$$|h(x;k+1)| = \left|\frac{\sin[(k+1)x]}{\sin x}\right| = \left|\frac{\sin(kx)\cos x}{\sin x} + \cos kx\right| \leq |h(x;k)||\cos x| + |\cos kx| < k+1.$$

Note that cancellation of the terms is valid provided that $\sin x \neq 0$, which is true in the interval given. We can also rewrite the second term in a more useful form and then evaluate the terms of (5.17) individually by defining

$$f(x) = 1 + 2\alpha\cos x \tag{5.18a}$$

$$g(x) = \frac{2\beta}{n+1}\left[(n-d+1)\cos(dx) + \sin(dx)\cot x\right]. \tag{5.18b}$$

We clearly see that f is monotonic for $x \in I$ (decreasing or increasing if α is positive or negative, respectively). The substitution $x \to \pi - x$ yields the relation $g(\pi - x) = (-1)^d g(x)$. Suppose that $\alpha > 0$ and $d = 2k$. Consider $x \in [0, \pi/2]$, then

$$f(x) + g(x) = f(x) + g(\pi - x) > f(\pi - x) + g(\pi - x),$$

which implies that the maximum of the function has to be in $[0, \pi/2]$ (and conversely that the minimum will be in $[\pi/2, \pi]$). We note that for $d \gg 1$, there is a rapidly oscillating function coupled with a slowly varying function. The extremum are then governed by the rapidly oscillating functions. The maxima $x_1 < x_2 < \cdots < x_l$ then occur with period $p \approx 2\pi/d$. Suppose that $\cos(dx_k) = \gamma$ and then $\sin(dx_k) = \pm\sqrt{1-\gamma^2}$. It is clear for a maximum that $g(x) > 0$ and so if $\beta > 0$ we would require that $\cos(dx_k) > 0$ and $\sin(dx_k) > 0$. If instead, $\beta < 0$, then we require $\cos(dx_k) < 0$ and $\sin(dx_k) < 0$. We can write this compactly using

$$g(x_k) = \frac{2|\beta|}{n+1}\left[(n-d+1)\gamma + \sqrt{1-\gamma^2}\cot x_k\right]. \tag{5.19}$$

$\cot x$ is decreasing and so $g(x_k) \geq g(x_{k+1})$. Since f is decreasing it follows that the maxima are all decreasing. The minima are treated in a similar way. Suppose $y_1 < y_2 < \cdots < y_l$ are the minima occurring with period $p \approx 2\pi/d$. We now want $g(x) < 0$, this amounts to a minus sign in (5.19). We obtain that $g(y_k) \leq g(y_{k+1})$. Again since f is decreasing it follows that the minima are also decreasing. This implies that the extremum are ordered and we can conclude that the global maximum occurs near $x = 0$ and is the first maxima and the global minimum occurs near $x = \pi$ and is the last minima. The case when $\alpha < 0$ is analogous, with maxima and minima reversed.

Converting back to original notation, we can now find an envelope. We can also conclude from this analysis that $g(x_k)$ extremum is roughly when $\gamma = 1$ (since equality only holds in this case). This allows us to approximate the extremum of this function

$$\tilde{E}(m) = 1 + 2\alpha\cos\left(\frac{m\pi}{n+1}\right) \pm \frac{2\beta(n-d+1)}{n+1}. \tag{5.20}$$

An envelope for $\lambda_{\mathbf{B},m}$ is given by

$$E(m) = 1 + 2\alpha \cos\left(\frac{m\pi}{n+1}\right) \pm 2\beta. \tag{5.21}$$

Using the envelope (5.21) or the approximation for extremum (5.20), we obtain a first order bound of ω_{opt} given by

$$\frac{1}{1+\kappa|\beta|} \leq \omega_{\text{opt}} \leq \min\left(\frac{2}{1+2|\alpha|+2\kappa|\beta|}, \frac{1}{1-\kappa|\beta|}\right), \tag{5.22}$$

where $\kappa = 1$ if we use (5.21) and $\kappa = \left(\frac{n-d+1}{n+1}\right)$ with (5.20).

Furthermore, we can approximate ω_{opt} using the above properties and noting that

$$\begin{aligned}
\max(\lambda_{\mathbf{B},m}) = \max\Bigg\{ & 1 + 2|\alpha| \cos\left(\frac{\pi}{n+1}\right) + \\
& \frac{2\beta}{n+1}\left[(n-d+1)\cos\left(\frac{d\pi}{n+1}\right) + \sin\left(\frac{d\pi}{n+1}\right)\cot\left(\frac{\pi}{n+1}\right)\right], \qquad (5.23a) \\
& 1 + 2|\alpha| \cos\left[\frac{[1+H(\beta)]\pi}{d}\right] + \frac{2|\beta|(n-d+1)}{n+1}\Bigg\} \qquad (5.23b)
\end{aligned}$$

$$\begin{aligned}
\min(\lambda_{\mathbf{B},m}) = \min\Bigg\{ & 1 - 2|\alpha| \cos\left(\frac{\pi}{n+1}\right) + \\
& \frac{2\beta}{n+1}\left[(n-d+1)\cos\left(\frac{d\pi}{n+1}\right) + \sin\left(\frac{d\pi}{n+1}\right)\cot\left(\frac{\pi}{n+1}\right)\right], \qquad (5.23c) \\
& 1 - 2|\alpha| \cos\left[\frac{[2-H(\beta)]\pi}{d}\right] - \frac{2|\beta|(n-d+1)}{n+1}\Bigg\}. \qquad (5.23d)
\end{aligned}$$

ω_{opt} is then given by (5.4), simulations show good agreement between the approximation and numerics.

5.4.2. Convergence rate analysis

We begin with the relations $\lambda_{max} = 1 - \nu_{min}$ and $\lambda_{min} = 1 - \nu_{max}$,

$$\omega_{opt} = \frac{2}{\lambda_{max} + \lambda_{min}} = \frac{2}{2 - (\nu_{max} + \nu_{min})}, \qquad \rho = \frac{\lambda_{max} - \lambda_{min}}{\lambda_{max} + \lambda_{min}} = \frac{\nu_{max} - \nu_{min}}{2 - (\nu_{max} + \nu_{min})}.$$

In the case where $d = 2k + 1$ we immediately have

$$\rho_{2k+1} = \nu_{\max} = 1 - \lambda_{\min}.$$

Lets consider two cases: $\beta > 0$ and $\beta < 0$ with limiting cases for d (i.e. $d = O(1)$ and $d \to n$). If $\beta > 0$, then using (5.23), we see that for $d = O(1)$ we have

$$\rho_{2k+1} = \begin{cases} 2(|\alpha| + \beta) & \text{if } d = O(1) \\ 2|\alpha| & \text{if } d = O(n), \end{cases} \tag{5.24a}$$

$$\rho_{2k} = \begin{cases} \frac{|\alpha|\left[1+\cos\left(\frac{\pi}{d}\right)\right]+2\beta}{1+|\alpha|\left[1-\cos\left(\frac{\pi}{d}\right)\right]} & \text{if } d = O(1) \\ 2|\alpha| & \text{if } d = O(n). \end{cases} \tag{5.24b}$$

We conclude that $\rho_{2k} \leq \rho_{2k+1}$ with $\rho_{2k} \uparrow \rho_{2k+1}$ as $d \to n$. Suppose now that $\beta < 0$, then

$$\rho_{2k+1} = \begin{cases} 2|\alpha| \cos\left(\frac{\pi}{d}\right) + 2|\beta| & \text{if } d = O(1) \\ 2|\alpha| & \text{if } d = O(n), \end{cases} \tag{5.25a}$$

$$\rho_{2k} = \begin{cases} \frac{|\alpha|\left[1+\cos\left(\frac{\pi}{d}\right)\right]+2|\beta|}{1-|\alpha|\left[1-\cos\left(\frac{\pi}{d}\right)\right]} & \text{if } d = O(1) \\ 2|\alpha| & \text{if } d = O(n). \end{cases} \tag{5.25b}$$

It can be shown that $\rho_{2k} \geq \rho_{2k+1}$ with $\rho_{2k+1} \uparrow \rho_{2k}$ as $d \to n$ (see appendix).

These relations have interesting practical consequences, particularly in physical problems where domains are discretized. Changing the distance between grid points shifts the nonzero element to a different diagonal. We can then improve the rate of convergence by choosing our grid size in a clever way.

5.4.3. Impact of RHS on ω_{opt}

The numerical sections illustrate an obvious shortcoming of this result. Though we have proven that $\omega_{opt} = 1$ is the best worst-case choice, numerical simulations indicate that this worst-case scenario is difficult to realize in a practical setting. In this section we illustrate the cause.

Let $\mathbf{x}^*$ be the solution to $\mathbf{Ax} = \mathbf{b}$. Then inserting this into (5.2) we obtain

$$\mathbf{e}^{(m+1)} = (\mathbf{I} - \mathbf{M}^{-1}\mathbf{A})\mathbf{e}^{(m)}. \tag{5.26}$$

Define the residual $\mathbf{r}^{(m)} \equiv \mathbf{b} - \mathbf{Ax}^{(m)}$, then manipulation (5.2) gives

$$\mathbf{e}^{(m+1)} - \mathbf{e}^{(m)} = \omega\mathbf{M}^{-1}\mathbf{r}^{(m)}.$$

Replacing $\mathbf{e}^{(m+1)}$ using (5.26), we arrive at

$$\mathbf{r}^{(m)} = \mathbf{Ae}^{(m)}. \tag{5.27}$$

A standard practice with Jacobi is to exit when the norm of the residual $\|\mathbf{r}^{(n)}\| < \epsilon$ where ϵ is some arbitrary cutoff criterion. The representation (5.27) is useful when we represent the error $\mathbf{e}^{(m)}$ using the eigenvectors of $\mathbf{M}^{-1}\mathbf{A}$. Letting $(\lambda_i, \mathbf{y}_i)$ be a eigenvalue/vector pair, we

write

$$\mathbf{e}^{(m)} = \sum_{i=1}^{n} c_i^{(m)} \mathbf{y}_i. \tag{5.28}$$

Taking a norm of (5.27), we obtain the following

$$\|\mathbf{r}^{(m)}\| \leq \|\mathbf{M}\| \|\mathbf{e}^{(0)}\| \sum_{i=1}^{n} |c_i^{(0)} \lambda_i (1-\lambda_i)^m|.$$

Let j be the index which satisfies $|c_j^{(0)} \lambda_j (1-\lambda_j)^m| > |c_i^{(0)} \lambda_i (1-\lambda_i)^m|$. Then we can remove the summation and obtain

$$\|\mathbf{r}^{(n)}\| \leq n \|\mathbf{M}\| \|\mathbf{e}^{(0)}\| |c_j^{(0)} \lambda_j (1-\lambda_j)^m|. \tag{5.29}$$

It is illuminating to see the relation between the term $c_j^{(0)} \lambda_j$ and $\mathbf{b}$. Suppose our initial guess is $\mathbf{x}^{(0)} \equiv 0$ then $\mathbf{e}^{(0)} = -\mathbf{x}^*$. Furthermore, $\mathbf{M}^{-1}\mathbf{A}\mathbf{x}^* = \mathbf{M}^{-1}\mathbf{b} = \tilde{\mathbf{b}}$. Using the expansion (5.28), we see that the coefficients must satisfy $\lambda_i c_i^{(0)} + \tilde{b}_i = 0$. Thus, we see that the right-hand side directly influences the nature of the exit criterion.

From this analysis, it is obvious that $\omega_{\text{opt}} = 1$ will perform better only in particular cases where $\mathbf{b}$ has nonzero coefficient in the eigenvector expansion with eigenvalue λ_i being the largest in magnitude for the function $|1 - \lambda|$.

5.5. Numerical Simulations and Applications

5.5.1. Toeplitz Matrices

In this section, we consider some numerical simulations comparing the asymptotic approximation of ω_{opt} to the numerically obtained optimal ω from computing the eigenvalues for the matrix. We analyze the matrix $\mathbf{B}$, defined in section 5.4.1 for different values of α, β, d, n.

We can see from figure 5.1 that the approximation is in good agreement with the numerics. We also note the convergence of $\omega_{\text{opt}} \to 1$ in all cases as was expected from theorem 5.3.2 or inferred from letting $n, d \to \infty$ in (5.23).

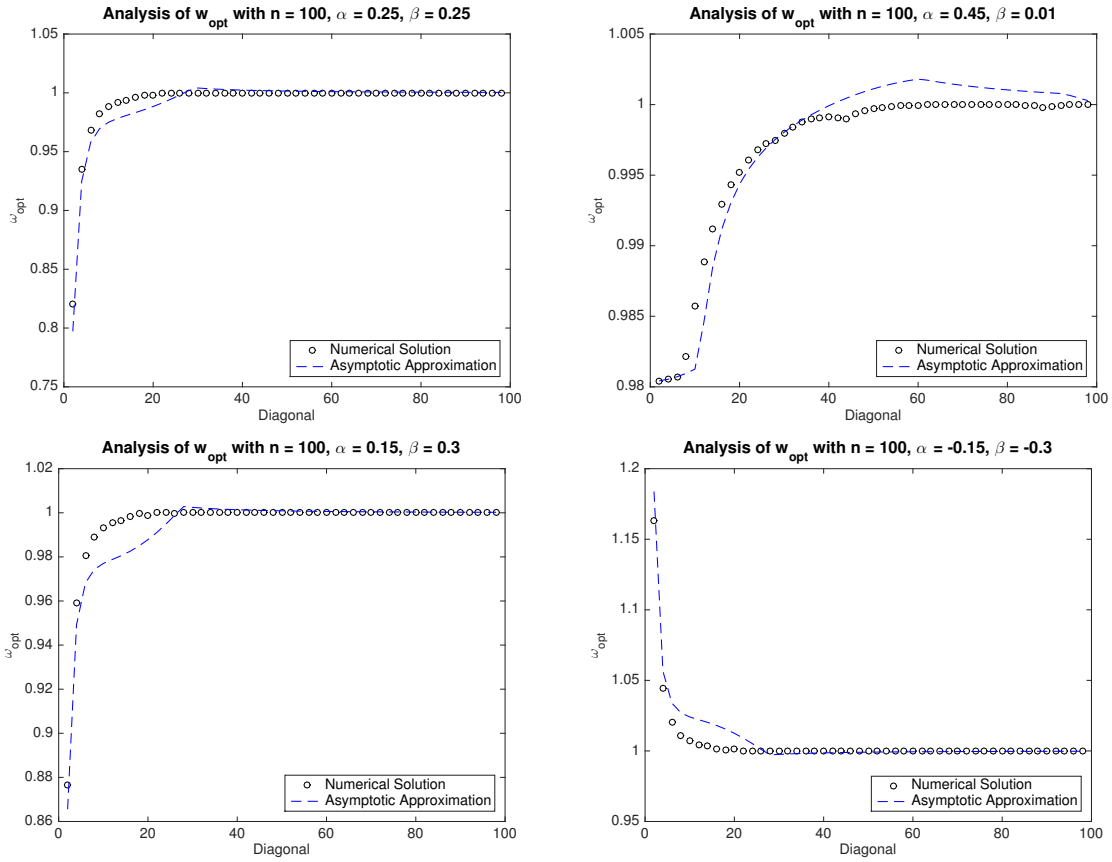

Figure 5.1. Numerical approximation of the eigenvalues are compared to the asymptotic approximation from section 5.4. We see good agreement for a range of values for α and β.

5.5.2. Practical Application: Reduction in computation time

The analysis in section 5.4.2 showed that the convergence rates are sensitive to the sign of the d-diagonal element (β) and d. In this section, we numerically investigate the consequence of

this by changing the diagonal and averaging over 50 different RHS. The details are in figure 5.2.

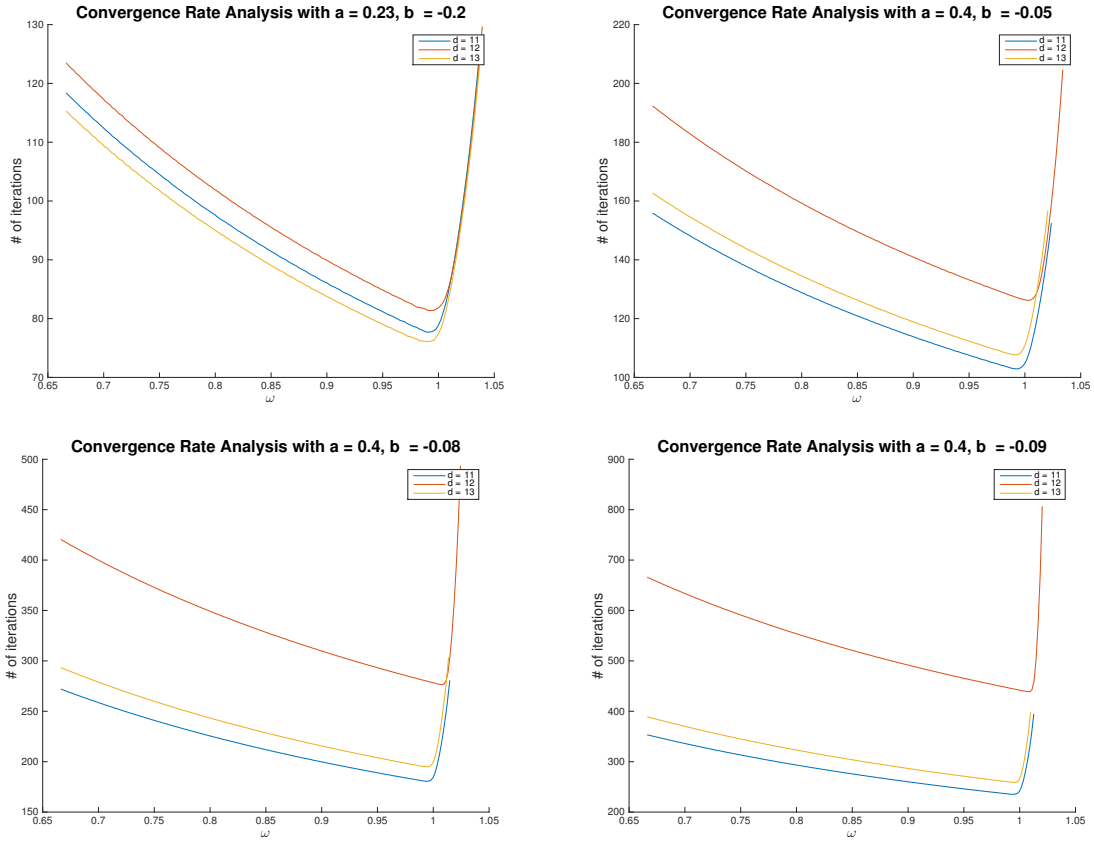

Figure 5.2. The above curves are found by averaging over 50 different right-hand sides in the linear equation $Ax = b$.

5.6. Conclusion

We have extended the theory regarding convergence properties of Jacobi. We demonstrated that the optimal Jacobi parameter is $\omega = 1$ for matrices having nonzero elements only on the main diagonal and odd diagonals. Additionally, we have shown that as $n, d \to \infty$ for matrices of size n and nonzero diagonal d, the Jacobi parameter asymptotically approaches $\omega = 1$.

Practical applications of these results include solving large sparse matrices such as those arising from physical systems. By changing the grid size, large reductions in the number of iterations required can be achieved.

CHAPTER 6

Conclusion

We have used the TDGL equations to gain insight into the mechanisms of dissipation in Type-II superconductors. In chapter 2, we analytically demonstrated the advent of phase slips in weak-linked 1D superconductors by extracting a coupled system of ODEs from the TDGL. This allowed us to understand the dynamics of weak-link phase slips which were previously only studied experimentally and numerically. We moved on to 2D superconductors in chapter 3 where we investigated the effects of an external magnetic field and current in parallel. A critical curve separating the superconductor from vortex (resistive) state was calculated from analytical methods and compared to simulations.

For general 2D and 3D superconductors we looked to optimize the pinning geometry so as to maximize the critical current. We numerically simulated the TDGL and discovered the optimal pinning radius and density for spherical and columnar inclusions. We also determined that for non-rotating fields (say fixed in the z direction), columnar effects were the most effective pinning centers.

In the final chapter we investigated the numerical solver of the TDGL itself. What originally began as a numerical investigation of determining the optimal weighting parameter for Jacobi became a theoretical investigation which uncovered general conditions under which the parameter can be found exactly. We also determined the limiting behavior of this parameter for large matrices and obtained asymptotic estimates when we were close to satisfying these conditions. Theoretical investigations of weighted Jacobi has been sparse

since it appeared over 150 years ago. With the prevalence of parallel computing and its reduction in computation time, ease of parallel methods (e.g. Weighted Jacobi) have gained new ground, making finding the optimal parameter particularly useful. Future work involves generalizing the results to non-hermitian (complex eigenvalue) matrices.

References

[1] D. Van Delft and P. Kes, "The discovery of superconductivity," *Physics Today*, vol. 63, no. 9, pp. 38–43, 2010.

[2] W. Meissner and R. Ochsenfeld, "Ein neuer effekt bei eintritt der supraleitfähigkeit," *Naturwissenschaften*, vol. 21, no. 44, pp. 787–788, 1933.

[3] F. London and H. London, "The electromagnetic equations of the supraconductor," in *Proceedings of the Royal Society of London A: Mathematical, Physical and Engineering Sciences*, vol. 149, pp. 71–88, The Royal Society, 1935.

[4] V. V. Schmidt, *The physics of superconductors: Introduction to fundamentals and applications*. Springer, 2013.

[5] L. D. Landau and V. Ginzburg, "On the theory of superconductivity," *Zh. Eksp. Teor. Fiz.*, vol. 20, p. 1064, 1950.

[6] A. A. Abrikosov, "An influence of the size on the critical field for type-II superconductors," in *Dokl. Akad. Nauk SSSR*, vol. 86, pp. 489–492, 1952.

[7] A. A. Abrikosov, "Magnetic properties of superconductors of the second group," *Sov. Phys.-JETP (Engl. Transl.);(United States)*, vol. 5, no. 6, 1957.

[8] A. Abrikosov, "Nobel lecture: Type-II superconductors and the vortex lattice," *Reviews of modern physics*, vol. 76, no. 3, p. 975, 2004.

[9] W. Kleiner, L. Roth, and S. Autler, "Bulk solution of ginzburg-landau equations for type ii superconductors: upper critical field region," *Physical Review*, vol. 133, no. 5A, p. A1226, 1964.

[10] D. Cribier, B. Jacrot, L. Madhov Rao, and B. Farnoux, "Evidence from neutron diffraction for a periodic structure of the magnetic field in a niobium superconductor," *Phys. Lett*, vol. 9, pp. 106–7, 1964.

[11] H. Traeuble and U. Essmann, "Observed magnetic structure of type-II superconductors," tech. rep., Max-Planck-Institut fuer Metallforschung, Stuttgart. Technische Hochschule, Stuttgart, 1967.

[12] N. Bogoliubov, "New method in the theory of superconductivity. III," *Sov. Phys.-JETP (Engl. Transl.);(United States)*, vol. 7, no. 1, 1958.

[13] L. GoR'Kov, "Energy spectrum of superconductors.[quantum field theory]," *Sov. Phys.-JETP (Engl. Transl.);(United States)*, vol. 7, no. 3, 1958.

[14] L. P. Gorkov, "Microscopic derivation of the ginzburg-landau equations in the theory of superconductivity," *Sov. Phys. JETP*, vol. 9, no. 6, pp. 1364–1367, 1959.

[15] W.-K. Kwok, U. Welp, A. Glatz, A. E. Koshelev, K. J. Kihlstrom, and G. W. Crabtree, "Vortices in high-performance high-temperature superconductors," *Reports on Progress in Physics*, vol. 79, no. 11, p. 116501, 2016.

[16] M. Rupich, "Second-generation (2g) coated high-temperature superconducting cables and wires for power grid applications," *Superconductors in the Power Grid: Materials and Applications*, p. 97, 2015.

[17] B. Josephson, "Possible new effects in superconductive tunnelling," *Physics Letters*, vol. 1, no. 7, pp. 251 – 253, 1962.

[18] P. W. Anderson and J. M. Rowell, "Probable observation of the josephson superconducting tunneling effect," *Physical Review Letters*, vol. 10, no. 6, p. 230, 1963.

[19] T. Clark, "Experiments on coupled josephson junctions," *Physics Letters A*, vol. 27, no. 9, pp. 585–586, 1968.

[20] A. Goldman and P. Kreisman, "Meissner effect and vortex penetration in josephson junctions," *Physical Review*, vol. 164, no. 2, p. 544, 1967.

[21] L. B. Ioffe, V. B. Geshkenbein, M. V. Feigel'Man, A. L. Fauchere, and G. Blatter, "Environmentally decoupled sds-wave josephson junctions for quantum computing," *Nature*, vol. 398, no. 6729, pp. 679–681, 1999.

[22] M. Eschrig and T. Löfwander, "Triplet supercurrents in clean and disordered half-metallic ferromagnets," *Nature Physics*, vol. 4, no. 2, pp. 138–143, 2008.

[23] P. W. Anderson and A. H. Dayem, "Radio-frequency effects in superconducting thin film bridges," *Phys. Rev. Lett.*, vol. 13, pp. 195–197, Aug 1964.

[24] J. Majer, J. Chow, J. Gambetta, J. Koch, B. Johnson, J. Schreier, L. Frunzio, D. Schuster, A. Houck, A. Wallraff, *et al.*, "Coupling superconducting qubits via a cavity bus," *Nature*, vol. 449, no. 7161, pp. 443–447, 2007.

[25] A. Berkley, H. Xu, R. Ramos, M. Gubrud, F. Strauch, P. Johnson, J. Anderson, A. Dragt, C. Lobb, and F. Wellstood, "Entangled macroscopic quantum states in two superconducting qubits," *Science*, vol. 300, no. 5625, pp. 1548–1550, 2003.

[26] D. Wollman, D. Van Harlingen, W. Lee, D. Ginsberg, and A. Leggett, "Experimental determination of the superconducting pairing state in ybco from the phase coherence of ybco-pb dc squids," *Physical Review Letters*, vol. 71, no. 13, p. 2134, 1993.

[27] M. Tinkham, *Introduction to superconductivity*. Courier Corporation, 1996.

[28] G. Blatter, M. V. Feigel'man, V. B. Geshkenbein, A. I. Larkin, and V. M. Vinokur, "Vortices in high-temperature superconductors," *Reviews of Modern Physics*, vol. 66, no. 4, p. 1125, 1994.

[29] J. Mooij and Y. V. Nazarov, "Superconducting nanowires as quantum phase-slip junctions," *Nature Physics*, vol. 2, no. 3, pp. 169–172, 2006.

[30] C. N. Lau, N. Markovic, M. Bockrath, A. Bezryadin, and M. Tinkham, "Quantum phase slips in superconducting nanowires," *Physical review letters*, vol. 87, no. 21, p. 217003, 2001.

[31] A. Glatz and T. Nattermann, "One-dimensional disordered density waves and superfluids: The role of quantum phase slips and thermal fluctuations," *Phys. Rev. Lett.*, vol. 88, p. 256401, Jun 2002.

[32] P. W. Anderson, "Considerations on the flow of superfluid helium," *Reviews of Modern Physics*, vol. 38, no. 2, p. 298, 1966.

[33] J. Langer and M. E. Fisher, "Intrinsic critical velocity of a superfluid," *Physical Review Letters*, vol. 19, no. 10, p. 560, 1967.

[34] K. Schwarz, "Phase slip and turbulence in superfluid he 4: A vortex mill that works," *Physical review letters*, vol. 64, no. 10, p. 1130, 1990.

[35] D. McKay, M. White, M. Pasienski, and B. DeMarco, "Phase-slip-induced dissipation in an atomic bose–hubbard system," *Nature*, vol. 453, no. 7191, pp. 76–79, 2008.

[36] P. Scherpelz, K. Padavić, A. Rançon, A. Glatz, I. S. Aranson, and K. Levin, "Phase imprinting in equilibrating fermi gases: The transience of vortex rings and other defects," *Phys. Rev. Lett.*, vol. 113, p. 125301, Sep 2014.

[37] P. Scherpelz, K. Padavić, A. Murray, A. Glatz, I. S. Aranson, and K. Levin, "Generic equilibration dynamics of planar defects in trapped atomic superfluids," *Phys. Rev. A*, vol. 91, p. 033621, Mar 2015.

[38] K. Wright, R. Blakestad, C. Lobb, W. Phillips, and G. Campbell, "Driving phase slips in a superfluid atom circuit with a rotating weak link," *Physical review letters*, vol. 110, no. 2, p. 025302, 2013.

[39] W. J. Skocpol, M. R. Beasley, and M. Tinkham, "Phase-slip centers and nonequilibrium processes in superconducting tin microbridges," *Journal of Low Temperature Physics*, vol. 16, no. 1, pp. 145–167, 1974.

[40] J. D. Meyer, "Voltage steps in the u(t)-transition curves and in the u(i)-characteristic curves of current-carrying whiskers of tin," *Applied physics*, vol. 2, no. 6, pp. 303–320, 1973.

[41] L. Kramer and A. Baratoff, "Lossless and dissipative current-carrying states in quasi-one-dimensional superconductors," *Phys. Rev. Lett.*, vol. 38, pp. 518–521, Feb 1977.

[42] W. A. Little, "Decay of persistent currents in small superconductors," *Phys. Rev.*, vol. 156, pp. 396–403, Apr 1967.

[43] L. Kramer and R. Rangel, "Structure and properties of the dissipative phase-slip state in narrow superconducting filaments with and without inhomogeneities," *Journal of low temperature physics*, vol. 57, no. 3-4, pp. 391–414, 1984.

[44] R. Rangel and L. Kramer, "Theory of periodically driven, current-carrying superconducting filaments. ii. stability limits of the homogeneous state. periodic and chaotic phase-slip states," *Journal of low temperature physics*, vol. 74, no. 3-4, pp. 163–183, 1989.

[45] A. Weber and L. Kramer, "Dissipative states in a current-carrying superconducting film," *Journal of low temperature physics*, vol. 84, no. 5-6, pp. 289–299, 1991.

[46] I. Aranson and V. Vinokur, "Surface instabilities and vortex transport in current-carrying superconductors," *Physical Review B*, vol. 57, no. 5, p. 3073, 1998.

[47] Y. N. Ovchinnikov and A. Varlamov, "Phase slips in a current-biased narrow superconducting strip," *Phys. Rev. B*, vol. 91, no. 1, p. 014514, 2015.

[48] J. S. Langer and V. Ambegaokar, "Intrinsic resistive transition in narrow superconducting channels," *Phys. Rev.*, vol. 164, pp. 498–510, Dec 1967.

[49] B. Ivlev and N. Kopnin, "Electric currents and resistive states in thin superconductors," *Advances in Physics*, vol. 33, no. 1, pp. 47–114, 1984.

[50] R. Van Dover, A. De Lozanne, and M. Beasley, "Superconductor-normal-superconductor microbridges: Fabrication, electrical behavior, and modeling," *J. Appl. Phys.*, vol. 52, no. 12, pp. 7327–7343, 1981.

[51] V. V. Baranov, A. G. Balanov, and V. V. Kabanov, "Current-voltage characteristic of narrow superconducting wires: Bifurcation phenomena," *Phys. Rev. B*, vol. 84, p. 094527, Sep 2011.

[52] V. V. Baranov, A. G. Balanov, and V. V. Kabanov, "Dynamics of resistive state in thin superconducting channels," *Phys. Rev. B*, vol. 87, p. 174516, May 2013.

[53] S. Michotte, S. Mátéfi-Tempfli, L. Piraux, D. Y. Vodolazov, and F. M. Peeters, "Condition for the occurrence of phase slip centers in superconducting nanowires under applied current or voltage," *Phys. Rev. B*, vol. 69, p. 094512, Mar 2004.

[54] L. Kramer and R. J. Watts-Tobin, "Theory of dissipative current-carrying states in superconducting filaments," *Phys. Rev. Lett.*, vol. 40, pp. 1041–1044, Apr 1978.

[55] G. Berdiyorov, A. d. C. Romaguera, M. Milošević, M. Doria, L. Covaci, and F. Peeters, "Dynamic and static phases of vortices under an applied drive in a superconducting stripe with an array of weak links," *Eur. Phys. J. B*, vol. 85, no. 4, pp. 1–8, 2012.

[56] I. S. Aranson and L. Kramer, "The world of the complex ginzburg-landau equation," *Reviews of Modern Physics*, vol. 74, no. 1, p. 99, 2002.

[57] J. Bardeen, L. N. Cooper, and J. R. Schrieffer, "Theory of superconductivity," *Physical Review*, vol. 108, no. 5, p. 1175, 1957.

[58] I. Sadovskyy, A. Koshelev, C. Phillips, D. Karpeyev, and A. Glatz, "Stable large-scale solver for ginzburg–landau equations for superconductors," *Journal of Computational Physics*, vol. 294, pp. 639–654, 2015.

[59] L. S. Tsimring and I. S. Aranson, "Localized and cellular patterns in a vibrated granular layer," *Physical review letters*, vol. 79, no. 2, p. 213, 1997.

[60] S. H. Strogatz, *Nonlinear dynamics and chaos: with applications to physics, biology, chemistry, and engineering*. Westview press, 2014.

[61] I. Aranson, M. Gitterman, and B. Y. Shapiro, "Onset of vortices in thin superconducting strips and wires," *Physical Review B*, vol. 51, no. 5, p. 3092, 1995.

[62] I. S. Aranson, L. Kramer, and A. Weber, "Dynamics of vortices in current-carrying superconducting films," *Journal of low temperature physics*, vol. 89, no. 5-6, pp. 859–868, 1992.

[63] T. G. Holesinger, L. Civale, B. Maiorov, D. M. Feldmann, J. Y. Coulter, D. J. Miller, V. A. Maroni, Z. Chen, D. C. Larbalestier, R. Feenstra, *et al.*, "Progress in nanoengineered microstructures for tunable high-current, high-temperature superconducting wires," *Adv. Mat.*, vol. 20, no. 3, pp. 391–407, 2008.

[64] A. Malozemoff, "Second-generation high-temperature superconductor wires for the electric power grid," *Annu. Rev. Mater. Res.*, vol. 42, no. 1, pp. 373–397, 2012.

[65] A. A. Abrikosov, "The magnetic properties of superconducting alloys," *J. Phys. Chem. Solids*, vol. 2, no. 3, pp. 199–208, 1957.

[66] G. Blatter, M. V. Feigel'man, V. B. Geshkenbein, A. I. Larkin, and V. M. Vinokur, "Vortices in high-temperature superconductors," *Rev. Mod. Phys.*, vol. 66, p. 1125, Oct 1994.

[67] G. Blatter and V. Geshkenbein, "Vortex matter," in *The physics of superconductors* (K. Bennemann and J. Ketterson, eds.), pp. 725–936, Springer Berlin Heidelberg, 2003.

[68] I. A. Sadovskyy, Y. Jia, M. Leroux, J. Kwon, H. Hu, L. Fang, C. Chaparro, S. Zhu, U. Welp, J.-M. Zuo, Y. Zhang, R. Nakasaki, V. Selvamanickam, G. W. Crabtree, A. E. Koshelev, A. Glatz, and W.-K. Kwok, "Toward superconducting critical current by design," *Adv. Mat.*, vol. 28, no. 23, pp. 4593–4600, 2016.

[69] I. A. Sadovskyy, A. E. Koshelev, C. L. Phillips, D. A. Karpeyev, and A. Glatz, "Stable large-scale solver for Ginzburg-Landau equations for superconductors," *J. Comp. Phys.*, vol. 294, pp. 639–654, 2015.

[70] D. Y. Vodolazov, "Vortex-induced negative magnetoresistance and peak effect in narrow superconducting films," *Phys. Rev. B*, vol. 88, p. 014525, Jul 2013.

[71] G. R. Berdiyorov, M. V. Milošević, and F. M. Peeters, "Novel commensurability effects in superconducting films with antidot arrays," *Phys. Rev. Lett.*, vol. 96, p. 207001, May 2006.

[72] G. R. Berdiyorov, M. V. Milošević, and F. M. Peeters, "Superconducting films with antidot arrays — novel behavior of the critical current," *Europhys. Lett.*, vol. 74, no. 3, p. 493, 2006.

[73] I. A. Sadovskyy, A. E. Koshelev, A. Glatz, V. Ortalan, M. W. Rupich, and M. Leroux, "Simulation of the vortex dynamics in a real pinning landscape of $YBa_2Cu_3O_{7-\delta}$ coated conductors," *Phys. Rev. Applied*, vol. 5, p. 014011, Jan 2016.

[74] I. A. Sadovskyy, Y. L. Wang, Z.-L. Xiao, W.-K. Kwok, and A. Glatz, "Critical current of hexagonally patterned superconducting films." in preparation., 2016.

[75] R. Hooke and T. A. Jeeves, ""Direct search" solution of numerical and statistical problems," *J. ACM*, vol. 8, no. 2, pp. 212–229, 1961.

[76] V. Torczon, "On the convergence of pattern search algorithms," *SIAM J. Optim.*, vol. 7, no. 1, pp. 1–25, 1997.

[77] E. D. Dolan, R. M. Lewis, and V. Torczon, "On the local convergence of pattern search," *SIAM J. Optim.*, vol. 14, no. 2, pp. 567–583, 2003.

[78] C. Audet and J. E. Dennis Jr, "Analysis of generalized pattern searches," *SIAM J. Optim.*, vol. 13, no. 3, pp. 889–903, 2002.

[79] J. C. Lagarias, J. A. Reeds, M. H. Wright, and P. E. Wright, "Convergence properties of the nelder–mead simplex method in low dimensions," *SIAM J. Optim.*, vol. 9, no. 1, pp. 112–147, 1998.

[80] K. I. McKinnon, "Convergence of the nelder–mead simplex method to a nonstationary point," *SIAM J. Optim.*, vol. 9, no. 1, pp. 148–158, 1998.

[81] L. M. Rios and N. V. Sahinidis, "Derivative-free optimization: a review of algorithms and comparison of software implementations," *J. Global Optim.*, vol. 56, no. 3, pp. 1247–1293, 2013.

[82] I. Loshchilov, M. Schoenauer, and M. Sebag, "Adaptive coordinate descent," in *Proc. of the 13th Annual Conference on Genetic and Evolutionary Computation*, pp. 885–892, ACM, 2011.

[83] A. H. G. Rinnooy Kan and G. T. Timmer, "Stochastic global optimization methods part I: clustering methods," *Math. Prog.*, vol. 39, no. 1, pp. 27–56, 1987.

[84] A. H. G. Rinnooy Kan and G. T. Timmer, "Stochastic global optimization methods part II: multi level methods," *Math. Prog.*, vol. 39, no. 1, pp. 57–78, 1987.

[85] J. Kennedy, "Particle swarm optimization," in *Encyclopedia of Machine Learning*, pp. 760–766, Springer, 2011.

[86] R. Poli, J. Kennedy, and T. Blackwell, "Particle swarm optimization," *Swarm Intell.*, vol. 1, no. 1, pp. 33–57, 2007.

[87] I. C. Trelea, "The particle swarm optimization algorithm: convergence analysis and parameter selection," *Inform. Process. Lett.*, vol. 85, no. 6, pp. 317–325, 2003.

[88] M. J. D. Powell, "On search directions for minimization algorithms," *Math. Prog.*, vol. 4, no. 1, pp. 193–201, 1973.

[89] C. Price, I. Coope, and D. Byatt, "A convergent variant of the Nelder-Mead algorithm," *J. Optim. Theory Appl.*, vol. 113, no. 1, pp. 5–19, 2002.

[90] L. Nazareth and P. Tseng, "Gilding the Lily: a variant of the Nelder-Mead algorithm based on golden-section search," *Comp. Optim. Appl.*, vol. 22, no. 1, pp. 133–144, 2002.

[91] A. R. Conn, K. Scheinberg, and L. N. Vicente, *Simplicial Direct-Search Methods*, ch. 8, pp. 141–162. SIAM, 2009.

[92] A. E. Koshelev, I. A. Sadovskyy, C. L. Phillips, and A. Glatz, "Optimization of vortex pinning by nanoparticles using simulations of the time-dependent Ginzburg-Landau model," *Phys. Rev. B*, vol. 93, p. 060508, Feb 2016.

[93] C. G. J. Jacobi, "Über ein leichtes verfahren die in der theorie der säcularstörungen vorkommenden gleichungen numerisch aufzulösen.," *Journal für die reine und angewandte Mathematik*, vol. 30, pp. 51–94, 1846.

[94] L. F. Richardson, "On the approximate arithmetical solution by finite differences of physical problems involving differential equations, with an application to the stresses in a masonry dam," in *Proceedings of the Royal Society of London A: Mathematical, Physical and Engineering Sciences*, vol. 83, pp. 335–336, The Royal Society, 1910.

[95] D. M. Young, *Iterative solution of large linear systems*. Elsevier, 2014.

[96] Y. Saad, *Iterative methods for sparse linear systems*. Siam, 2003.

[97] X. I. Yang and R. Mittal, "Acceleration of the jacobi iterative method by factors exceeding 100 using scheduled relaxation," *Journal of Computational Physics*, vol. 274, pp. 695–708, 2014.

[98] Z. Zhang, Q. Miao, and Y. Wang, "Cuda-based jacobi's iterative method," in *Computer Science-Technology and Applications, 2009. IFCSTA'09. International Forum on*, vol. 1, pp. 259–262, IEEE, 2009.

[99] A. Imakura, T. Sakurai, K. Sumiyoshi, and H. Matsufuru, "An auto-tuning technique of the weighted jacobi-type iteration used for preconditioners of krylov subspace methods," in *Embedded Multicore Socs (MCSoC), 2012 IEEE 6th International Symposium on*, pp. 183–190, IEEE, 2012.

[100] S. D. Conte and C. W. D. Boor, *Elementary numerical analysis: an algorithmic approach*. McGraw-Hill Higher Education, 1980.

[101] D. Young, "Iterative methods for solving partial difference equations of elliptic type," *Transactions of the American Mathematical Society*, vol. 76, no. 1, pp. 92–111, 1954.

APPENDIX A

Properties of Superconductors

A.1. Derivation of the second London equation

The kinetic energy density is given by

$$W_K = \frac{1}{2} m_s v_s^2 = \frac{n_s m v_s^2}{2} = \frac{m j_s^2}{2 n_s e^2} = \frac{1}{2} \Lambda j_s^2.$$

If we use Maxwell's equation (1.1b) for the current density we obtain

$$W_K = \frac{c\Lambda}{32\pi^2} (\nabla \times \boldsymbol{H})^2 = \frac{\lambda^2}{8\pi} (\nabla \times \boldsymbol{H})^2,$$

where we have defined

$$\lambda = \sqrt{\frac{mc^2}{4\pi n_s e^2}}, \tag{A.1}$$

this is the London (magnetic) penetration depth described earlier (the factor 8π was removed to coincide with the magnetic energy density of the superconductor $H^2/8\pi$).

Now we are in a position to obtain the total (Helmholtz) free energy by summing the kinetic and magnetic energy. This leads to

$$\mathcal{F}_{sH}[\boldsymbol{H}] = \mathcal{F}_{s0} + \frac{1}{8\pi} \int [\boldsymbol{H}^2 + \lambda^2 (\nabla \times \boldsymbol{H})^2] \, dV. \tag{A.2}$$

This is a variational problem where we wish to find the $\boldsymbol{H}$, which minimizes the function. Consider the more general variational problem

$$F[\boldsymbol{y}] = \int f(\boldsymbol{y}, \nabla \times \boldsymbol{y})\, dV \tag{A.3}$$

where $y = y_0$ along the surface. Suppose $\boldsymbol{y} = \tilde{\boldsymbol{y}} + \epsilon \boldsymbol{z}$ where $\tilde{\boldsymbol{y}}$ minimizes the functional, $\epsilon \ll 1$. It follows $\boldsymbol{z}|_{\partial V} = 0$ by noting that $\boldsymbol{y}|_{\partial V} = \tilde{\boldsymbol{y}}_{\partial V}$. Also note that defining $G(\epsilon) := F[y_0 + \epsilon\eta]$ we see that $G(0)$ is a minimum and so a necessary condition is $G'(0) = 0$. Plugging this into (A.3) and expanding in small ϵ we have

$$G'(0) = 0 = \int [\boldsymbol{f}_{\boldsymbol{y}} \cdot \boldsymbol{z} + \boldsymbol{f}_{\nabla \times \boldsymbol{y}} \cdot (\nabla \times \boldsymbol{z})]\, dV.$$

Noting the identity $\nabla \cdot (a \times b) = b \cdot (\nabla \times a) - a \cdot (\nabla \times b)$, we obtain

$$\begin{aligned} 0 &= \int [\boldsymbol{f}_{\boldsymbol{y}} \cdot \boldsymbol{z} + \nabla \cdot (f_{\nabla \times \boldsymbol{y}} \times \boldsymbol{z}) + (\nabla \times f_{\nabla \times \boldsymbol{y}}) \cdot \boldsymbol{z}]\, dV \\ &= \int [(\boldsymbol{f}_{\boldsymbol{y}} + \nabla \times f_{\nabla \times \boldsymbol{y}}) \cdot \boldsymbol{z}]\, dV + \int_{\partial V} (f_{\nabla \times \boldsymbol{y}} \times \boldsymbol{z})\, d\boldsymbol{S}. \end{aligned}$$

The surface integral is zero since $\boldsymbol{z} = 0$ along the boundary. The first term is 0 only if the term in parenthesis is identically 0 which leads to an Euler-Lagrange equation:

$$\boldsymbol{f}_{\boldsymbol{y}} + \nabla \times f_{\nabla \times \boldsymbol{y}} = 0. \tag{A.4}$$

A.2. Derivation of Generalized London and quantized magnetic flux

Rewriting (1.1c) in terms of potentials, we have

$$\begin{aligned}
\boldsymbol{F} &= q\left[-\nabla V - \frac{\partial \boldsymbol{A}}{\partial t} + \boldsymbol{v}\times(\nabla\times\boldsymbol{A})\right] \\
&= q\left[-\nabla V + \nabla(\boldsymbol{v}\cdot\boldsymbol{A}) - (\boldsymbol{v}\cdot\nabla)\boldsymbol{A} - \frac{d\boldsymbol{A}}{dt} + (\boldsymbol{v}\cdot\nabla)\boldsymbol{A}\right] \\
&= q\left[-\nabla V + \nabla(\boldsymbol{v}\cdot\boldsymbol{A}) - \frac{d\boldsymbol{A}}{dt}\right] \\
&= q\left[\nabla(\boldsymbol{v}\cdot\boldsymbol{A} - V) - \frac{d\boldsymbol{A}}{dt}\right] \\
&= q\left[\nabla(\boldsymbol{v}\cdot\boldsymbol{A} - V) - \frac{d}{dt}\nabla_{\boldsymbol{v}}(\boldsymbol{v}\cdot\boldsymbol{A} - V)\right].
\end{aligned}$$

Finally, we recall the basic E-L equation

$$\frac{d}{dt}\nabla_{\boldsymbol{v}}\mathcal{L} - \nabla_{\boldsymbol{x}}\mathcal{L} = 0,$$

where $\mathcal{L} = T - U$ where U is the potential and T the kinetic energy. Inserting this into the above gives

$$\boldsymbol{F} = \frac{d}{dt}\nabla_{\boldsymbol{v}}U - \nabla_{\boldsymbol{x}}U,$$

from which we can now read off our generalized potential $U = q(V - \boldsymbol{v}\cdot\boldsymbol{A})$. For consistency, we rescale $\boldsymbol{A} \to \frac{1}{c}\boldsymbol{A}$. The Lagrangian is then

$$\mathcal{L} = \frac{1}{2}mv^2 - qV + \frac{q}{c}(\boldsymbol{v}\cdot\boldsymbol{A}). \tag{A.5}$$

APPENDIX B

Phase slip appendix

B.1. No voltage in the superconducting state

We begin by multiplying (1.20a) by Ψ^* and we differentiate (1.20b) with respect to x. This gives

$$u(i|\Psi|^2\mu + \Psi^*\Psi_t) = \Psi^*\Psi_{xx} + [\nu(x) - |\Psi|^2]|\Psi|^2 \tag{B.1}$$

$$0 = \Im(\Psi^*\Psi_{xx}) - \mu_{xx}. \tag{B.2}$$

Taking the imaginary part of (B.1) and substituting this result into (B.2), we obtain

$$\mu_{xx} - u|\Psi|^2\mu = u\Im(\Psi^*\Psi_t). \tag{B.3}$$

Far from the inclusion, all the applied current is supercurrent and so if $L \gg r$, we expect $j_0 = \Im(\Psi^*\Psi_{xx})|_{x=\pm L}$, which implies that $\mu_x(\pm L) = 0$. Multiplying (B.3) by μ and integrating over the domain gives

$$\int_{-L}^{L} \left(\mu_x^2 + u|\Psi|^2\mu^2\right)\, dx = \mu\mu_x\Big|_{-L}^{L} + u\int_{-L}^{L} \Im(\Psi^*\Psi_t)\, dx.$$

Noting the boundary conditions for μ and the fact that $\Psi_t = 0$ (stationary state), we see that $\mu \equiv 0$.

B.2. Critical current calculation

We separate (2.5) by region (superconducting vs. normal metal) and then take the first integral to obtain the equations

$$E_S = F_x^2 + F^2 + j_0^2 F^{-2} - \frac{1}{2}F^4, \qquad x \notin I \tag{B.4}$$

$$E_I = F_x^2 - CF^2 + j_0^2 F^{-2} - \frac{1}{2}F^4, \qquad x \in I. \tag{B.5}$$

Now, far from the inclusion (near the boundary of the superconductor), $F \to F_\infty$ a constant. Assuming the relevant approximation that $j_0 \ll 1$, we see that $F_\infty^2 \approx 1 - j_0^2$. Inserting this into (B.4), implies that $E_S \approx \frac{1}{2} + j_0^2$. We now use the large C approximation that $C \gg j_0^2 F^{-4}$. Proceeding, we obtain

$$F_I(x) = K_1 e^{(|x|-r)\sqrt{C}},$$

where we have introduced the radius r of the inclusion. Solving the outer region at first order is given by

$$F_S(x) = \tanh\left(\frac{|x| - K_2}{\sqrt{2}}\right).$$

The two constants are determined by the continuity conditions at the boundary of the inclusion. By symmetry, we may analyze just one side of the boundary, then our conditions are

$$K_1 = \tanh\left(\frac{r - K_2}{\sqrt{2}}\right) \tag{B.6}$$

$$K_1 = \frac{1}{\sqrt{2C}}\operatorname{sech}^2\left(\frac{r - K_2}{\sqrt{2}}\right). \tag{B.7}$$

Solving for K_1 and K_2, we obtain

$$K_1 = \frac{1}{\sqrt{2C}} + O\left(\frac{1}{C}\right) \tag{B.8}$$

$$K_2 = r - \frac{1}{\sqrt{C}} + O\left(\frac{1}{C}\right). \tag{B.9}$$

Note the identity $E_S - E_I = (1 + C)F^2(r) \geq 0$. This implies that

$$E_I \approx j_0^2 - \frac{1}{2C} \ll 1.$$

Motivated by this, we assume that E_I is a small parameter. At first order then $E_I = 0$ and looking at $x = 0$ we see that

$$E_I = 0 = -CF^2(0) + j_0^2 F^{-2}(0) - \frac{1}{4}F^4(0),$$

where the derivative has vanished by symmetry. Since F is small in the inclusion, the last term can be neglected and we are left with $j_0 \approx \sqrt{C}F^2(0)$. This leads to eq. (2.6).

B.3. Saddle-node bifurcation analysis

We show that $j_c \propto F^2(0)$ is a necessary condition for a saddle-node bifurcation to occur. Consider (2.5) at $x = 0$ as an algebraic equation and defining $F_0 \equiv F(0)$, we obtain

$$F_0^6 + CF_0^4 - F_{xx}(0)F_0^3 + j_0^2 = 0. \tag{B.10}$$

If $j_0 = j_c$ is a saddle-node bifurcation, then two solutions to this equation merge and so the derivative with respect to j_0 approaches infinity as $j_0 \to j_c$. Differentiating (B.10), we obtain

$$\left[6F_0^5 + 4CF_0^3 - 3F_{xx}(0)F_0^2\right]\frac{dF_0}{dj_0} - F_0^3\frac{dF_{xx}(0)}{dj_0} + 2j_0 = 0.$$

Now we have two derivatives which diverge as $j_0 \to j_c$, we can balance in three ways. Suppose first that $dF_{xx}(0)/dj_0 \gg dF_0/dj_0$, then we require $F_0 = 0$, which leads to $j_c = 0$. Alternatively, we can require $dF_{xx}(0)/dj_0 = O(dF_0/dj_0)$ or $dF_{xx}(0)/dj_0 \ll dF_0/dj_0$. Both lead to the same requirement with the difference being a numerical constant.

Suppose then that $dF_{xx}(0)/dj_0 = \beta dF_0/dj_0$, when $j_c - j_0 \ll j_c$. At first order then, we require

$$F_0^2[6F_0^3 + (4C - \beta)F_0 - 3F_{xx}(0)] = 0.$$

The nontrivial result is then

$$F_{xx}(0) = \frac{1}{3}F_0[(4C - \beta) + 6F_0^2].$$

Plugging this into (B.10), we obtain

$$j_0^2 = \frac{1}{3}F_0^4[(C - \beta) + 3F_0^2].$$

Thus, we see that if a SN bifurcation occurs, the location of the critical current $j_c \propto F_0^2$ for $F_0 \ll 1$, in agreement with the asymptotic calculation in appendix B.2.

B.4. Numerical analysis of j_c

To analyze the error associated with calculating j_c numerically, we took $L = 20$ and varied Δx. The results are shown in figure B.1. Assuming the error is linear, we extrapolate the critical current to be $j_c \approx 0.06366$, which is in excellent agreement with the linear system solved using NAG. For fixed $\Delta x = 0.05$, we measured the sensitivity of L on j_c and found no significant change for $L \gg r$ (typically $L > 5r$ was sufficient).

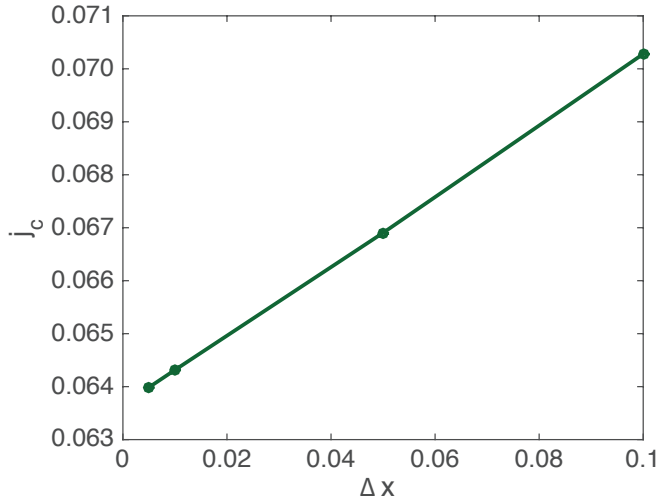

Figure B.1. Convergence of j_c as a function of Δx. As $\Delta x \to 0$, j_c approaches the true value. Dynamic simulations took place with $\Delta x = 0.05$.

B.5. Weakly nonlinear calculation

To obtain the weakly nonlinear system, we analyze near $j_0 = j_c + \epsilon$ where $|\epsilon| \ll 1$. Linearizing about the base state near $\epsilon = 0$ with $\Psi = (R + \eta)e^{i\phi}$. From before, we saw that $\epsilon = 0$ leads to a degenerate zero eigenvalue implying that the linearized system has a generalized eigenvector solution where $L\eta_1 = 0$ and $L\eta_2 = \eta_1$. We use Ansatz $\eta = A\delta\eta_1 + \delta^2 B(\eta_2 + z) + \delta^3\zeta$ where $\eta_k = \begin{pmatrix} U_k \\ V_k \end{pmatrix}$ and $\epsilon = \alpha\delta^2$. Inserting this into (2.2a)–(2.2c) with the aid of mathematica and obtain at first order the ODE for A

$$\mathcal{L}z = u\eta_1\partial_\tau A - \eta_1 B -$$

$$\begin{pmatrix} -A^2\left[R(3U_1^2 + V_1^2) + uV_1\int_{-L/2}^{x}(R'V_1 - RV_1' - 2R\phi'U_1)\,ds\right] \\ -A^2\left[uU_1\int_{-L/2}^{x} RV_1' - R'V_1 + 2R\phi'U_1\,ds + R\left(2U_1V_1 + u\int_{-L/2}^{x}\{\phi'(U_1^2 + V_1^2) + U_1V_1' - U_1'V_1\}\,ds\right)\right] \end{pmatrix}.$$

At next order, we obtain the ODE for B (where we have already projected onto the eigenvector)

$$
\begin{aligned}
u\partial_\tau B\langle U_1^\dagger, U_2\rangle = \Bigg\langle U_1^\dagger, A^3\left\{uV_1\int_{-L/2}^{x}[\phi'(U_1^2+V_1^2)+U_1V_1'-U_1'V_1]\,ds - U_1^3 - U_1V_1^2\right\} - 2KR\phi' + \\
AB\Bigg[uV_2\int_{-L/2}^{x}(2R\phi'U_1+RV_1'-R'V_1)\,ds - \\
uV_1\int_{-L/2}^{x}(2R\phi'U_2+RV_2'-R'V_2)\,ds - 2R(3U_1U_2+V_1V_2)\Bigg]\Bigg\rangle \\
u\partial_\tau B\langle V_1^\dagger, V_2\rangle = \left\langle V_1^\dagger, -A^3\left\{U_1^2V_1+V_1^3+uU_1\int_{-L/2}^{x}[\phi'(U_1^2+V_1^2)+U_1V_1'-U_1'V_1]\,ds\right\} - \right. \\
AB\Bigg\{U_2\left[2RV_1+u\int_{-L/2}^{x}(RV_2'-R'V_2+2R\phi'U_2)\,ds\right] + \\
U_1\left[2RV_2+u\int_{-L/2}^{x}(RV_2'-R'V_2+2R\phi'U_2)\,ds\right] + \\
uR\int_{-L/2}^{x}[U_2V_1'-V_2U_1'+U_1V_2'-V_1U_2'+2\phi'(U_1U_2+V_1V_2)]\,ds\Bigg\} \\
\left. + K\left(2R'-uR\int_{-L/2}^{x}R^2\,ds\right)+u\alpha xR\right\rangle
\end{aligned}
$$

APPENDIX C

Superconductor Analysis

C.1. Global instability

We consider an infinite homogenous superconductor subject to an electric current with no external magnetic field. Without a magnetic field, we can without loss assume the current is in the $+x$ direction and by symmetry all variations occur only along the x direction. Substitution of (1.20a)-(1.20b) with $\Psi = Re^{i\phi}$ yields the requirement,

$$R^2 = 1 - \varphi_x^2.$$

We seek homogenous solutions and so this requires $\phi_x = k$, a constant. It follows that $\phi = kx$, $R = \sqrt{1-k^2}$ and $j_0 = k(1-k^2)$.

To analyze the stability of this solution, we perturb by inserting $\Psi = (R+\eta)e^{ikx}$ into (1.20a) which gives,

$$u\eta_t = \eta'' + 2ik\eta' - (1-k^2)(\eta + \eta^*).$$

Letting $\eta = (A + iB)e^{iqx+\omega t}$, we obtain the coupled problem (redefining $B \to iB$)

$$\begin{pmatrix} u\omega + q^2 + 2(1-k^2) & 2kq \\ 2kq & u\omega + q^2 \end{pmatrix} \begin{pmatrix} A \\ B \end{pmatrix} = \begin{pmatrix} 0 \\ 0 \end{pmatrix}.$$

This has nontrivial solutions only when the determinant is zero. Setting it to zero, we obtain an implicit relation for $\omega(q)$ by

$$(u\omega + q^2 + 2[1-k^2])(u\omega + q^2) - 4k^2q^2 = 0.$$

We are interested in when $\omega(q) > 0$. For $q \gg 1$ we expand in large q and obtain $\omega(q) = -q^2/u < 0$ and so high frequency numbers are damped out the fastest. We observe next that with $q = 0$ we obtain a negative root and $\omega = 0$. Expanding in small q we have at next order that

$$\omega(q) = -\frac{q^2(1-3k^2)}{u(1-k^2)}.$$

For this mode to be stable for all $q \to 0$ we require that $1 - 3k^2 > 0$. This defines our $k_c = 1/\sqrt{3}$ which implies the depairing current $j_c = 2/\sqrt{27} \approx 0.3849$.